Nanoscale Wireless Optical Communication Receivers with Graphene and Carbon Nanotube

by

Burhan Gülbahar

A Thesis Submitted to the
Graduate School of Sciences and Engineering
in Partial Fulfillment of the Requirements for
the Degree of

Doctor of Philosophy
in
Electrical and Electronics Engineering

Koç University

January 2012

Nanoscale Wireless Optical Communication Receivers with Graphene and Carbon Nanotube

Approved by:

Assoc. Prof. Dr. Özgür Barış AKAN, Advisor

Assoc. Prof. Dr. Fatih ALAGÖZ
Department of Computer Engineering, Boğaziçi University

Assist. Prof. Dr. Serdar KOZAT
Department of Electrical and Electronics Engineering, Koç University

Assoc. Prof. Dr. Tuna TUĞCU
Department of Computer Engineering, Boğaziçi University

Assist. Prof. Dr. A. Behzat ŞAHİN
Department of Electrical and Electronics Engineering, Middle East Technical University

Date Approved

To my father OSMAN GÜLBAHAR and mother KAMER GÜLBAHAR

ABSTRACT

Graphene and carbon nanotube are two popular building blocks of nanotechnology with significant electronic, optical, mechanical and thermal properties and diverse growing application areas in physical, chemical, biological and technological sciences. Graphene as a tiny two-dimensional atomic layer carbon sheet and its rolled version into nanometer scale diameter nanotubes have been used in field effect transistor structures with significant electronic and optoelectronic properties. Metal-graphene-metal (MGM) photodetectors with single or multi-layer graphene sheets are promising for future nanoscale optical communication architectures because of wide range absorption from far infrared to visible spectrum, fast carrier velocity and advanced production techniques due to planar geometry. Similarly, carbon nanotube field-effect transistors (CNTFETs) show significant photodetection performances due to wide spectral region, tunable band-gap and fast carrier velocity. Both of the structures with nanoscale dimensions and efficient optoelectronic properties open the possibility to be used in next generation optical wireless communication (OWC) networking architectures. In this thesis, the communication theoretical modeling and analysis of nanoscale optical wireless receivers based on single layer graphene (SLG) and single walled nanotubes (SWNTs) are established. The performance limitations of photodetectors due to their resistive and capacitive elements, and carrier velocity are analyzed. The fundamental communication theoretical performance metrics, i.e., signal-to-noise ratio (SNR), bit-error rate (BER) and data rate, are theoretically modeled and numerically simulated. It

is shown that tens of Gb/s and hundreds of Mb/s data rates for SLG and SWNT, respectively, can be achieved with practical power levels where intrinsic THz data range communication capability is explored. Thermal and shot noise limited regimes of the photodetectors are explored with respect to varying transmit power levels. Furthermore, diversity combining methods for multi-receiver graphene detectors are introduced which increase the efficiency of the detectors. Moreover, broadcast information network for nanotube networks are introduced in a transmit power optimization framework. The communication theoretical modeling and performance analysis of graphene and carbon nanotube optical receivers lay the foundations for next generation nanoscale wireless optical communication architectures.

ÖZET

Grafen ve karbon nanotüp, önemli elektronik, optik, mekanik ve termal özellikleri ve fiziksel, kimyasal, biyolojik ve teknolojik bilimlerde artan uygulama alanları ile nanoteknolojinin iki popüler yapı taşıdır. İki boyutlu incecik atomik tabaka karbon levha olan grafen ve onun nanometre ölçekli çaplı nanotüpler biçiminde yuvarlanmış hali olarak karbon nanotüp, önemli elektronik ve optoelektronik özellikleri ile etkili transistör yapıları içinde kullanılmıştır. Tekli ya da çoklu-katman grafen levhalara sahip metal-grafen-metal (MGM) fotodetektörler, uzak kızılötesinden görünür spektruma kadar geniş emme aralığı, hızlı taşıyıcı hızı ve düzlemsel geometri nedeniyle gelişmiş üretim teknikleri sayesinde gelecek nano ölçekli optik haberleşme mimarileri için umut vericidir. Benzer şekilde, karbon nanotüp alan etkili transistörler (KNTAET'ler) geniş spektral bölgesi, ayarlanabilir bant aralığı ve hızlı taşıyıcı hızı nedeniyle önemli fotodetektör performansları göstermektedirler. Her ikisinin de nano ölçekli boyutları ve verimli optoelektronik özellikleri, yeni nesil optik kablosuz iletişim (OKİ) ağ mimarilerinde kullanılma olasılığını açar. Bu tez çalışmasında, tek katman grafen (TKG) ve tek duvarlı nanotüpler (TDNT'ler) temelli nano ölçekli optik kablosuz alıcıların iletişim teorik modelleme ve analizi inşa edilmiştir. Fotodetektörlerin, rezistif ve kapasitif elemanlar ve taşıyıcı hızı nedeniyle olan performans sınırlamaları analiz edilir. Temel iletişim teorik performans ölçütleri, yani sinyal-gürültü oranı (SGO), bit-hata oranı (BHO) ve veri hızı, teorik olarak modellenmiş ve sayısal olarak simüle edilmiştir. TKG ve TDNT için, özgün THz veri iletişim yeteneğinin keşfedilmesiyle birlikte, sırasıyla, yüzlerce Gb/s ve onlarca Mb/s veri hızlarının pratik güç seviyeleri ile sağlanabileceği gösterilmiştir. Fotodetektörlerin termal ve ani atışlı gürültü sınırlı rejimleri değişen iletim güç seviyelerine göre incelenmiştir. Ayrıca, çoklu alıcı grafen detektörler için verimliliği artıran çeşitlilik birleştirme yöntemleri tanıtılmıştır. Dahası, nanotüp ağlar için bilgi yayın

ağı, iletim gücü optimizasyonu çerçevesinde tanıtıldı. Grafen ve karbon nanotüp optik alıcıların iletişim teorik modelleme ve performans analizi, yeni nesil nano ölçekli kablosuz optik haberleşme mimarisinin temellerini oluşturmaktadır.

ACKNOWLEDGEMENTS

First of all, I want to thank my advisor Dr. Özgür Barış Akan. He has open my horizon to become a successful researcher in frontiers of electronics engineering. I appreciate all his contributions related to ideas, time, motivational stimulation and funding to make my Ph.D. experience successful. His hard working and creative enthusiasm gave me an invaluable experience. He contributed a lot to my social and academic life as a great friend in addition to being a precious advisor.

I am also thankful for the invaluable contributions and insightful discussions of the thesis supervising and jury committee members Dr. Serdar Kozat and Dr. Fatih Alagöz. I would also like to acknowledge the thesis jury members Dr. Tuna Tuğcu and Dr. A. Behzat Şahin for their interest, time and discussions.

The members of the Next-generation and Wireless Communications Laboratory (NWCL) group have contributed significantly to my personal and academic life in Koç University: Dr. Barış Atakan, Özgür Ergül, Ahmet Ozan Biçen, Murat Kuşcu and Murat Kocaoğlu. The group has given me a lot in terms of friendship, advice, collaboration and joyful moments of academic life. I would like to thank to B. Tan Bacınoğlu, a former member of the group, for his valuable discussions on quantum mechanical perspective of nanoscale communications and friendly support.

I am also grateful to the administrative staff of Koç University for making easier the troubles of academic education. I would like to thank to Koç University for all the resources provided to create successful and creative academicians. I would like to give special thanks to the Department of Electrical and Electronics Engineering of Koç University providing a high-level research and academic atmosphere.

I also gratefully acknowledge the funding resources provided by Scientific and Technological Research Council of Turkey (TUBITAK).

Lastly, I would like to thank my father Osman and mother Kamer for their infinite love to succeed my thesis work in the path to become a human with free spirit. I am especially grateful to my sister Elif for her encouragement and valuable discussions about the academic life.

Burhan Gülbahar

Koç University

January 2012

TABLE OF CONTENTS

LIST OF TABLES

LIST OF FIGURES

LIST OF ABBREVIATIONS

0D zero-dimensional, p. 2.

1D one-dimensional, p. 2.

2D two-dimensional, p. 2.

AM amplitude modulation, p. 18.

ASK amplitude shift keying, p. 18.

AWGN additive white Gaussian noise, p. 15.

BB branch and bound, p. 7.

BER bit-error rate, p. 4.

BLG bi-layer graphene, p. 52.

CMOS complementary metal-oxide-semiconductor, p. 2.

CNT carbon nanotube, p. 3.

CNTFET carbon nanotube field-effect transistor, p. 6.

CVD chemical vapor decomposition, p. 123.

CW continuous wave, p. 121.

DOS density-of-states, p. 49.

EGC equal gain combining, p. 6.

FDM frequency division multiplexing, p. 18.

FET field-effect transistor, p. 26.

FIR far-infrared, p. 2.

FM frequency modulation, p. 18.

FSK frequency shift keying, p. 18.

FWHM full width at half maximum, p. 105.

GMR giant magnetoresistance, p. 2.

GNR graphene nanoribbon, p. 51.

GPD graphene photodetector, p. 2.

IC integrated circuit, p. 1.

IM/DD intensity modulation and direct detection, p. 5.

IR infrared, p. 10.

LD laser diode, p. 14.

LED light-emitting diode, p. 14.

LIPSOL Linear Interior Point Solver, p. 75.

LOS line-of-sight, p. 15.

LP linear programming, p. 7.

MGM metal-graphene-metal, p. 36.

MLG multi-layer graphene, p. 62.

MOS metal-oxide-semiconductor, p. 1.

MOSFET metal-oxide-semiconductor field-effect transistor, p. 97.

MRC maximal ratio combining, p. 6.

MSM metal-semiconductor-metal, p. 25.

MWNT multi-walled carbon nanotube, p. 88.

NEGF non-equilibrium Green's function, p. 109.

NL noise-limited, p. 35.

NoC Network-on-Chip, p. 86.

NRZ non-return-to-zero, p. 5.

NW nanowire, p. 13.

OPA optimum power allocation, p. 87.

OWC optical wireless communications, p. 1.

PAM pulse amplitude modulation, p. 18.

PCM pulse code modulation, p. 18.

PDM pulse duration modulation, p. 18.

PPM pulse position modulation, p. 18.

PSK phase shift keying, p. 12.

PTE photothermoelectric effect, p. 55.

QDIP quantum dot infrared photodetector, p. 13.

QHE quantum Hall effect, p. 42.

QWIP quantum well infrared photodetector, p. 13.

RLT reformulation-linearization technique, p. 75.

RZ return-to-zero, p. 18.

SB Schottky barrier, p. 6.

SDP semidefinite programming, p. 7.

SNR signal-to-noise ratio, p. 4.

SR single receiver, p. 40.

SWNT single walled carbon nanotube, p. 25.

TE thermionic emission, p. 27.

TU tunneling, p. 114.

UPA uniform power allocation, p. 87.

UV ultra-violet, p. 2.

WDM wavelength division multiplexing, p. 12.

WSK wavelength shift keying, p. 18.

CHAPTER 1

INTRODUCTION

1.1 Motivation

The evolution of the society necessitates higher demands from technology in main industries regarding to applications for communications, information and military purposes. The microelectronics industry will evolve towards nanoelectronics due to reduction of electronic devices below 10 nm triggered by growing demands such as smaller size and faster electronic components, higher memory capacity of integrated circuits (ICs), higher transmission data speed, higher bandwidth optical communication receivers etc. [117]. For example, the reduction in the sizes of metal-oxide-semiconductor (MOS) transistors evolves the devices to operate in quantum mechanical nanoscale regime. The operation of these nanoscale devices is described by mesoscopic and quantum physics.

The nanoelectronic materials and their devices discovered along the last several decades construct the foundations of the next generation electronics, optoelectronics and communication industries. Optical wireless communications (OWC) is a complementary method to radio frequency communications technology where both of them are affected significantly by the developing nanotechnology inventions. For example, nanoscale electronics has high impacts in various areas of *solid state nanoelectronics*, *superconducting electronics*, *spintronics*, *molecular electronics*, *bioelectronics* and *optoelectronics* which includes the main subject of the thesis, i.e., graphene and nanotube nanoscale photodetectors [117]. Solid state nanoelectronics includes heterostructures of popular materials like Si, SiO_2 and III-V compounds, and transistors of single-electron, resonant-tunneling and ballistic type. Superconducting electronics leads to high speed, low power consuming and almost zero

resistance Josephson junctions. Spintronics with electron-spin transistors and giant magnetoresistance (GMR) effect exploits the spin orientation of electrons which can be successfully integrated with complementary metal-oxide-semiconductor (CMOS) circuits. GMR effect has been awarded Nobel Prize in Physics in 2007. It has many application areas like modern hard drives and magnetic sensors. Molecular electronics utilizing nanoscale collections of molecules as electronic components based on different states or configurations that molecules can take leads to the ultimate step in miniaturization. Bioelectronics or bio-inspired electronics tries to imitate nature in achieving difficult tasks such as imitating neurons in parallel processing. Furthermore, the intersection of biology with nanoelectronics leading to novel devices such as biosensors and DNA chips has potential applications in medicine, biomedical sciences and various physical and technological industries.

Nanoscale optoelectronics is another emerging field which takes significantly growing attention in the last decades where the electronic devices are potentially argued to be replaced by photonic devices [117]. Optoelectronic devices have developed significantly based on nanoscale materials such as III-V direct gap semiconductors, quantum well and quantum dot, denoted as zero-dimensional (0D), based semiconductor structures, one-dimensional (1D) nanotube and nanowire structures, organic and inorganic molecules and two-dimensional (2D) layers of graphene. Graphene and carbon nanotube have high impacts in nanoscale photodetector technologies which will be explored throughout the thesis.

Recently, graphene with its groundbreaking experiments and groundbreaking properties as a 2D nanoscale atomic layer carbon sheet has taken Nobel Prize in Physics in 2010 to Andre Geim and Konstantin Novoselov. It has very unique electronic and photonic properties which can be utilized in electronics components and especially as graphene photodetectors (GPDs) making graphene promising for future nanoscale optical communication architectures with its ultra wide-band absorption spectrum from far-infrared (FIR) to ultraviolet (UV), fast carrier velocity, tunable absorption with various device geometries such

as patterning into smaller pieces and forming bi-layers and advantages of fabrication due to planar geometry [57, 188]. Graphene photodetectors as tiny single atomic layer sheets show high internal quantum efficiencies reaching 30% and hundreds of Gb/s data rate performances [124, 141, 188] laying the foundations of the graphene in future optoelectronics applications.

On the other hand, carbon nanotube is another rising star of the last decades in the nanotechnology world as a promising candidate for future nanoscale communication networks. After the pioneering works of Suomo Iijima on carbon nanotubes (CNTs) in 1991 and 1993 [71, 73], there is a significantly accelerating number of works, applications and advances on carbon nanotubes with application areas in physical and technological sciences. CNTs with nanometer scale diameters are ultra-light weight strongest materials in terms of tensile strength. They have extremely large thermal conductivity and ballistic conductivity of electrons at room temperature making them quasi-1D structures [12,78]. CNTs are promising to be used in nanoscale optoelectronic and photonic applications as photodetectors and nanoscale light sources due to unique optical properties, tunable bandgap, wide spectral region, significant ballistic transport of carriers, efficiency and nanoscale size diameters. CNT field effect transistors as photodetectors show significant performances with potentials of hundreds of Gb/s data rates [148, 167, 168] making them candidates for future optoelectronic devices.

The significant properties of graphene and carbon nanotube and the availability of their high performance photodetector experiments open the way to analyze their theoretical performances as photodetectors in wireless optical communications architectures. It is of fundamental importance to model and analyze the foundations of nanoscale optical wireless communication architectures based on graphene and carbon nanotube as the rising stars of the last decade. In this thesis, the communication theoretical foundations of the experimentally available graphene and single walled carbon nanotube photodetectors are constructed.

The gap between graphene and carbon nanotube optoelectronics and the wireless communications is tried to be filled by analyzing the basic communication theoretical aspects of graphene and carbon nanotube optical communication networks. Next, the main contributions of the thesis are summarized.

1.2 Contribution

The publications corresponding to the study in this thesis are as the following,

1. B. Gulbahar, O. B. Akan, "A Communication Theoretical Modeling of Single-Walled Carbon Nanotube Optical Nanoreceivers and Broadcast Power Allocation," to appear in IEEE Transactions on Nanotechnology, 2011.

2. B. Gulbahar, O. B. Akan, "A Communication Theoretical Modeling of Single-layer Graphene Photodetectors and Efficient Multi-receiver Diversity Combining," to appear in IEEE Transactions on Nanotechnology, 2011.

where bi-layer graphene in multi-color tunable multi-receiver photodetectors and analysis of stochastic resonance in its performance are ongoing works.

In the current literature, there are experimental works analyzing the metal-graphene-metal photodetectors in terms of photocurrent, dark current and theoretical analysis of cut-off bit rates. Similarly, graphene phototransistors composed of graphene nanoribbon and bi-layers are theoretically analyzed in terms of dark current detectivity. However, the communication theoretical fundamentals of single-layer metal-graphene-metal photodetectors are not analyzed with models of nanoscale optical receivers in terms of fundamental performance metrics, i.e., signal-to-noise ratio (SNR), bit-error rate (BER) and cut-off bit rates (R_b). Furthermore, networking concepts such as diversity combining and multi-receiver graphene structures with size diversity are not considered before.

Besides that, for carbon nanotubes, photocurrent, dark current and efficiency of carbon nanotube photodiodes and photodetectors are analyzed experimentally in great detail, however, their communication theoretical fundamentals are not analyzed in terms of optical receiver modeling and fundamental performance metrics of SNR, BER and R_b. Furthermore, wireless optical networking concepts like broadcast networking of nanotubes with various diameters are not considered before.

The summary of the novel contributions related to single layer graphene wireless optical receivers can be listed as the following.

- Classification of graphene wireless optical receivers with respect to their basic layouts as photo-thermoelectric, symmetric metal and asymmetric metal p-n junctions, multi-layer p-i-n schemes and phototransistors.

- Theoretical modeling and analysis of photocurrent and noise performances of single-layer symmetric metal-graphene-metal photodetectors within an optical communication perspective.

- Theoretical modeling and analysis of single-layer symmetric metal-graphene-metal photodetectors in terms of communication theoretical performance metrics of SNR, BER and cut-off data rate with emphasis on resistive, capacitive and carrier velocity limitations showing tens of Gb/s achievable data rates with very low BERs for intensity modulation and direct detection (IM/DD) non-return-to-zero (NRZ) on-off keying modulation.

- Analysis of shot and thermal noise limited performance regimes with emphasis on graphene layer width dependence and the observation of the dominating thermal noise limited regime for practical power levels.

- Introduction of the concepts of multi-receiver graphene photodetectors and their diversity combining as a method to increase the efficiency of the detector.

- Introduction of the parallel line-scan optical networking transmit topology
- Performance analysis of maximal ratio (MRC) and equal gain (EGC) diversity combining methods
- Computation of the optimum receiver placement within a diversity combining framework which both homogenizes and improves nonuniform SNR of single receiver parallel line-scan spatial channels by solving max-min concave quadratic and linear optimization problems with reformulation-linearization technique and liner programming, respectively.

On the other hand, the summary of novel contributions related to single walled carbon nanotube wireless optical receivers can be listed as the following.

- Classification of single walled carbon nanotube wireless optical receivers as carbon nanotube field-effect transistor (CNTFET) photoconductive devices, CNT p-n junctions with tunable gate voltages and Schottky barrier (SB) CNTFET photodiodes.
- Theoretical modeling and analysis of photocurrent and noise performances of metal-single walled nanotube-metal small diameter, i.e., (0.7-1.2) nm, carbon nanotube receivers within an optical communication perspective.
- Theoretical modeling and analysis of diameter dependent communication theoretical performance metrics of SNR, BER and cut-off data rate with emphasis on resistive, capacitive and carrier velocity limitations showing hundreds of Mb/s data rate with very low BERs for intensity modulation and direct detection non-return-to-zero on-off keying modulation.
- Parameter fitting of the developed theoretical models with experimental data in literature.
- Analysis of shot, thermal and dark noise limited performance regimes.

- Introduction of the concept of multi-user CNT ad hoc network topology for wireless optical information broadcast.

- Optimization framework maximizing the minimum SNR in the broadcast network as NP-hard quadratic and linear power allocation problems among transmitter frequencies, the solution with semidefinite programming (SDP) relaxation method combined with Branch and Bound (BB) framework, i.e., SDP-BB, and linear programming (LP), and the observation of significant improvement in terms of SNR gain and data rate with optimum power allocation.

As a result, the communication theoretical basics of graphene and carbon nanotube photodetectors are constructed and the foundations for future nanoscale optical wireless communication architectures are formed. The basic communication theoretical modeling and analysis, and the introduction of the optical wireless networking concepts for the two important nanoscale building blocks, i.e., graphene and carbon nanotube, bridge the gap between the physical sciences, where the quantum mechanical rules specify the characteristics, and the wireless communication technology of engineering background. By using the developed models in this thesis, novel networking concepts and protocols can be developed for future graphene and carbon nanotube wireless optical communication networks.

1.3 Organization

The organization of the thesis is as the following. In Chapter-2, the background on optical wireless communications (OWC) is given by presenting the history of optical communications, recent advancements in nanoscale optoelectronic devices and applications, the system model of OWC, the conventional modulation formats, the characteristics of dynamical response analysis, photodetector types and communication theoretical analysis for BER and SNR in OWC systems.

In Chapter-3, the graphene nanoscale photodetectors are discussed, modeled and analyzed communication theoretically. Firstly, in Section-3.1, the basic properties of graphene

are introduced. The electronic properties are analyzed in a detailed manner emphasizing the resistance, carrier velocity and capacitance models which are important parameters in a graphene field effect transistor photodetector application. Furthermore, optical properties of graphene are analyzed concentrating on the optical absorption properties of single-layer graphene and band-gap tuning with various methods. Then, two important members of graphene family, i.e., bi-layer graphene and graphene nanoribbons, are introduced with their potential advantages and application areas. Next, in Section-3.2, various graphene photodetector types such as photo-thermoelectric detectors, junction photodetectors including symmetric, asymmetric metals, multi-layer p-i-n photodetectors and phototransistors are introduced. Then, the efficiency of graphene photodetectors and the methods to improve it are discussed. In Section-3.4, the single layer graphene photodetector is modeled in terms of equivalent circuit, photocurrent, noise and SNR. Then, in Section-3.5, diversity combining methods for multi-receiver graphene photodetectors are introduced. Furthermore, in Section-3.6, parallel line-scan optical networking topology is introduced for graphene nanoscale photodetectors. In Section-3.7, the optimum graphene photodetector placement and the selection of widths are presented for a diversity combining optimization framework for spatial parallel line-scan channels. Finally, in 3.8, the numerical analyses of the modeled graphene photodetectors and diversity combining methods are accomplished resulting in practical SNR, BER and data rate characteristics and efficiency improvement ratios for diversity combining methods.

In Chapter-4, carbon nanotube nanoscale wireless optical communication receivers are modeled and analyzed communication theoretically. Firstly, in Section-4.1, the physical properties of carbon nanotubes are introduced and wide range of application areas are listed. Then, electronic properties are presented by introducing carbon nanotube field effect transistors. Similar to graphene photodetectors, the fundamental metrics of resistance, carrier velocity and capacitance are modeled specifying the performance of the transistor

as a photodetector. Furthermore, optical properties of carbon nanotubes are presented emphasizing the diameter dependence of optical absorption and transition frequencies. Next, in Section-4.2, carbon nanotube photodetector types such as carbon nanotube field effect transistor photoconductors, p-n junction photodiodes and Schottky Barrier carbon nanotube field effect transistor photodiodes are introduced. Then, in Section-4.3, the model of single walled carbon nanotube photodetector is presented in terms of equivalent circuit, photocurrent, noise and SNR. Then, in Section-4.4, various optical transmitter technologies are discussed which can be used in a broadcast carbon nanotube optical network presented in Section-4.5. The optimization of transmit power for the CNT broadcast network is analyzed in Section-4.6. Finally, in Section-4.7, SNR, BER and data rate performances of nanotubes are numerically analyzed giving practical achievable ranges. Furthermore, the improvement obtained with broadcast power optimization is discussed.

Finally, in Chapter-5, the conclusions of the thesis are given summarizing the main contributions and the future work.

CHAPTER 2

BACKGROUND ON WIRELESS OPTICAL COMMUNICATIONS

Radio and optical communication technologies are the two fundamental methods to transmit information wirelessly in a world of increasing significant demand for wireless technologies [152]. Radio communication uses the frequency spectrum extending from KHz to hundreds of GHz frequencies where the data transmission for our current technological devices such as television, wireless phones and radio operate. The optical communication covers the range from infrared (IR) to visible and UV spectrum. The electromagnetic spectrum is shown in Fig. 2.1.

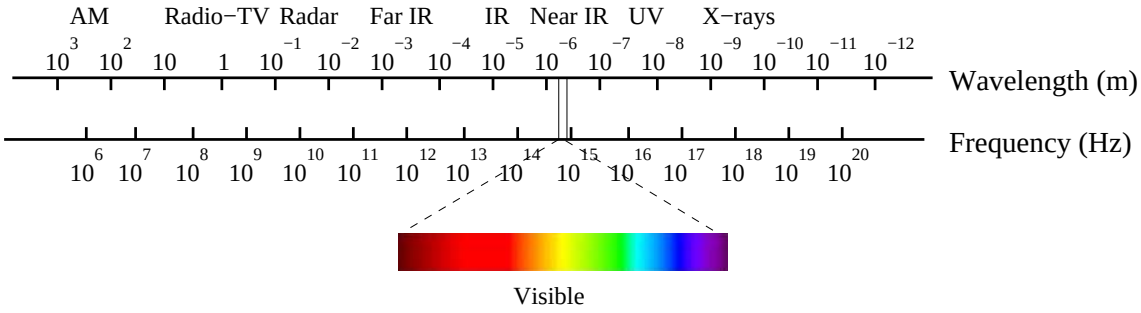

Figure 2.1: The electromagnetic spectrum showing RF and optical communication.

The radio spectrum is getting more congested every year making it a more expensive resource. Optical communications spectrum, e.g., IR, has various advantages compared with radio such as the availability of significant unregulated bandwidths, immunity to electromagnetic interference, security, locality, easy wireless deployment, low cost, small size and limited power consumption [152]. On the other hand, some disadvantages of optical communication links can be listed such as susceptibility to external blocking due to objects,

the noise of background illumination, high attenuation through air, fog and snow. Optical wireless communication technology is generally preferred for short range communications due to its advantages such as security, immunity to radio frequency interference and low cost whereas RF technology is preferred over longer distances for high mobility and bad atmospheric conditions.

The history of using optical signals to transmit information extends to antiquity, e.g., Homer argues about the use of optical signals to transmit a message in approximately 1200 B.C. [70]. The fire beacons lit between mountain tops enable to send information over long distances. In 1790's, Claude Chappe's optical telegraph has sent information over distances of hundreds of kilometers in minutes by changing the orientation of signaling arms on a large tower. The photophone shown in Fig. 2.2(a) and (b) invented by Alexander Graham Bell and Charles Sumner Tainter on 1880's transmits an audible signal over a distance of 213 m by modulation of the transmitted light with a mirror vibrated by the voice where the receiver is a selenium crystal converting the optical signal into an electrical current [15].

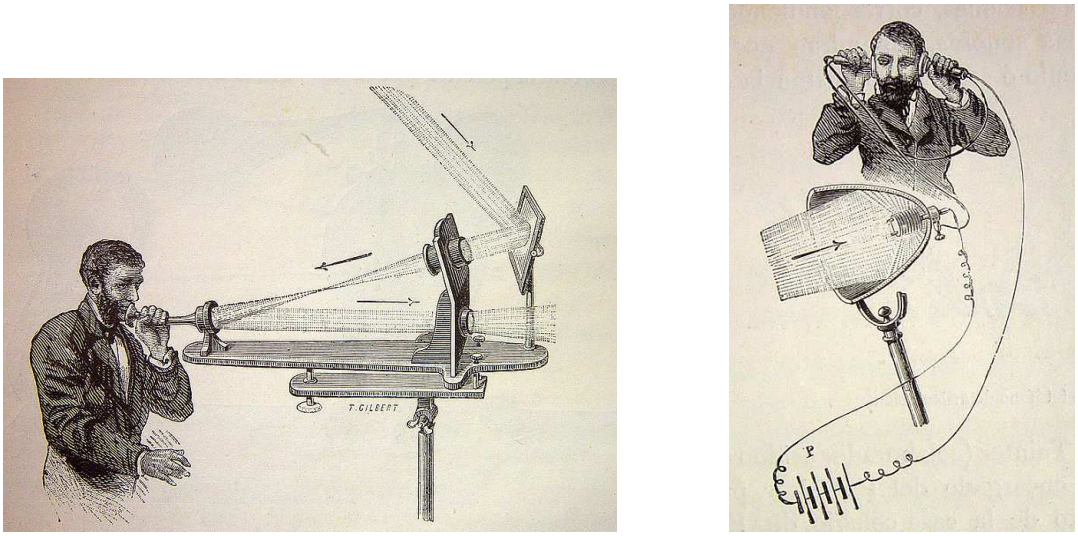

(a) (b)

Figure 2.2: Photophone invented by Alexander Graham Bell and Charles Sumner Tainter on 1880's with the illustration for (a) the transmitter, and (b) the receiver [15].

After F.R. Gfeller and U. Bapst have suggested IR for indoor communications in 1979,

IBM's first experimental works between 1978 and 1981 show that duplex IR links achieve 64 Kb/s data rate with phase shift keying (PSK) modulation and 256 KHz carrier frequency. Today, the technological developments in optical sources, modulation and ultrafast detectors have led to the increased data rates up to 40 Gb/s and beyond [39]. Photoreceiver modules supporting data rates over 40 Gb/s [55] and 100 Gb/s [11] are designed. The free space optical wireless communication experiments give 1.28 Tbit/s $\approx 32 \times 40$ Gb/s transmission capacity over a distance of 210 m [35] and 16-channel 10 Gb/s capacity over 2.16 km [31] with wavelength division multiplexing (WDM).

The developments in nanotechnology science have also led to applications regarding modern photodetectors with nanoscale dimensions which are described next.

2.1 Nanoscale Wireless Optical Communications

Nanoscale photodetectors with applications in nanoscale communications have gained significant attention from the researchers recently due to various advantages unique to their nanoscale nature [151]. Ultrafast, tunable and high performance nanoscale graphene (2D) and carbon nanotube (1D) photodetectors reach hundreds of GHz bandwidths [148, 188] as will be described in the next chapters which are the main subjects of the thesis.

Furthermore, nanoscale light sources and detectors as optical antennas are discussed as one of the methods for constructing communication units in a nanoscale communication architecture [3]. Moreover, optical nanoscale interconnects or networks on chips can replace the electrical counterparts with advantages of high bandwidth, low latency, scalability and low energy consumption [63]. Therefore, nanoscale optical communication architectures are of the fundamental importance for next generation communication technologies. In this thesis, the modeling of the nanoscale optical receiver and the communication theoretical analysis experienced by the receiver are given special importance.

In addition to graphene and nanotube, there are other nanoscale building blocks for

photodetector applications which deserve to be discussed briefly. The nanoscale quantum dot infrared photodetectors (QDIPs) denoted as zero dimensional (OD) objects have normal incident light detection capability, low dark current, long excited-state lifetime, high photoconductive gain, high temperature and voltage-tunable multi-spectral operation [104, 162]. Quantum well infrared detectors (QWIPs) have the mature processing technology for the material GaAs leading to low cost, flexibility in high speed and multi-color applications [163].

Nanowire (NW) photodetectors with one dimensional (1D) structures are fabricated from metal-oxides, e.g., ZnO, group II-VI compounds like $\mathrm{Hg}_{1-x}\mathrm{Cd}_x Te$, group III-V compounds such as InP, GaAs, AlGaAs and InGaAs, group IV compounds such as Si and Ge and group VI compounds such as Se and Te [166]. NW photodetectors have several advantages compared with bulk photodetectors such as possibility of dense device integration, sub-wavelength spatial resolution, enhanced light absorption in vertical arrays, high photosensitivity and gain.

Single photon detectors lead to high-sensitivity and high-resolution near-field imaging sensing the extremely low light powers emitted by nanoscale sources [19]. They succeed in measuring the diffraction pattern of single photons with sub-wavelength spatial resolution, small noise and small active area. Single photon detectors are implemented with photomultipliers, avalanche photodiodes, visible-light photon counters, superconducting nanowires, superconducting transition-edge sensors, quantum dots and semiconductor defects [66].

2.2 System Model

One of the most popular and important forms of data modulation at the transmitter is intensity modulation (IM). The data information modulates the instantaneous power of the transmitted energy at the transmission wavelength λ. The electrical data signal drives transmitter as input data signal. The optical receiver, i.e., photodetector, converts the optical into an electrical signal using direct detection technique (DD) such that the generated electrical

signal is proportional to the instantaneous power of the received optical signal. A general model for wireless IM channels and the communication system are shown in Fig. 2.3.

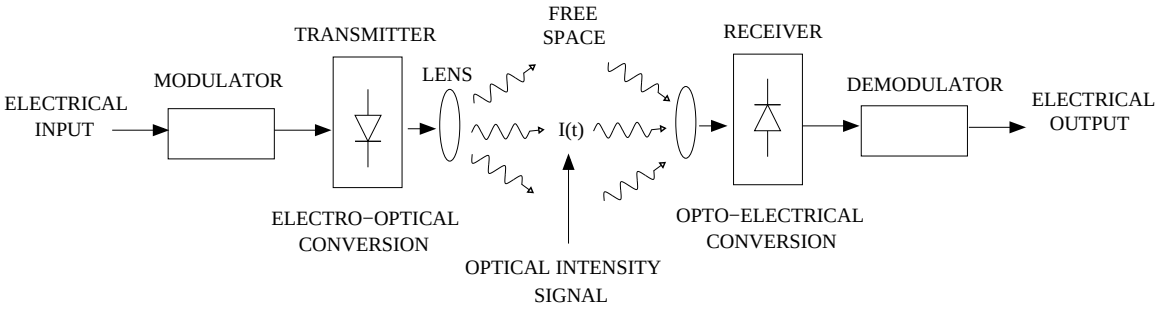

Figure 2.3: Block diagram of wireless IM/DD optical communication system [70, 152].

The information sent on the free space channel is the optical intensity modulated signal transmitted by generally light-emitting diode (LED), laser diode (LD) or various laser sources with dimensions ranging from macroscale to nanoscale [70,152]. The opto-electrical conversion, which is the main scope of the thesis in nanoscale, is generally performed by a reversed biased photodiode detector producing an electrical current which is a measure of the optical power impinging on the device. The detection of optical intensities results in the constraint that the information bearing intensity signal should be non-negative since the transmitted power can physically never be negative, i.e., $P(t) \geq 0$. The optical channel between transmitter and the receiver can be modeled by a linear, time-invariant baseband system with impulse response $h(t)$ as shown in Fig. 2.4 [79, 152].

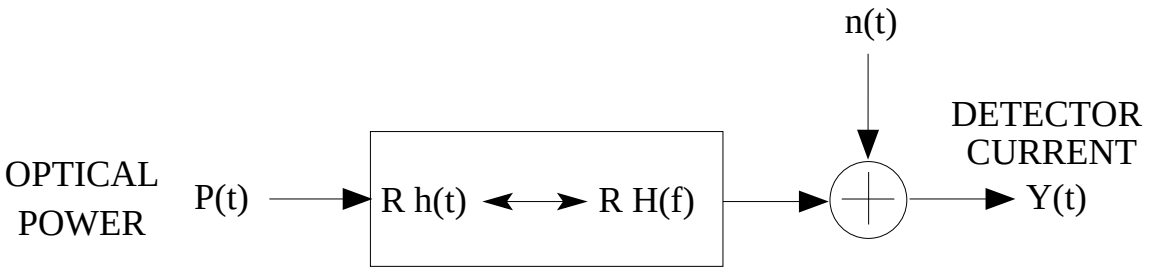

Figure 2.4: Wireless IM/DD optical communication channel model [152].

It includes the effects of multi-path, line-of-sight (LOS) and non-light-of-sight (non-LOS) propagation effects which are generally valid for indoor diffusive propagation. $P(t)$ is the instantaneous optical power of the transmitter where the average of the power is limited by a predetermined threshold, i.e., P_{max},

$$\lim_{T\to\infty} \frac{1}{2\,T} \int_{-T}^{T} P(t)\,\mathrm{dt} \leq\ P_{max} \tag{1}$$

The resulting output current $Y(t)$ can be written as,

$$Y(t)\ =\ \mathcal{R}\,P(t)\ *h(t)\ +\ n(t) \tag{2}$$

where $*$ denotes convolution, $\mathcal{R}$ is called responsivity of the detector and $n(t)$ is signal independent noise which is generally modeled as additive white Gaussian (AWGN) [79]. The noise includes the contributions coming from the internal mechanisms of the photodetector, external circuits like the contacts and the pre-amplifiers and the background light noise.

The responsivity of a photodetectors is one of the most important factors determining its efficiency. For a photodetector, under the saturation limit, i.e., $P_r(t) \leq P_{r,sat}$, the generated photocurrent, i.e., $I_{ph}(t)$ depends linearly on the input optical received power $P_r(t)$ with the relation,

$$I_{ph}(t)\ =\ \mathcal{R}\,P_r(t) \tag{3}$$

where $\mathcal{R}$ is the detector responsivity in units of (A/W). It depends on the photodetector type, device geometry and the wavelength of the modulated optical carrier. In some detectors, e.g., avalanche detectors, it also depends on the output voltage of the photodiode in addition to the wavelength.

Besides that, a similar metric of photodetectors is the *internal quantum efficiency*, i.e., η_i, which can be defined as the ratio of the count of the absorbed photons to the carriers of the generated current,

$$\eta_i\ =\ \frac{I_{ph}\,/\,q}{P_a(t)\,/\,h\nu} \tag{4}$$

where $P_a(t)$ is the absorbed power, $P_a(t) \,/\, h\nu$ is the number of absorbed photons, $I_{ph} \,/\, q$ is the number of generated carriers, h is the Planck's constant, $\nu = c \,/\, \lambda$ is the optical carrier frequency and λ is the wavelength of the light. A similar metric, i.e., the external quantum efficiency η_e, is closely related to the responsivity in terms of dependence to the number of incident photons not the absorbed photons by the following relation,

$$\eta_e = \frac{I_{ph} \,/\, q}{P_r(t) \,/\, h\nu} = \mathcal{R}\frac{h\nu}{q} \tag{5}$$

For photodetectors with internal gain g, i.e., photoconductors, phototransistors, avalanche photodiodes, the signal current, i.e., $I_{phg}(t)$, is amplified with the gain g as the following,

$$I_{phg}(t) = g\, I_{ph}(t) \tag{6}$$

Therefore, *intrinsic responsivity* is defined as $\mathcal{R}_0 = \eta_e\, q \,/\, h\nu$ for photodetectors with gain where the responsivity becomes

$$\mathcal{R} == g\, \mathcal{R}_0 = g\, \eta_e\, q \,/\, h\nu \tag{7}$$

For photodetectors without internal gain, e.g., p-n junction based diodes, Schottky photodiodes, $I_{phg} = I_{ph}$ and $\mathcal{R} = \mathcal{R}_0$.

Under ideal conditions, i.e., all of the incident photons are absorbed and converted into the carrier in the external circuit, $\eta_e = 1$ and $\mathcal{R} = q \,/\, h\nu$. However, in real photodetectors, the responsivity is lower than the ideal value due to various reasons such as part of the power is absorbed by the photodetector (with absorption coefficient α), part of the power is reflected due to dielectric mismatch, some power is absorbed to regions where a useful current is not obtained and some ratio of the power is transmitted without absorption [58].

The absorption coefficient (or attenuation coefficient) α depending on the unique interaction of the semiconductor material with the incoming optical electromagnetic wave specifies how much light is absorbed as the incident light propagates through the semiconductor medium of the detector. For example, the optical power density of the light propagated inside the medium with depth d can be given by $P(d) = P(0)\exp(-\alpha d)$ where

P_0 is the density at the entrance of the medium. Absorption coefficient depends on the imaginary part of the complex dielectric function as the following,

$$\alpha = \frac{4\,\pi\kappa}{\lambda} = \frac{\varepsilon_i(\nu)\,2\,\pi\,\nu}{n_d\,c} \tag{8}$$

where $\kappa = \varepsilon_i(\nu)\,/\,2\,n_d$ is the imaginary part of the complex index of refraction, $\varepsilon_i(\nu)$ is the imaginary part of the complex dielectric function $\varepsilon_p(\nu) = \varepsilon_r(\nu) + i\,\varepsilon_i(\nu)$, n_d is the refractive index [78]. The unit of α is generally given in terms of m^{-1}. The absorption length is defined as $L_\alpha \equiv 1\,/\alpha$, i.e., the minimum length of the absorption region to absorb most of the light. However, as the absorption length increases the time for the carriers to reach the contacts, i.e., the transit-time, increases by lowering the dynamic performance.

The responsivity, absorption coefficient and quantum efficiency are features depending on the wavelength of the optical excitation. The example responsivities and external quantum efficiencies of conventional photodetectors are seen in Fig. 2.5(a) and (b). The corresponding InGaAs p-i-n photodiode has a cutoff frequency of 3 GHz [58]. Si trap detector has an almost unity quantum efficiency [72]. Furthermore, the ideal responsivity curve where $\mathcal{R} = q\,/\,h\nu$ is shown in the figure.

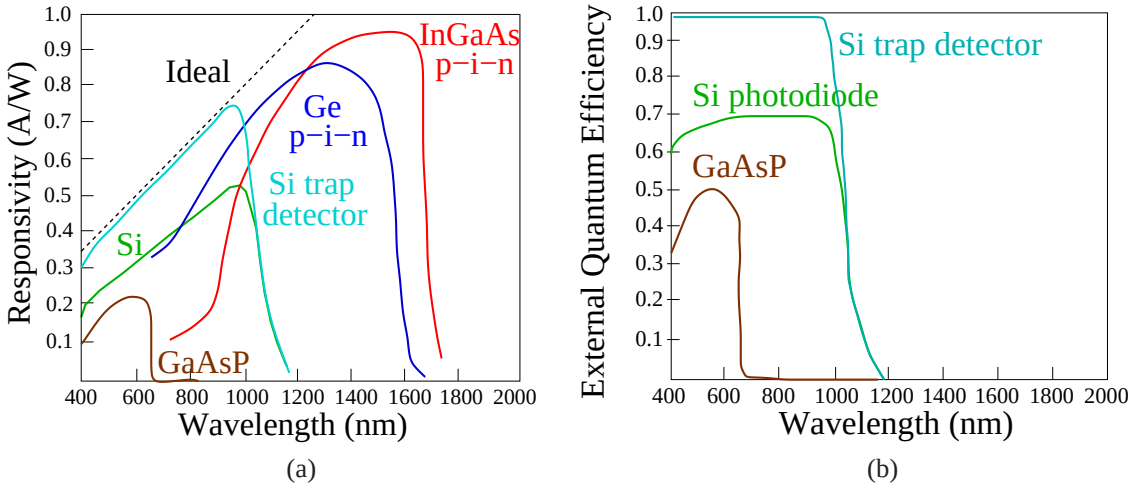

Figure 2.5: The performance of various photodetectors in terms of (a) the responsivity, and (b) the external quantum efficiency [18, 58].

2.3 Modulation

In IM/DD communication systems, the driver of the optical source uses the electrically modulated data signal to modulate the IR radiation emitted by the transmitter light source. The main optical modulation types used in optical communication systems can be categorized as *analog modulation* including amplitude modulation (AM) and frequency modulation (FM), *pulse modulation* including pulse position modulation (PPM), pulse amplitude modulation (PAM) and pulse duration modulation (PDM), *digital modulation* including amplitude shift keying (ASK), phase shift keying (PSK), frequency shift keying (FSK) and on-off keying modulation with return-to-zero (RZ-OOK) or non-return-to-zero (NRZ-OOK) on-off keying modulation, and *polarization shift keying modulation* where the polarization of the light is changed between two orthogonal states [81, 152].

In AM and FM, analog message signal modulates either amplitude or frequency of the intensity of light. FM modulation permits multiple users to access the optical channel using frequency division multiplexing (FDM) by using different frequency carriers.

In pulse modulation, the analog signal is sampled and the digital pulses are modulated in amplitude (PAM), position (PPM), or duration (PDM) with respect to the amplitude of the analog signal. AM and PAM are not preferred for wireless optical communications due to the additive noise [152]. If the analog signal is sampled and quantized, classical pulse code modulation (PCM) and coding techniques for PCM binary signals can be used to modulate the intensity of the light, e.g., the combination of PCM and Manchester coding. In PPM, the temporal positions of the optical intensity pulses are varied with respect to the modulating signal. PPM provides high power efficiency and its bandwidth efficiency and other performance metric can be combined by its variations such as wavelength shift keying pulse position modulation(WSK-PPM), differential pulse position modulation (DPPM), overlapping pulse position modulation (OPPM), multiple pulse position modulation (MPPM) and digital pulse interval modulation (DPIM) [152].

In digital modulation, which is the main scope of the thesis, the binary signal modulates

a sinusoidal carrier signal which is used to drive the emitter light source. However, a DC bias is generally added to make sure that the subcarrier signal is always positive. If the phase of the sinusoidal carrier is shifted, the modulation scheme is called PSK. On the other hand, if its frequency but not the phase or amplitude of the carrier is varied with respect to the amplitude of the modulating binary signal, then the modulation scheme is called FSK.

The fundamental and basic modulation technique used throughout the thesis, i.e., on-off keying modulation, is generally preferred in wireless optical communications due to its bandwidth efficiency and easiness to implement. A light source is simply switched between on and off states. The waveform of RZ-OOK scheme can be given as the following,

$$X(t) = \sum_{k} I_k \, P_{peak} \, p_{\gamma,T}(t \, - \, k \, T) \tag{9}$$

where $I_k = \{0, 1\}$ is the binary bit sequence, P_{peak} is the peak transmit power, γ is the duty cycle, T is the bit period, and $p_{\gamma,T}$ is the pulse with $p_{\gamma,T}(t) = 1$ for $0 \leq t \leq \gamma T$ and 0 otherwise. NRZ-OOK scheme can be obtained by setting $\gamma = 1$. The average optical power is half of the peak power for NRZ-OOK case.

Various forms of modulation techniques are shown in Fig. 2.6(a) and (b) where the non-negativity of the resulting emitted intensity signal should be paid attention.

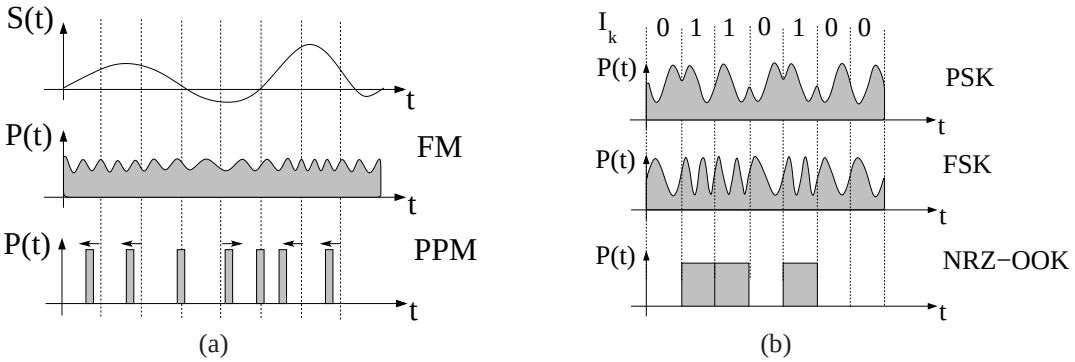

Figure 2.6: (a) FM and PPM intensity modulation schemes where $S(t)$ is the modulating analog information signal, (b) FSK, PSK and NRZ-OOK digital intensity modulation schemes where I_k is the binary information sequence [152].

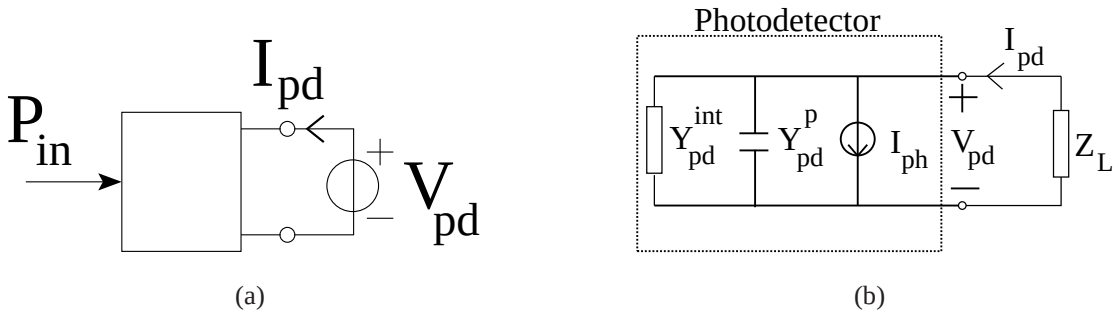

(a) (b)

Figure 2.7: (a) Black-box model and (b) Small signal equivalent circuit of a photodetector [58].

2.4 Dynamical Response

The dynamical characterization of the photodetectors is needed based on the fact that when the input power received by a photodetector varies too rapidly, the photocurrent does not follow its instantaneous value due to low-pass, delay mechanisms and the effect of the transit time of the photogenerated carriers. Therefore, small signal analysis for RC limited dynamic response, and carrier velocity analysis for transit-time limited dynamic response are necessary.

The dynamic response of the photodetectors can be analyzed based on their RC and transit time limited cut-off frequencies combined with their equivalent circuit analysis [58, 83]. Small signal equivalent circuit for photodetectors can be constructed by modeling the capacitive and resistive elements of the detector-external circuit combination [58]. The black-box and small-signal equivalent model of a general photodetector are shown in Fig. 2.7(a) and (b), respectively.

The black-box model includes a general constitutive relation

$$I_{pd}(t) = f(P_{in}(t), V_{pd}(t), \frac{d}{dt}, \lambda) \tag{10}$$

where $V_{pd}(t)$ is the detector voltage, and λ is the wavelength of the optical carrier and the time derivative implies a general memoryless relation. By using small signal analysis, i.e.,

modeling the variables as the following,

$$P_{in} = P_{in,0} + \mathrm{Re}(\widehat{P}_{in}\,\mathrm{e}^{j\omega t});\;\; I_{pd} = I_{pd,0} + \mathrm{Re}(\widehat{I}_{pd}\,\mathrm{e}^{j\omega t});\;\; V_{pd} = V_{pd,0} + \mathrm{Re}(\widehat{V}_{pd}\,\mathrm{e}^{j\omega t}) \quad (11)$$

where $P_{in,0}$, $I_{pd,0}$ and $V_{pd,0}$ are DC values, ω is the light angular modulation frequency, the following small-signal relation is obtained,

$$I_{pd}(\omega) = \left(Y_{pd}^{int}(\omega) \,+\, Y_{pd}^{p}(\omega)\right) \widehat{V}_{pd}(\omega) \,+\, \widehat{I}_{ph}(\omega) \quad (12)$$

where $\mathcal{R}(\omega)$ is the small-signal responsivity, $Y_{pd}^{int}(\omega)$ and $Y_{pd}^{p}(\omega)$ are the intrinsic and parasitic admittances, respectively, and $\widehat{I}_{ph}(\omega) = \mathcal{R}(\omega)\widehat{P}_{in}(\omega)$ is the signal photocurrent phasor as shown in Fig. 2.7(b) [58]. Assuming the equivalent capacitance of the circuit is C_{eq} and the equivalent resistance is R_{eq}, the phasor of the current on the load can be found as the following,

$$\widehat{I}_L(\omega) = -\frac{\widehat{I}_{ph}(\omega) R_{eq} \,/\, R_L}{1 \,+\, j\,\omega\, R_{eq} C_{\,eq}} \quad (13)$$

Then, the RC-limited cut-off frequency, i.e., f_C equals to $1 \,/\, 2\pi R_{eq} C_{eq}$.

RC-limited cut-off frequency depends on the device geometry and external factors. On the other hand, intrinsic transit-time limited cut-off frequency, i.e., f_{tr}, is found by using the saturation velocity of the carriers (holes and electrons) and the depletion region width depending on specific device geometries [58, 83]. The transit-time limited bandwidth is important where the depletion width for the photogenerated carriers is long enough, e.g., in a p-i-n photodiode, whereas its effect is negligible in small depletion widths of p-n photodiodes. The transit-time limited bandwidth is basically proportional to the transit time $\tau_{tr} \,\propto\, W_d \,/\, v_c$ elapsed for the photo-generated carriers traversing the distance to the metal contacts where W_d is the depletion width and v_c is the carrier velocity.

Various expressions of transit-time limited bandwidths are developed for different device geometries. For p-i-n photodiode with thick depletion region, i.e., $\alpha\, W_d \gg 1$ where α is the absorption constant, $f_{tr} \,\approx\, 0.443\, v_c \,/\, W_d \,\approx\, 1 \,/\, 2.2\, \tau_{tr}$ whereas for thin depletion region, i.e., $\alpha\, W_d \ll 1$, it is $f_{tr} \,\approx\, 3.5\, v_c \,/ 2\,\pi\, W_d \,\approx\, 1 \,/\, 1.79\, \tau_{tr}$ [58, 83]. Besides that, for

metal-semiconductor-metal detectors, the transit-time limited cut-off frequency is assumed to have the form $f_{tr} = 1 / 2\,\pi\,\tau_{tr}$ where $\tau_{tr} = \delta\,W_i / 2\,v_c$ is the transit time for the metal fingers with distance W_i and the correction factor δ is added [41]. The photoconductors are expressed to have $f_{tr} = 1 / 2\,\pi\,\tau_{tr}$ where τ_{tr} is the transit time for the carriers between ohmic contacts (given in (23)).

By combining the RC limited and transit-time limited cut-off frequencies, the resulting 3dB cut-off frequency is represented as the following [83],

$$\frac{1}{f_{3dB}^2} = \frac{1}{f_C^2} + \frac{1}{f_{tr}^2} \tag{14}$$

This general analysis introduced for p-n junction photodiodes can be applied for general class of photodetectors by finding their RC-limited and transmit-time limited cut-off frequencies.

2.5 Optical Receivers: Photodetectors

In this section, various type of photodetector structures encountered in graphene and carbon nanotube photodetector applications are analyzed in terms of their basic working principles and device geometries. P-n junction photodiodes, metal-semiconductor-metal Schottky barrier photodiodes and photoconductors are analyzed.

2.5.1 P-n Junction Photodiodes

P-n junction based photodiodes are some of the most popular and conventional photodiodes used in current wireless optical communications semiconductor technology. Avalanche photodiodes and phototransistors can also be included in p-n junction based photodiodes. These devices carry the photogenerated carriers to the external circuit by the junction reverse electric field. In p-n photodiode, the width of the depletion region, i.e., the region with ionized dopants and built-in electric field where the photo-excitation is performed, is small, and the incident photons absorbed in the adjacent diffusion regions lead to degraded frequency response performance. On the other hand, p-i-n photodiodes are more optimized

versions of p-n photodiodes such that the depletion region is widened which is placed between high doping layers. The photocurrent obtained from the uniform electric field of the wide intrinsic absorption region is not much effected from the diffusive components. The pin photodiode has high-bandwidth performance compared with p-n diodes.

In the next chapters, it is shown that the asymmetric metal-nanotube-metal Schottky photodiodes operate in reverse bias similar to a p-n junction based diode in terms of equivalent circuit and operation characteristics. Furthermore, it is observed that in graphene based photodetectors, the carriers are swept to the external contacts by the built-in potential developed in the metal-graphene interfaces. Therefore, the basic properties, circuit equations and the operating regimes of p-n junction based diodes are investigated in this section.

The basic device layout and the energy band diagram of a reverse biased p-i-n diode are shown in Fig. 2.8(a) and (b), respectively.

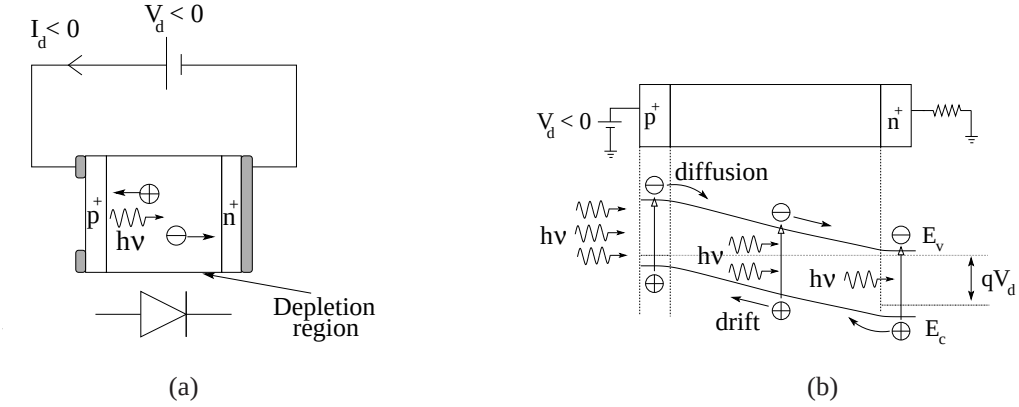

Figure 2.8: (a) Simplified scheme and (b) energy band diagram of a p-i-n photodiode in reverse bias [58].

The photodiode operating regime of the device is in reverse bias, i.e., $V_d < 0$, and the photocurrent $I_d < 0$ as shown in Fig. 2.8(a). The main contribution of the photocurrent is the drift current of the carriers in the depletion region and the minor current comes from diffusive components as shown in Fig. 2.8(b). By considering the reflectivity R of the upper surface, absorption coefficient α and the internal quantum efficiency η_i, a basic observation

for the responsivity is as the following,

$$\mathcal{R} = \frac{q}{h\,\nu}\,\eta_i\,(1 - R)\,(1 - \mathrm{e}^{-\alpha W}) \tag{15}$$

where W is the width of the depletion region and $(1 - R)\,(1 - \mathrm{e}^{-\alpha W})$ is the total absorbed power in the depletion region.

The performance of p-n junction diodes can be analyzed by using their equivalent circuits. The equivalent circuit of p-n junction photodiode is shown in Fig. 2.9 where R_d is the parallel diode resistance or shunt resistance, C_d is the intrinsic diode capacitance, I_{ph} is the photocurrent, C_p is the external parasitic capacitance, R_s is the series resistance, i.e., parasitic or contact resistance, ohmic losses in bulk regions and R_{eq} is the equivalent series resistance of R_s and the pre-amplifier circuit connected to the photodetector output. The diode is the ideal diode with ideality factor $1 \leq n \leq 2$ which depends on carrier generation and recombination in the depletion region. Then, the current-voltage relationship

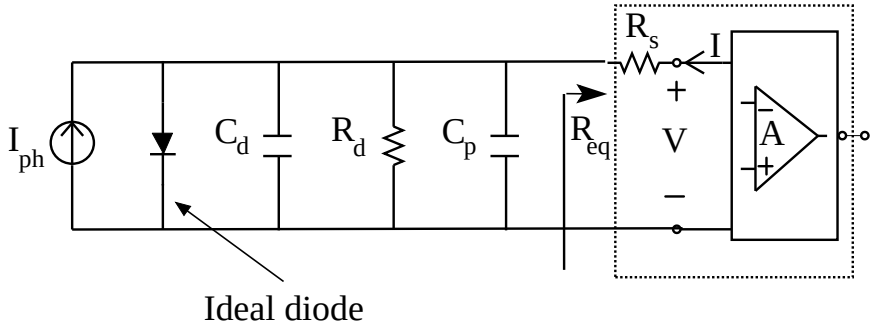

Figure 2.9: Simplified equivalent circuit of a p-n junction photodiodes.

of a p-n junction diode can be represented by the modified Shockley diode equation as the following

$$I = \frac{V - I\,R_s}{R_d} + I_d\,\left[\exp\left(\frac{q\,(V - I\,R_s)}{n\,\kappa\,T}\right) - 1\right] - I_{ph} \tag{16}$$

where I_d is the saturation current, i.e., the dark current of the photodiode.

The region where $V < 0$ and $I < 0$ is denoted by the *photodiode region* while the region $V > 0$ is called the *photovoltaic region* such that it converts the optical energy

into electrical energy as shown in Fig. 2.10. In photovoltaic region, the output power, i.e., $P_{out} = V\,I = P_{max} = V_M \times I_M$ is maximized by adjusting the operating point.

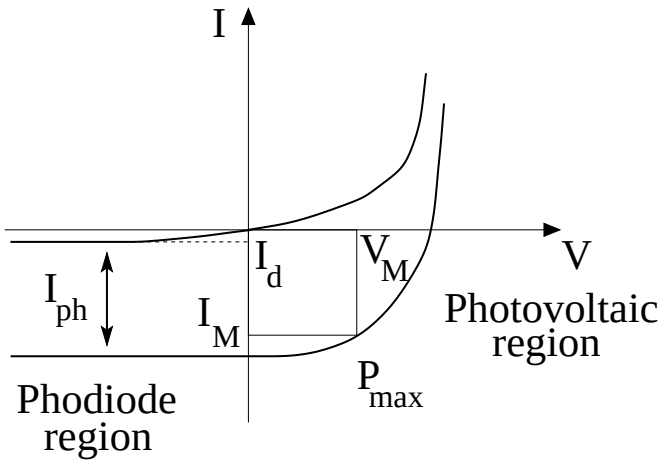

Figure 2.10: Photodiode and photovoltaic regions of operation of a p-n junction photodiode.

When the diode is reverse biased and the resistance $R_d \gg R_s$ which is generally the case for conventional photodiodes, the photodiode region of operation current can be found by using (16) as the following,

$$I = -I_d - I_{ph} \tag{17}$$

where the current is the sum of the dark and photocurrent.

2.5.2 Metal-Semiconductor-Metal Schottky Barrier Photodiodes

The rectifying behavior of p-n junction diodes can also be obtained with metal-semiconductor-metal (MSM) type photodiode geometries. For example, the p-type semiconductor, e.g., single walled carbon nanotube (SWNT) in air shows p-type behavior [110], is placed between asymmetric metal types, i.e., lower work function and higher work function metals, and at the contact with the lower work function a Schottky barrier is formed whereas the contact with the higher work function metal forms the ohmic contact [85, 115, 173].

MSM photodetectors offer large photosensitive surface area, very high performance speed, low capacitance and easy to integrate planar surfaces compatible with field effect

transistor (FET) technology [41,183]. An illustrative MSM photodetector device geometry is shown in Fig. 2.11. The interdigitated device geometry allows the carriers to be collected over a large area while leading to a very short inter-electrode distance for the carriers to traverse.

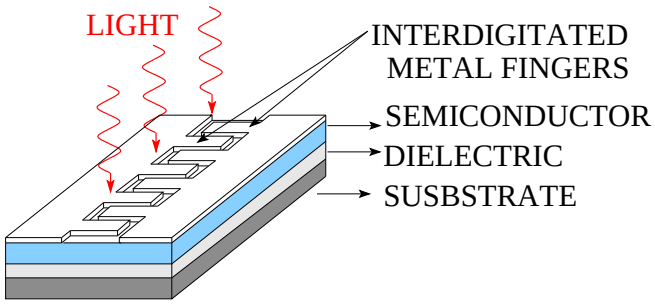

Figure 2.11: Interdigitated metal-semiconductor-metal (MSM) photodetector device [41, 152, 183].

The diode behavior formed due to Schottky barrier shows a majority carrier device behavior such that if the semiconductor is n-type, electrons and if the p-type, holes play the significant role in operation of the device. The illustrative energy-band diagram of MSM devices with Schottky contact at the source and ohmic contact at the drain for p-type semiconductor is shown for various bias and gate voltages in Fig. 2.12.

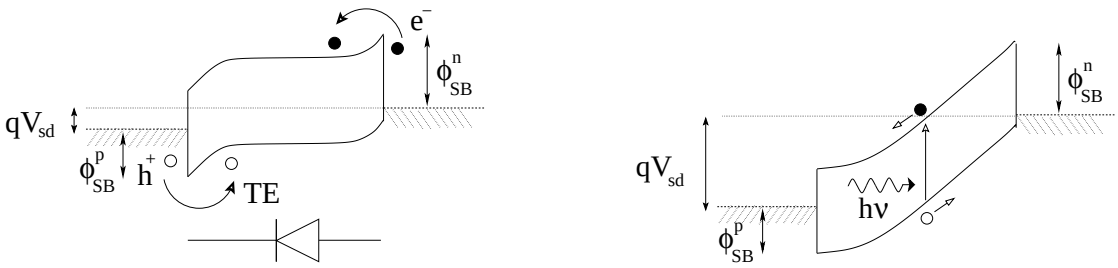

Figure 2.12: (a) Energy band diagram of asymmetric, i.e., Schottky contact - p-type semiconductor - ohmic contact, MSM device at reverse bias where full depletion not occurs showing the contributions due to thermionic emission (TE) current for holes (h^+) and electrons (e^-), (b) High reverse biased energy band diagram of the device with fully depleted scheme where collection of the photogenerated electrons and holes are shown.

Here the barrier heights Φ^p_{SB} and Φ^n_{SB} specify the thermionic emission (TE) components of the dark current for majority hole carrier and minority electron carrier, respectively. They can be found by using the following equality,

$$\Phi^p_{SB} = E_g + \chi - \phi_m; \;\; \Phi^n_{SB} = \phi_m - \chi \tag{18}$$

where E_g and χ are the semiconductor band-gap and the electron affinity, respectively, and ϕ_m is the metal work function [183]. For example, for SWNTs Φ^p_{SB} is equal to $\phi_{CNT} + E_g\,/\,2 - \phi_m$ where $\phi_{CNT} = \chi + E_g\,/\,2$ is the work function of carbon nanotube around 4.7-4.9 eV [109]. The work function of typical metals which are in the scope of the thesis and which are realized and analyzed for carbon nanotube contacts in the literature [33, 98, 103, 119, 135, 144, 171] are given in Table-2.1 .

Table 2.1: Work functions of different metals [33, 98, 103, 119, 135, 144, 171]

Metal	ϕ_m (eV)	Metal	ϕ_m (eV)
Ag	4.26	Ga	4.2
Al	4.1-4.3	Hf	3.9-4
Au	5.1-5.2	Nb	4.3
Ca	2.87	Ni	5.15
Cu	4.65	Pd	5-5.25
Cr	4.4-4.5	Pt	5.65
Fe	4.5	Ti	4.3-4.6

In order to obtain the rectifying diode behavior, the device should operate at reverse bias, i.e., $V_{ds} \leq 0$ and the gate voltage positive biased, i.e.,$V_g \geq 0$, such that the barrier for holes at the source is thick enough not to allow for tunneling current at reverse bias. In forward bias, the diode at the source operates in the forward bias mode. The region between the electrodes is depleted and the electric field is formed. The photocurrent saturates when the flat-band condition, i.e., the depletion region of the reverse biased junction at the source increases and reaches across the inter-metal distance.

The source drain current of the MSM device is given by

$$I_{ds} = I_d \left[\exp\left(\frac{q\,V_{ds}}{n\,\kappa\,T} \right) - 1 \right] \tag{19}$$

where V_{ds} is the forward bias, n is the ideality factor, the dark or leakage current, i.e., I_d, of the MSM device based on thermionic emission theory is given by

$$I_d = A\,A_n^*\,T^2 \exp\left(-\frac{\Phi_{SB}^n}{\kappa\,T}\right) + A\,A_p^*\,T^2 \exp\left(-\frac{\Phi_{SB}^p}{\kappa\,T}\right) \tag{20}$$

where A is the contact area at the source and drain, A_n^* and A_p^* are the effective Richardson constants for electrons and holes, respectively, T is the temperature and κ is the Boltzman constant [41, 172, 173, 183]. In the case of Schottky contact at the source and the ohmic contact at the drain with $\Phi_{SB}^n > \Phi_{SB}^p$ as shown in Fig. 2.12 and p-type semiconductor with hole majority carriers, the dark current can be approximated by the following [85,115,173],

$$I_d \approx A\,A_p^*\,T^2 \exp\left(-\frac{\Phi_{SB}^p}{\kappa\,T}\right) \tag{21}$$

The small signal equivalent circuit of MSM photodetectors are similar to the p-n junction diodes as shown in Fig. 2.13. R_{pd} is the leakage resistance, R_f is the series metal finger resistance, C_p is the parasitic capacitance including the ground-finger and the pads, C_{ext} and L_{ext} are the external circuit parameters including the wires and the amplifiers and R_L is the load resistance. The circuit can be analyzed converting to the small signal equivalent circuit defined for general photodetectors in Fig. 2.7(a) and (b).

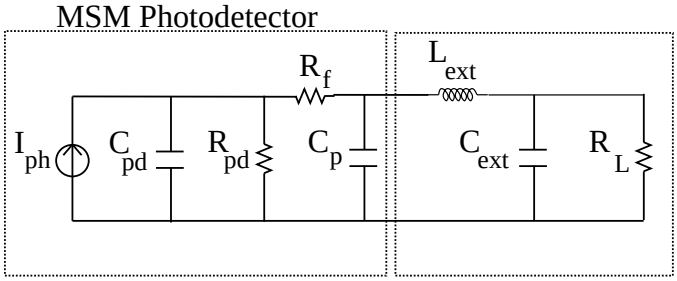

Figure 2.13: Small signal equivalent circuit of MSM photodetectors [41, 183].

Then, by finding the equivalent capacitance and resistance and the carrier transit time, cut-off frequencies f_C and f_{tr} can be found [41, 183].

2.5.3 Photoconductors

Photoconductive or photoresistor detector is based on photoconductivity such that the incident radiation changes the electrical conductivity of the material. The conductivity of the insulator or semiconductor material increases under incident optical light due to photogenerated carriers. The generated carriers are swept to the external circuit, e.g., to a resistor R_L, by the approximately uniform electric field induced by the applied voltage bias V_b. A simple device geometry of photoconductive detector and the band diagram showing the intrinsic and extrinsic excitation of the carriers are shown in Fig. 2.14(a) and (b).

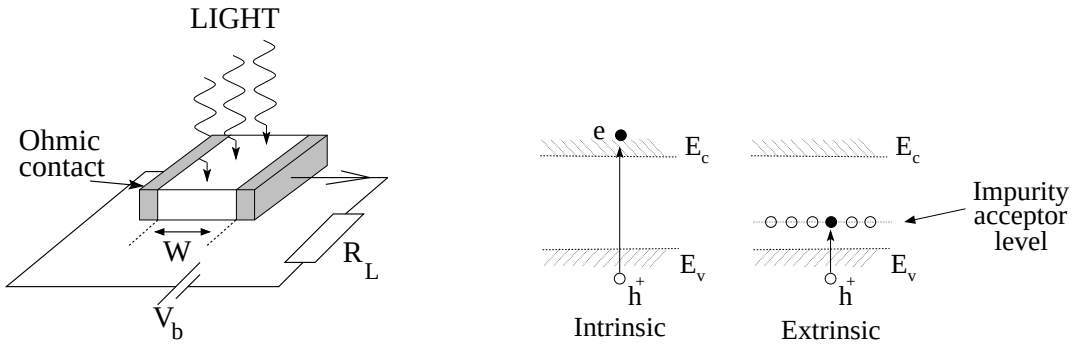

Figure 2.14: (a) Simplified scheme and geometry, and (b) of a photoconductive detector and (b) the band diagram showing the intrinsic and p-type extrinsic photoconductivity [107, 183].

The intrinsic photoconductivity is due to the electron-hole pairs generated by band-to-band absorption of the incident photons. For the extrinsic photoconductivity, the optical transitions are between impurity levels within the bandgap and the band edge. For example, in a p-type extrinsic photoconductor, the impurity acceptor level is above the valence-band and electrons are excited to these levels upon incident light as shown in Fig. 2.14(b). The obtained signal can be detected through a load resistor as photovoltage or photocurrent.

A photoconductor is a photodetector with gain depending on the properties of the semiconductor and electrical contacts. The gain of a conventional photodetector is represented

as the following,

$$g \;=\; \frac{\tau_c}{\tau_{tr}} \tag{22}$$

where τ_c is the dominating excess carrier recombination lifetime and τ_{tr} is the transit time of the carriers between ohmic contacts which can be found as

$$\tau_{tr} \;=\; \frac{W}{v_c} \;=\; \frac{W}{\mu_c\, E} \;=\; \frac{W^2}{\mu_c\, V_b} \tag{23}$$

where $v_c = \mu_c\, E$ is the carrier velocity, $E \;=\; V_b \,/\, W$ is the uniform electric field along the photoconductor and μ_c is the mobility of the dominating carrier, i.e., either electron or hole. The resulting photocurrent with gain g, i.e., I_{phg}, and the responsivity $\mathcal{R} \;=\; g\,\eta_e\, q \,/\, h\nu$ are given in (6) and (7), respectively.

The equivalent circuit of the photoconductor as shown in Fig. 2.15 is relatively simple compared with photodiodes and whose model is used in the next chapter while modeling metal-semiconductor-metal graphene ultrafast photodetectors.

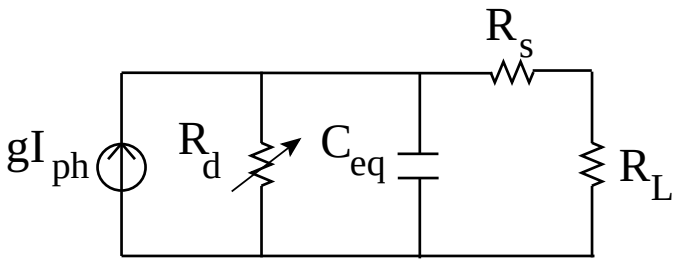

Figure 2.15: Small signal equivalent circuit of photoconductors [107].

The variable resistance R_d decreases upon illumination. The dark current resistivity of the detector is

$$\rho \;=\; \frac{1}{n_0\,\mu_n\, q \;+\; p_0\,\mu_p\, q} \tag{24}$$

where n_0 and p_0 are equilibrium concentrations of free electrons and holes, respectively, and μ_n and μ_p are their mobilities [177]. The change in resistance, i.e., ΔR_d, can be found by taking the derivative of (24) as the following,

$$\Delta R_d \;=\; -R_d\, \frac{q\,(\mu_n \;+\; \mu_p)\eta_e P_r\, \tau_c}{\sigma\, A_d\, L_d} \tag{25}$$

where A_d is the active area, L_d is the thickness, σ is the conductivity and τ_c is the carrier lifetime.

The other circuit components are the same as the models of p-n junction based devices, i.e., equivalent capacitance C_{eq}, series and load resistances R_s and R_L, respectively. Photoconductors are simpler than photodiodes and have lower operational speeds.

2.6 SNR and BER Analysis

SNR of optical communications systems are calculated by analyzing the distinct noise sources encountered in photodetector receivers [88]. The noise can also result from input light due to laser noise, the noise of optical amplifier, background optical noise coming from external sources of light and interference noise from other sources of communication in the same wireless optical communication network. The noise analysis of carbon nanotube and graphene optical receivers in this thesis concentrates on the noise contributions coming from the photodetector analyzing the fundamental limitations of the photodetector. Therefore, fundamental photodetector noise types effecting the performance are analyzed in this section.

The fundamental detector noise types specifying the performance are the thermal noise from resistive elements, the shot noise due to the dark current, quantum nature of the incoming photons and 1/f noise, i.e., flicker noise, and generation-recombination noise specific to the photoconductors.

Thermal noise arises from the resistance of the photodetector, load and pre-amplifier. Thermal noise is modeled as independent from the optical signal and having a Gaussian distribution [70]. The power spectral density of a noise random process, i.e., $S_n(f)$ can be used to find the root mean square value of the noise current, i.e., $\overline{i_n^2}$, as the following,

$$\overline{i_n^2} = \int_0^\infty S_n(f)\, df \tag{26}$$

Then, the power spectral density and the noise current root mean square value of thermal

noise process of a resistive element R (Ω) is expressed as the following,

$$S_{n,th}(f) = \frac{4\,\kappa\,T}{R} \quad (\text{A}^2/\text{Hz}); \;\; \overline{i^2_{n,th}} = \frac{4\,\kappa\,T\,B}{R} \quad (\text{A}^2) \tag{27}$$

where κ is the Boltzmann constant, T (K) is the temperature and B (Hz) is the bandwidth. The pre-amplifier resistance noise is important in photodetector amplifications. For example, if a low resistance amplifier is used, an excessive amount of thermal noise is added to the photocurrent signal. High impedance pre-amplifiers prevent large thermal noise but bring a lower dynamic response performance. Transimpedance pre-amplifiers improve both the noise and detector bandwidth performance.

The second fundamental source of noise is shot noise due to the discrete nature of charge carriers. It has dark current and quantum noise components. The carriers leading to the dark current traverse the potential barrier of the p-n junction of the photodiode in a random fashion leading to the shot noise. The shot noise is modeled as identically shaped decaying pulses with Poisson distribution in time domain. The power spectral density of Poisson distributed random process is given by Carson's theorem [156]. Therefore, the dark current which flows in the photodetector even when there is no incident light, i.e., i_d, brings a power spectral density and root mean square current of the following,

$$S_{n,d}(f) = 2\,q\,i_d \quad (\text{A}^2/\text{Hz}); \;\; \overline{i^2_{n,d}} = 2\,q\,i_d\,B \quad (\text{A}^2) \tag{28}$$

where q (Coloumbs) is the electric charge.

The quantum noise component of the shot noise results from the probabilistic generation of carrier pairs in the space charge region due to the quantum nature of photons arriving at the detector. A photocurrent of i_{ph} results in the following quantum shot noise spectral density and root means square photocurrent,

$$S_{n,p}(f) = 2\,q\,i_p \quad (\text{A}^2/\text{Hz}); \;\; \overline{i^2_{n,p}} = 2\,q\,i_p\,B \quad (\text{A}^2) \tag{29}$$

where the form of the shot noise coming from the photocurrent and dark current is the same.

For photodetectors with internal gain, i.e., photoconductors, phototransistors, photomultiplier or avalanche photodiode, the signal and dark currents are amplified by the gain g, i.e.,

$$i_{pg} \;=\; g\, i_p \;=\; g\, \eta_e\, q\, P_r \,/\, h\, \nu; \qquad i_{dg} = g\, i_d \tag{30}$$

where i_d is the unamplified dark current and $i_p = \eta_e\, q\, P_r \,/\, h\, \nu$ is the unamplified photocurrent. Then, the shot noise is also multiplied through the multiplication of noise electrons by transforming into excess noise as the following,

$$\overline{i^2_{n,p,d}} = 2\, q\, i_{p,d}\, B\, g^2\, F \;=\; 2\, q\, i_{pg,dg}\, B\, g\, F \qquad (\mathrm{A}^2) \tag{31}$$

where $F \;>\; 1$ is the excess noise factor which depends on device geometry, type and the amount of gain [107]. In photoconductors, photomultipliers and avalanche photodiodes, the gain g is random where the excess noise factor is expressed as $F \;=\; \overline{g^2} \,/\, (\overline{g})^2$. Both g and F are unity for photodetectors with unity internal gain and the shot noise in (31) transforms into (28) and (29).

Flicker noise is important when the operating frequency of the device is very low such that the power spectrum of the noise falls with frequency according to 1/f proportionality. The source of the noise is considered as the imperfect ohmic contacts, surface-state traps and dislocations [177]. In this thesis, the analyzed carbon nanotube and graphene photodetectors operate at frequencies larger than 1 KHz where the flicker noise effect can be ignored.

Generation-recombination (g-r) noise is known as the shot noise in photoconductors due to random fluctuations in the carrier number by the statistical nature of the generation and recombination of carriers [107]. The gain g in a photoconductor shown in (22) leads to g-r noise of the excess noise form given in (31). It is equal to the ratio of carrier lifetime τ_c to transit time τ_r across the photoconductor where the lifetimes depend on the photoconductor properties, the contacts and the voltage. Then, the excess noise factor is found equal to 2 for photoconductive detectors [107] based on $F \;=\; \overline{g^2} \,/\, (\overline{g})^2 \;=\; \overline{\tau_c^2} \,/\, (\overline{\tau_c})^2$ with

Poisson distributed probability distribution of τ_c leading to the shot noise, i.e., g-r noise, as the following,

$$\overline{i^2_{n,p,d}} = 4\,q\,i_{pg,dg}\,B\,g \qquad (\mathrm{A}^2) \tag{32}$$

A noise equivalent circuit showing the main dominating noise sources, i.e., thermal and shot, in a photodetector is shown in Fig. 2.16.

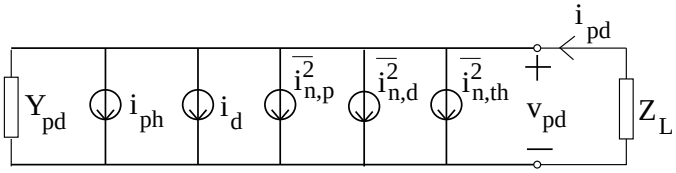

Figure 2.16: Noise equivalent circuit for a typical photodetector [58].

Assuming NRZ-OOK modulation is used throughout the thesis, SNR of IM/DD modulation can be computed by using the ON state of the information transmission with incident power P_r and responsivity of the photodetector $\mathcal{R}$ as the following [58, 79],

$$SNR = \frac{(\mathcal{R}\,P_r)^2}{2\,q\;(i_p + i_d)\;B + 4\,\kappa\,T\,B\,/\,R_{eq}} \tag{33}$$

where R_{eq} is the equivalent resistance contributing to the thermal noise. If the photoconductor has internal gain, then, SNR is represented as the following,

$$SNR = \frac{(g\,i_p)^2}{2\,q\;(i_p + i_d)\;B\,g^2\,F\; + 4\,\kappa\,T\,B\,/\,R_{eq}} = \frac{(\mathcal{R}\,P_r)^2}{2\,q\;(i_{pg} + i_{dg})\;B\,g\,F\; + 4\,\kappa\,T\,B\,/\,R_{eq}} \tag{34}$$

which transforms into (33) when there is no photodetector gain and where i_{pg}, i_{dg} and $\mathcal{R}$ are defined in (30) and (7), respectively.

BER of NRZ-OOK modulation can be found by using the on state SNR as the following [149]. Assume that for the on state the output Y_{on} equals to $S + n$ with $SNR = S^2\,/\,\sigma_n^2$ and for the off state $Y_{off} = n$. Assuming the noise is AWGN, the probability of error when the signal is on can be found as the following,

$$P(e\,|\,S_{on}) = \int_{-\infty}^{S/2} \frac{1}{\sqrt{2\,\pi\,\sigma_n^2}} \exp\left[-\frac{(r-S)^2}{2\,\sigma_n^2}\right] \mathrm{d}r \tag{35}$$

After change of variables, it can be converted to the following,

$$P(e \,|\, S_{on}) = \int_{\frac{S}{2\sigma_n\sqrt{2}}}^{\infty} \frac{1}{\sqrt{\pi}} \exp\left(-x^2\right) \, \mathrm{d}x = \frac{1}{2}\mathrm{erfc}\left(\frac{\sqrt{SNR}}{2\sqrt{2}}\right) \tag{36}$$

where erfc$(.)$ is the complementary error function defined as the following,

$$\mathrm{erfc}(x) = \frac{2}{\sqrt{\pi}} \int_{x}^{\infty} \exp\left(-x^2\right) \, \mathrm{d}x \tag{37}$$

The similar result can be obtained for off state error such that $P(e \,|\, S_{off}) = P(e \,|\, S_{on})$. Then, BER can be found as the following,

$$BER = P_e = \frac{1}{2}\left(P(e \,|\, S_{off}) + P(e \,|\, S_{off})\right) = Q\left(\frac{\sqrt{SNR}}{2}\right) \tag{38}$$

where $Q(.)$ is the Q-function defined as $Q(x) = 0.5\,\mathrm{erfc}(x \,/\, \sqrt{2})$.

Depending on the size of the dark current shot noise, photocurrent shot noise and thermal noise, the corresponding noise-limited (NL) operating regions can be defined such that the detector behaves differently with respect to the input power. For example, assuming the photocurrent is large compared with dark current and the thermal noise is negligible, photocurrent shot-noise limited SNR, i.e., γ_s, can be found as the following,

$$\gamma_s = \frac{i_p^2}{2\,q\,i_p} = \frac{\mathcal{R}\,P_r}{2\,q\,B} \tag{39}$$

where the SNR depends linearly on the received optical power P_r. On the other hand, when the detector operated in thermal noise-limited regime, SNR, i.e., γ_t, can be represented as the following,

$$\gamma_t = \frac{i_p^2}{4\,\kappa\,T\,B \,/\, R_{eq}} = \frac{\mathcal{R}^2\,P_r^2\,R_{eq}}{4\,\kappa\,T\,B} \tag{40}$$

where SNR depends on the square of the received input power showing a larger improvement as the input power is increased. Therefore, the input power effects the photodetector performance depending on specific device geometry, dark current, light intensity and external circuit and should be kept in mind while designing optical communication architectures.

CHAPTER 3

GRAPHENE NANOSCALE WIRELESS OPTICAL COMMUNICATION RECEIVERS

Graphene with groundbreaking properties has tremendous impact in physical sciences as a two-dimensional atomic layer carbon sheet. Its unique electronic and photonic properties lead to applications such as transistors, graphene photodetectors (GPDs) and electronic circuit components. Metal-graphene-metal (MGM) GPDs with single or multi-layer graphene sheets are promising for future nanoscale optical communication architectures because of wide range absorption from far infrared to visible spectrum, fast carrier velocity and advanced production techniques due to planar geometry. Graphene being a 2D single-atomic-layer carbon atoms in a hexagonal honeycomb lattice has tremendous impact in physical sciences due to its significant and unique electronic, photonic and mechanical properties [57, 188]. It has high electron mobility and carrier Fermi velocity ($1/300$ of the speed of light), strong and fast broadband absorption from far infrared to visible and ultraviolet spectrum due to linear dispersion of Dirac electrons [20, 40, 170, 185]. Furthermore, absorption range is tunable with external gates, by band gap engineering forming narrow nanoribbons or applying strain and electric fields. Moreover, absorption from multiple graphene layers is additive. Combining its tremendous near-ballistic electronic transport and photonic properties with mechanical stability leads to devices operating at room temperature in nanoscale electronics and optoelectronics [20].

Graphene is the thinnest and the strongest material and with largest surface to weight ratio. The fundamental properties of graphene and carbon nanotube compared with high performances of conventional materials can be seen in Table-3.1. As can be observed, both

graphene and carbon nanotube are extremely strong with their high thermal and electrical conductivity.

Table 3.1: Graphene and CNT Properties [9, 28, 102, 129]

Property	Graphene	SWNT	Other
Young's modulus	0.5-1.5 TPa	0.3-1.5 TPa	0.2 GPa for strong steel
Tensile strength	1 TPa	30-200 GPa	1-2 GPa for strong steel
Thermal conductivity (Room Temp.)	4800-5300 W/(m.K)	6600 W/(m.K)	3300 W/(m.K) for diamond
Current capacity	$> 10^8$ A/cm^2	$> 10^9$ A/cm^2	10^7 A/cm^2 for Cu (d = 100 nm)
Carrier mobility (Room Temp.)	> 20000 cm^2/(V s)	20000-60000 cm^2/(V s)	450-1400 cm^2/(V s) for Si

The term graphene means the combination of *graphite* and the suffix *-ene* provided by Hanns-Peter Boehm who described carbon foils in 1962. The summary of the history of graphene emphasizing the important events especially related to graphene photodetectors can be seen in Table-3.2.

Its story beginning with graphite in ancient times extends to its modern generation and control in 20th century resulting in 40 GHz photodetectors, 100 GHz transistors, 1 GHz optical modulators and ICs like 10 GHz broadband frequency mixers. Graphite includes graphene sheets stacked together with interplanar spacing of 0.335 nm. Graphene is the structural building element of carbon materials such as graphite, charcoal, carbon nanotubes and fullerenes. 2D carbon can be wrapped up into zero dimensional fullerenes, rolled into one dimensional nanotubes, or stacked together into a form of 3D graphite.

Graphene is similar to carbon nanotube in terms of electronic transport properties, however, it is 2D, zero band gap and more easily produced by using advanced techniques due to its planar geometry leading to a competitive nanoscale material [6]. Graphene photodetectors combine the wide range of optical absorption and fast carrier transport properties

Table 3.2: Graphene Timeline

Year	Event
4000 BC	graphite paint used to decorate pottery in southeast Europe
1500	the discovery of natural graphite in England
1789	the name *graphite* by Abraham Werner derived from the Greek word *to draw*
1947	exploration of the theory of graphene to understand graphite by Wallace
1962	the term *graphene* introduced to describe monolayer flakes of reduced graphene oxide by Hanns-Peter Boehm
1966	growing of graphite multilayers by Hess et al.
1984	Dirac model of graphene described with massless quasi-particles by Semenoff
2004	extraction and isolation of single-layer graphene from bulk graphite by Geim and Novoselov (winners of 2010 Nobel Prize in Physics)
2004	the first graphene FET by Novoselov et al.
2008	the optical response of graphene-metal interfaces with photocurrent imaging technique by Xia et al. in IBM and Lee et al. in Max-Planck Inst. & EPFL
2008	the theoretical model of graphene nanoribbon transistor by Ryzhii et al.
2009	the demonstration of ultrafast and the first graphene FET photodetector operating at 40 GHz by Xia et al. in IBM
2010	graphene FET with 100 GHz cutoff frequency by Lin et al. in IBM
2011	the first graphene optical modulator at frequencies over 1 GHz by Liu et al.
2011	the first graphene IC of broadband frequency mixer operating at frequencies up to 10 GHz by Lin et al. in IBM

of graphene compared with conventional semiconductors. Recent metal-graphene-metal experiments show strong photocurrent response reaching internal quantum efficiency of 30% and hundreds of Gb/s data rate performance [124, 141, 188] due to photothermoelectric effect or built-in field of Schottky barriers at metal-graphene interfaces [89, 95, 124, 125, 140, 187, 194]. Furthermore, graphene phototransistors with p-i-n junctions show significant theoretical performance of optical responsivity, i.e., $\mathcal{R}$, and dark current detectivity [159–161]. Thus, ultrawideband response range and fast carrier response make graphene photodetectors potential candidates for future nanoscale optical networks.

Graphene with remarkable fast response in wide spectrum range suffers from low efficiency due to the low light-graphene interaction region, low absorption and the necessity to form multiple p-n junctions to sweep the charge carriers [44, 124, 188]. The efficiency is improved with the increased absorption of multi-layer graphene [161], increased electric field region and intensity sweeping the charge carriers with multiple finger devices and asymmetric metals [124] or amplified optical fields of adaptive resonance frequencies with plasmonic nanostructures placed near the contacts [44]. However, the improvement of efficiency by diversity combining multiple receivers with optimized geometrical placement of the same total area of single layer graphene is not considered in any of these articles.

Although graphene photodetectors are experimentally and theoretically analyzed in terms of photocurrent, dark current and cut-off bit rates, i.e., R_b, and graphene phototransistors are theoretically analyzed in terms of dark current detectivity, single-layer metal-graphene-metal photodetectors are not analyzed and modeled as nanoscale optical receivers in terms of fundamental performance metrics, i.e., SNR, BER and R_b.

In this thesis, for the first time, nanoscale single-layer symmetric metal-graphene-metal photodetectors are analyzed in terms of performance metrics for intensity modulation and direct detection non-return-to-zero on-off keying modulation showing tens of Gb/s achievable data rates with very low BERs. Performances of shot and thermal noise limited regimes are analyzed by emphasizing the width dependence and prevalence of thermal noise limited regime for practical power levels. Moreover, multi-receiver graphene photodetectors and parallel line-scan optical networking transmit topology are, for the first time, introduced which increase the efficiency of the detector as a novel method. Performance of maximal ratio and equal gain diversity combining methods are analyzed for multi-receiver devices. Nonuniform SNR of single receiver parallel line-scan spatial channels is both homogenized and improved by using multi-receiver devices with the same

total graphene area. Diversity methods and optimum receiver placement defined as max-min concave quadratic and linear optimization problems are solved with reformulation-linearization technique.

In this chapter, firstly physical and optical properties of graphene are introduced. Then, graphene photodetectors presented in the literature are discussed by emphasizing the device model used in the thesis. Graphene photodetectors are theoretically modeled in terms of SNR by using equivalent circuit, photocurrent and noise analyses. Signal-to-noise ratio, bit-error rate and data rate performances of nanoscale single-layer symmetric MGM photodetectors are analyzed for intensity modulation and direct detection modulation. Shot and thermal noise limited (NL) performance is analyzed emphasizing graphene layer width dependence and domination of thermal NL characteristics for practical power levels. Tens of Gb/s data rates are shown to be achievable with very low BERs for single receiver (SR) GPDs. Then, diversity methods for multi-receiver graphene photodetectors are analyzed improving the efficiency of symmetric graphene photodetectors. Furthermore, parallel line-scan optical nanonetwork topology is introduced. SNR performance of single receiver is improved with multi-receiver photodetectors by solving quadratic concave and linear optimization problems. The proposed models and optimization schemes are numerically simulated for practical power levels.

3.1 Properties of Graphene

Graphene is a single planar layer of sp^2-bonded carbon atoms packed into a honeycomb lattice as shown in Fig. 3.1(a) [131, 184]. The black balls are the carbon atoms with bond length of $a_{CC} \approx 0.142$ nm represented by the sticks. The lattice is characterized as a hexagonal Bravais lattice with two basis atoms and primitive vector of equilateral parallelogram with side $a_{CC}\sqrt{3}$. Primitive unit vectors a_1 and a_2 are represented by the following,

$$a_1 = (\frac{3\,a_{CC}}{2},\, \frac{a_{CC}\,\sqrt{3}}{2});\;\; a_2 = (\frac{3\,a_{CC}}{2},\, -\frac{a_{CC}\,\sqrt{3}}{2}) \tag{41}$$

where $|a_1| = |a_2| = a_{CC}\sqrt{3}$.

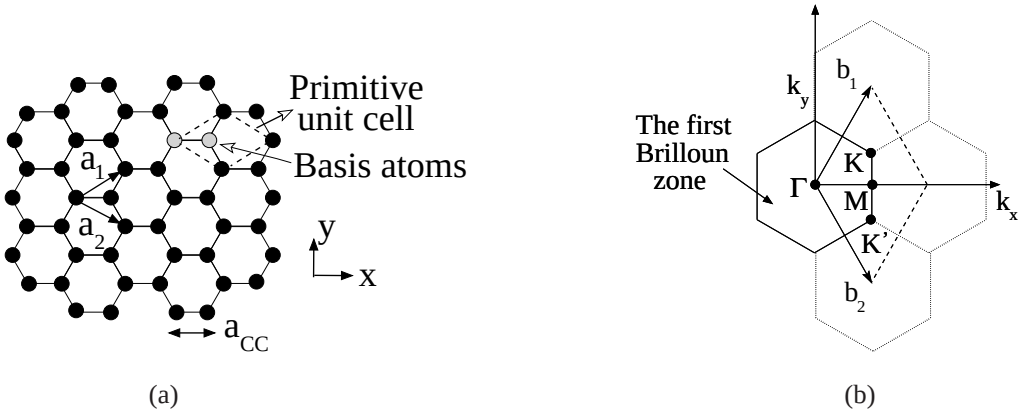

Figure 3.1: (a) The honeycomb lattice structure of graphene showing the primitive unit cell, basis atoms and primitive unit vectors, and (b) its reciprocal lattice showing the wavevector space and the symmetric points in the Brillouin [184].

3.1.1 Electronic Properties

The energy and wave-vector of electrons in a solid are closely related represented by the dispersion relation or band structure [184]. The energy-momentum dispersion relation of graphene could be understood by analyzing the π^* (conduction) and π (valence) energy bands since the $2p_z$ electrons in graphene form the π-bonds such that electron cloud is distributed normal to the graphene plane and these delocalized electrons specify the electronic properties of graphene and its 1-D rolled versions, i.e., CNTs. The energy band are calculated by using tight-binding as the following,

$$E(k_x,\, k_y) \,=\, \pm\,\gamma\,\sqrt{1 \,+\, 4\cos\left(\frac{3\,a_{CC}\,k_x}{2}\right)\cos\left(\frac{a_{CC}\,\sqrt{3}\,k_y}{2}\right) \,+\, 4\cos^2\left(\frac{a_{CC}\,\sqrt{3}\,k_y}{2}\right)} \tag{42}$$

where k_x and k_y denote the components of the wavevector in the reciprocal lattice of graphene as shown in Fig. 3.1(b) and γ, i.e., the nearest neighbor overlap energy, is between 2.7-3.3 eV, and generally taken as 3.1 eV [184]. The reciprocal lattice vectors are as the following,

$$b_1 = (\frac{2\,\pi}{3\,a_{CC}},\, \frac{2\,\pi}{a_{CC}\,\sqrt{3}});\;\; b_2 = (\frac{2\,\pi}{3\,a_{CC}},\, -\frac{2\,\pi}{a_{CC}\,\sqrt{3}}) \tag{43}$$

and there are six K and M-points in the Brillouin zone which are symmetric points for the dispersion relation of graphene with the center of the Brillouin zone defined by Γ. The highest and lowest energy states within valence and conduction bands, respectively, occur at the K-point which corresponds to $E = 0$ eV defined as the Fermi energy, i.e., $E_F = 0$ eV. The characteristics of electronic devices are characterized by the electrons around the Fermi energy. Therefore, the six K-points are the places where the conduction and valence bands touch. These points are called *Dirac points* and the dispersion around them is expressed as the linear dispersion equation as the following,

$$E_{k_x,k_y} = \pm \hbar \, v_F \sqrt{k_x^2 + k_y^2} \tag{44}$$

where $v_F \approx 10^6$ m/s is the Fermi velocity, i.e., the velocity at the Fermi energy. The plot of the linear dispersion around the Dirac points is called *Dirac cone* which is shown in 3.2(b). 3D valence and conduction energy bands with the Dirac cone, and the 2D contour of the valence band highlighting the symmetric points of the reciprocal lattice are shown in Fig. 3.2(a) and (c), respectively.

The Dirac cone, the connection between valence and conduction bands, or the absence of a bandgap at the Fermi energy make the graphene classified as zero-gap semiconductor. On the other hand, in a metal, Fermi energy is generally in the conduction band while in a semiconductor, it is inside the finite band-gap between valence and conduction bands.

The intrinsic graphene is a zero-gap semiconductor resulting zero effective mass for electron and hole carriers. They behave like relativistic particles called *Dirac fermions* described by the Dirac equation. Traveling with a constant speed and showing the characteristics of the photons in a condensed-matter system make the graphene an area of the observation of relativistic effects such as quantum Hall effect (QHE), even at room temperature, and Klein tunneling over high and wide potential barriers making the graphene powerful to the impurity and disorder potentials.

The transport studies on graphene generally use single-layer graphene field effect transistor geometry with modulating gate voltage as shown in Fig. 3.3 [43,164]. The exfoliated

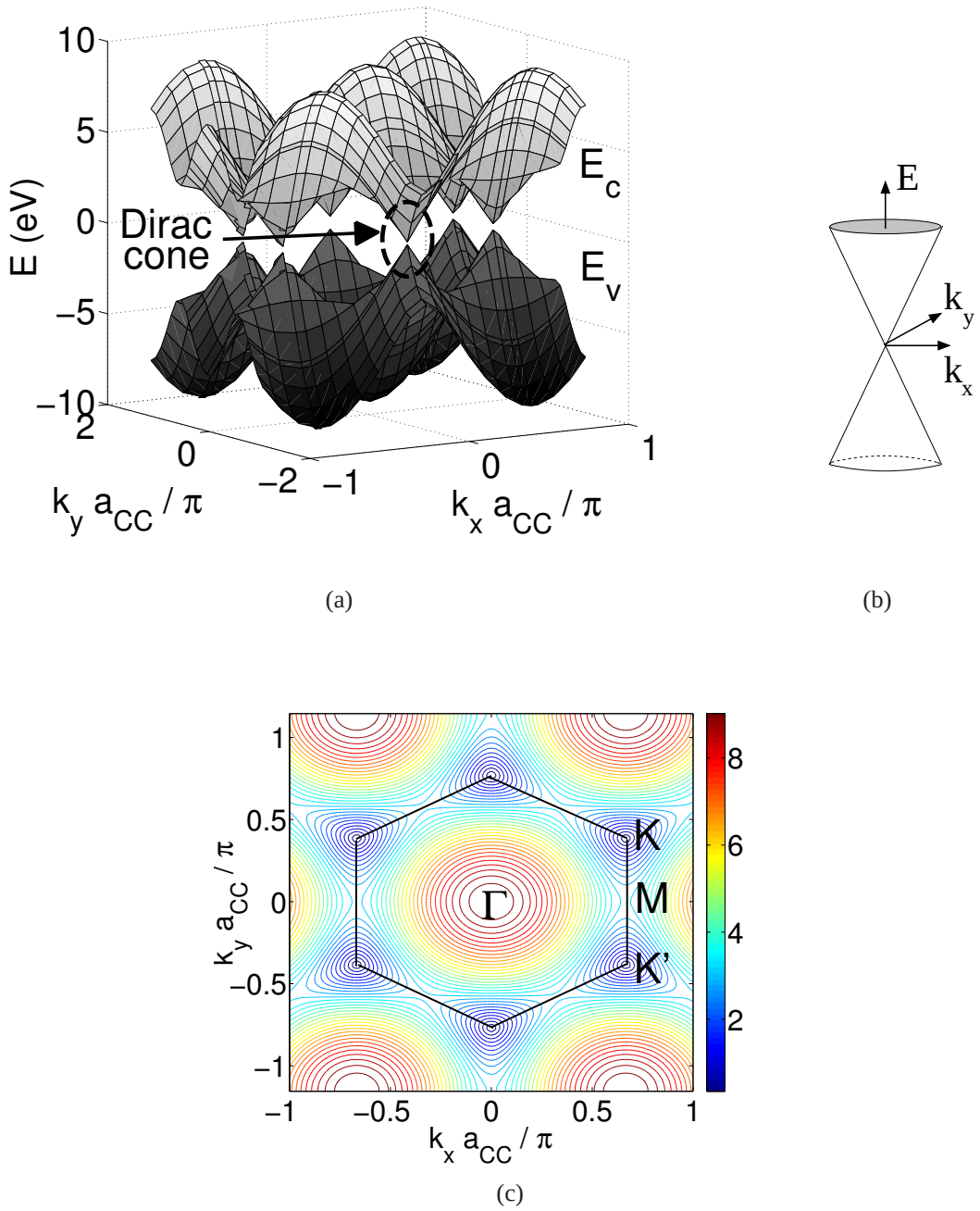

Figure 3.2: (a) 3D plot of the energy states of π^*-π valence and conduction bands, (b) Dirac cone of the graphene showing the linear dispersion relation near the Dirac points, i.e., K and $K^{'}$ in the contour plot, and (c) the contour plot of the valence band showing the reciprocal lattice points [184].

or epitaxial graphene layers are used in back gate or dual top/back gate configuration as shown in Fig. 3.3(a) and (b), respectively.

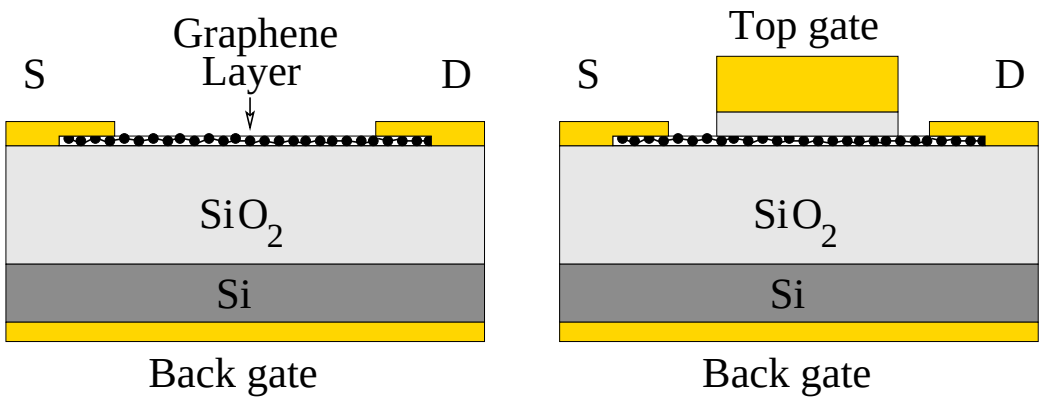

(a) (b)

Figure 3.3: Graphene field effect transistor with (a) back-gated, and (b) dual top/back gated device geometry where the graphene layer is formed of either large area graphene or graphene nanoribbon [164].

The Fermi level of the graphene can be modulated by back-gate voltage and ambipolar FET behavior is observed on a SiO_2 substrate such that the device shows the minimum conductivity for some gate voltage V_D called the Dirac voltage, it shows p-type behavior for $V_g < V_D$ and n-type behavior for $V_g > V_D$ [54]. The large area graphene FETs have on-off ratios in the range 2-20 due to zero band-gap preventing them to be used in logic applications but with significant properties for radio frequency applications. Besides that, the devices with graphene nanoribbons of width less than 5 nm which are band-gap materials show high on-off ratios on the range $\approx 10^6$.

One atomic layer thickness as a transistor device is a significantly attractive feature such that shorter channel lengths and higher speeds become possible preventing the performance restricting short channel effects [164]. In [105], a graphene FET device with cut-off frequency of 100 GHz exceeding Si metal-oxide semiconductor FET of the same gate length (53 GHz) shows significant switching behavior and channel mobility larger than 2×10^4 cm^2 V^{-1}s^{-1}.

The electron mobility at low temperature and carrier densities below $n < 5 \times 10^9$ cm^{-2}

is shown to reach 2×10^5 cm^2 V^{-1}s^{-1} which cannot be obtained with conventional semiconductors. The perfect crystalline structure and frozen high-energy optical phonons (≈ 200 meV) at room temperature lead to ultra-high mobilities as high as 2×10^4 cm^2 V^{-1}s^{-1} in the high carrier density regime. The mobility is observed to be independent of the carrier density and temperature such that temperature independence shows that defect scattering is the dominant limiting factor. Another interesting observation is the minimum conductance of graphene such that it has a minimum quantum unit of conductance even with zero charge carrier density, i.e., $4\,e^2\,/\,\pi\,h$ [137, 178].

These properties and near-ballistic transport at room temperature make the graphene a favorable building block for the future next generation electronic and optoelectronic components. In photodetector applications, graphene is usually used in a transistor configuration with source and drain contacts, and modulating gate voltages. Therefore, in order to measure the high frequency performance of the photodetector, it is necessary to model the resistance, capacitance and carrier velocity of the graphene in a transistor photodetector configuration which is described next.

3.1.1.1 Resistance Model

The total resistance of a graphene flake in a transistor FET configuration can be described by the following,

$$R_{tot} \,=\, R_{bulk} + 2\,R_c = \,\rho_{sh}\,L\,/W \,+\, 2\,\rho_c\,/(L_c\,W) \tag{45}$$

where ρ_{sh} and ρ_{shc} denote the sheet resistances of graphene channel and the region under the contacts, respectively, L_c is the contact length, L and W are graphene channel length and width, respectively [181].

The contact resistance experiments show that the resistance changes with gate bias [181, 189]. In Fig. 3.4(a), the contact resistance vs. gate voltage is seen for the graphene FET with length $1\,\mu$m and width $2\,\mu$m at room temperature where V_D is the *Dirac voltage* at which the carrier density is the lowest, resistance is the maximum and the conductance is

the minimum. The exfoliated single-layer graphene flakes are connected to palladium/gold (25 nm) contacts where the flake is put on 90 nm silicon oxide (SiO_2). When the channel is p-doped with a large negative gate voltage, the contact resistance minimum is about $185 \pm 20\,\Omega\,\mu$m which is used in our calculations.

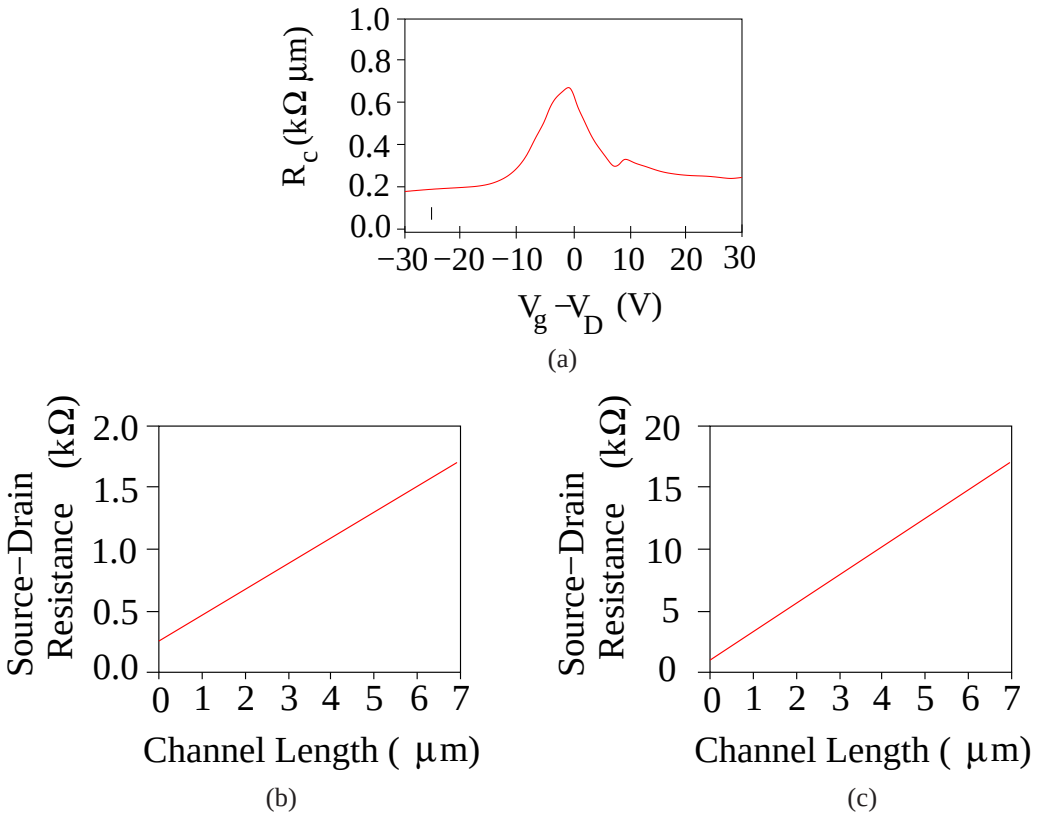

Figure 3.4: (a) The contact resistance measurements performed for $1\,\mu$m long and $2\,mu$m wide graphene FET with palladium/gold (25 nm) contacts, total drain-source resistance for (b) $V_g = -10$ V and (c) $V_g = 23$ V [189].

The contact conductance is theoretically shown to be $(4\,q^2\,/\,h)\,T\,M$ by using Landauer's approach where T is the carrier transmission probability and M is the number of conduction modes of graphene [37, 189]. For an ideal metal-graphene junction resistance, the theoretical expression gives $\approx 40\,\Omega\,\mu$m with $T = 1$ [189]. Therefore, contact resistance can be decreased 2 or 3 times by using better techniques approaching the ideal contact regime.

The contact resistance decreases if one of the following is performed; the quality of

graphene is improved with higher mobility, the morphology of the metal is improved leading to smaller metal-graphene coupling length, the metals which result in higher metal-induced doping concentration in the graphene under the metal are chosen, the graphene under the metal is doped leading to more conduction modes in the graphene under the metal and oxide thickness is reduced in order to minimize the inter-facial potential width [189].

On the other hand, the graphene sheet resistance ρ_{sh} can be extracted approximately from the measurement results in Fig. 3.4(b) and (c) [189]. It is observed that the resistance is almost uniform for different gate voltages and $\rho_{sh} \approx 400\,\Omega\,/$ sq. Although, different results are also available in literature about graphene sheet resistance, the experimental procedure in [189] is directly related to graphene FET for various gate bias and taken as the reference point. For example, in [157], epitaxial graphene grown on SiC(0001) is observed to have $\rho_{sh} > 1000\,\Omega\,/$ sq and $\rho_{sh} \leq 200\,\Omega\,/$ sq upon hydrogenation. In [94], $\rho_{sh} \leq 500\,\Omega\,/$ sq is found by using four probe method.

3.1.1.2 Carrier Velocity Model

The maximum saturation velocity of the carriers in a graphene FET photodetector configuration is the Fermi velocity, i.e., $v_F \approx 10^6$ m/s. As the number of carriers and Fermi level of the graphene layer change, the carrier velocity is observed to change in various experimental and theoretical studies [118, 154]. The carrier density is tuned continuously between electrons and holes with concentrations reaching to $n = \pm 10^{13}$ cm^{-2} by changing the gate voltage. The experiments on the conductivity of graphene on a substrate show that $\sigma = \mu\, q\, n$ where μ is the low-field mobility. The carriers are driven by electric fields with their velocity increasing linearly for low-fields. As the electric field increases, the velocity of the carriers saturate due to increased inelastic scattering by optical phonons of graphene and coupling with the substrate [118, 154]. In [118], the saturation carrier velocity, i.e., $v_c = v_{sat}$, is given as the following,

$$v_{sat} = v_F \frac{\hbar\,\omega_P}{E_F} = \frac{\omega_P}{k_F} = \frac{\omega_P}{\sqrt{\pi\, n}} \tag{46}$$

where $\hbar\omega_P$ is the phonon energy, e.g., 55 meV surface phonon energy of SiO_2, n is the carrier density, E_F is the Fermi energy modulated by the gate voltage and $k_F = \sqrt{\pi\, n}$ is the Fermi wave vector. As the Fermi energy shifts away from zero and the carrier charge density increases, the saturation velocity decreases. In [118], the minimum sheet carrier density is shown to be around $n_0 = \pm 5 \times 10^{11}$ cm^{-2} and the saturation velocity for low carrier density of n_0 and high carrier density of $n = \pm 10^{13}$ cm^{-2} is shown to be 5.5×10^5 m/s and 0.63×10^5 m/s, respectively. In [188], the saturation velocity at the built-in potential barrier of the metal and positive gate modulated graphene (p-n junction) is assumed to be the low carrier saturation velocity. However, in various gate modulations, e.g., negative gate modulation leading to p-p+ junction, there could be higher carrier density and lower saturation velocity. On the other hand, in a more recent study of [143], v_{sat} of 4-8×10^5 m/s calculated at room temperature larger than reported experimental values due to the self-heating effect where the velocity depending weakly on carrier density and the substrate. Therefore, more experimental and theoretical results are needed to fully characterize the saturation velocity in photodetector transistor applications. As a result, for practical best performance and optimized photodetectors, the low carrier density saturation velocity of 5.5×10^5 m/s in [118, 188] is applicable to be used.

3.1.1.3 Capacitance Model

The cut-off frequency performance in high frequency circuits are determined by RC time constants and transit time limited bandwidths. RC time constant is determined by the capacitive elements of circuit as discussed in Section-2.4. The total capacitance is found by adding the series capacitances of quantum capacitance C_Q and electrostatic capacitance C_{ES} of the oxide between graphene and the gate as shown in Fig. 3.5.

The quantum capacitance occurs due to quantized energy levels having a finite number of states in order to put more free carriers in the system [22, 184]. In a device, the quantum capacitance is generally in series with the geometric electrostatic capacitance and not

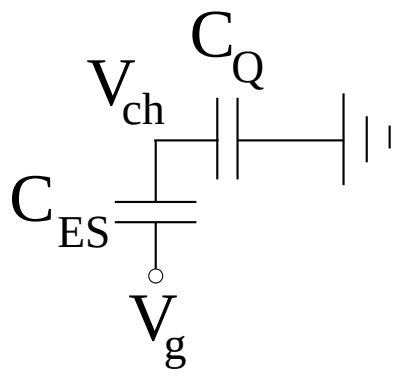

Figure 3.5: The equivalent capacitance modeling of back-gated single layer graphene transistor [193].

accessible in bulk 3D metallic conductors due to its significantly large values. C_Q reaches to infinity values when density-of-states (DOS) is very large or the energy level separation between states is infinitesimally small. In bulk conductors, the number of mobile electrons are significantly large with excitation by a very small amount of energy leading to vanishing quantum capacitance. In nanoscale dimensions, the number of electrons is getting smaller where they require larger excitation energies leading to smaller quantum capacitances. Quantum capacitance exists in low DOS systems including 1D systems.

The quantum capacitance is found by $C_Q = -q\,\partial q_c \,/\, \partial\mu$ where it is ratio of the change in charge density q_c to change in surface potential μ. For devices having electron-hole symmetry about 0 eV, it can be found by the following [38, 184],

$$C_Q = q^2 \int_{-\infty}^{\infty} g(E)\, F_T(E,\, \mu)\mathrm{d}E \tag{47}$$

where $g(E)$ is the density of states, $F_T = \partial F \,/\, \partial\mu = (1 \,/\, 4\,\kappa_B\, T)\,\mathrm{sech}^2\big(\,(E-\mu)\,/\,2\,\kappa_B\, T\big)$ is the thermal broadening function, $F(.)$ is the Fermi-Dirac distribution function.

The quantum capacitance of the graphene layer is found by using (47) as the following,

$$C_Q = \int_{-\infty}^{0} -E\,\mathrm{sech}^2\left(\frac{E - V_{ch}}{2\,\kappa_B\, T}\right)\mathrm{d}E + \int_{0}^{\infty} E\,\mathrm{sech}^2\left(\frac{E - V_{ch}}{2\,\kappa_B\, T}\right)\mathrm{d}E \tag{48}$$

where $g(E) = 2\,|E| \,/\, (\pi\,\hbar\, v_F)$ and $\mu = V_{ch} = E_F \,/\, q$ is the chemical potential which can be modulated by using the gate voltage. For $V_{ch} \gg \kappa_B\, T$, C_Q is expressed as the

following [48, 191],

$$C_Q \approx \frac{2\,E_F\,q^2}{\pi\,\hbar^2\,v_F^2} \tag{49}$$

On the other hand, for zero chemical potential, i.e., $E_F = 0$, it can be expressed as the following,

$$C_Q \approx \frac{2\,q^2\,\kappa_B\,T\ln(4)}{\pi\,\hbar^2\,v_F^2} \approx 8\,\text{fF}/\mu\text{m}^2 \tag{50}$$

such that the graphene layer has the minimum intrinsic capacitance of 8 fF/μm^2 at the room temperature increasing with back-gate modulation according to (49).

The electrostatic oxide capacitance, i.e., C_{ES}, is given by $= \epsilon_r\epsilon_0\,/\,t_{ox}$ where ϵ_r is the relative permittivity of the oxide [48]. For $\epsilon_r = 3.9$ of SiO_2, conventional oxide thickness of $t_{ox} = 300$ nm results in $C_{ES} = 0.115$ fF/μm^2. It can be observed that even the minimum intrinsic graphene quantum resistance is larger than the electrostatic capacitance leading to negligible quantum capacitance.

3.1.2 Optical Properties

Graphene's strong and approximately constant optical absorption over the broadband spectrum of far infrared to near ultra-violet makes it a promising candidate in future optical communications architectures [6]. The linear energy dispersion of the Dirac fermions makes the broadband applications possible. The light transmittance, i.e., T, of free-standing single layer graphene is theoretically shown to be equal to the following by applying the Fresnel equations,

$$T = \left(1 + \frac{\pi\,\alpha}{2}\right)^{-2} \tag{51}$$

where $\alpha = e^2\,/\,(4\,\pi\,\epsilon_0\,\hbar\,c) = 1\,/\,137$ is the fine structure constant [20]. Therefore, the absorption of graphene layers is proportional to the number of layers where each absorbs $\%\,2.3$ of the incoming white light over the visible spectrum [6, 128]. This can be compared with traditional semiconductor, e.g., $\%\,1$ absorption of light for a 10 nm thick GaAs quantum well [14]. Furthermore, it is observed that the absorption of single layer graphene can be modulated due to Pauli blocking by an external gate field which tunes the Fermi

level [100, 136]. The low density of states in the vicinity of the Dirac point leads to easy shift of the Fermi level making Pauli blocking possible in the visible range of the spectrum [136]. Moreover, the graphene can be saturated with strong optical excitation which is used in the mode locking of fiber lasers by using graphene as the saturable absorber [14]. The saturation intensity of graphene is shown to be changing between $\approx 7 \times 10^3$-6×10^6 W/mm^2 for optical frequencies from near-IR to visible spectral regions [180, 197]. These power levels are very high for practical applications and the effect of saturation intensity is not considered in our analysis in this thesis. Optical tuning, large absorption, easiness of manufacturing and engineering, and combination with tremendous electronic properties make the graphene candidate for future photonic and optoelectronic devices. Next, the band-gap engineering of graphene is introduced such that its usability is widened.

3.1.2.1 Graphene Bandgap Engineering

The zero band gap limits the applications of graphene in field-effect transistors requiring a high current on/off ratio and more efficient photodetectors in terms of optical absorption. The zero-band gap of the graphene can be changed by various forms of band-gap engineering, i.e., gated bi-layer graphene field effect transistors, patterning graphene into narrow ribbons (graphene nanoribbons), applying uni-axial strain on single layer graphene, hydrogenation and molecule adsorption, introducing a finite density of Stone-Wales defects and on top of boron nitride substrates [17, 46, 59, 67, 108, 132, 142]. Two important band-gap engineering methods, i.e., bi-layer graphene and graphene nanoribbons (GNRs), show band-gaps as much as ≈ 250 meV in bi-layer graphene, ≈ 200 meV and ≈ 0.5 eV in nanoribbons of width 15 nm and 4 nm, respectively [67, 153, 201]. Next, the mentioned graphene derivatives, i.e., bi-layer and nanoribbon graphenes, are introduced.

3.1.3 Graphene Family

The single-layer graphene forms the basis of more engineered nanostructures which are advantageous in terms of electronic and optical properties, e.g., opening a tunable band-gap

in bi-layer and nanoribbons, absorbing more light in multi-layer structures. In this section, two important engineered structures based on single layer graphene are introduced, i.e., bi-layer graphene (BLG) and graphene nano-ribbon.

3.1.3.1 Bi-layer graphene

Bi-layer graphenes can be formed by using the natural stacking fashion of graphite, i.e., Bernal stacking named after the British scientist John Desmond Bernal determining the structure of graphite in 1924, as shown in Fig. 3.6(a) where one of the basis atoms is placed on top of the other basis atom of the bottom layer, and the other basis atom of the top layer is placed on the center of the hexagon of the bottom layer forming a four-atom basis structure [136]. This is A-B Bernal stacking where bilayer graphene is generally found. Bernal stacked bi-layer graphene has two valence and two conduction bands as shown in Fig. 3.6(b). It has zero-band gap with hyperbolic bands not linear like single-layer graphene where the distance between two valence or conductions bands is $\gamma \approx 0.4$ eV [51]. The atomic structure of Bernal-stacked bilayer graphene and energy dispersion diagram with the band-gap opening by induced electric field of the gate voltage are shown in Fig. 3.6(a) and (b), respectively.

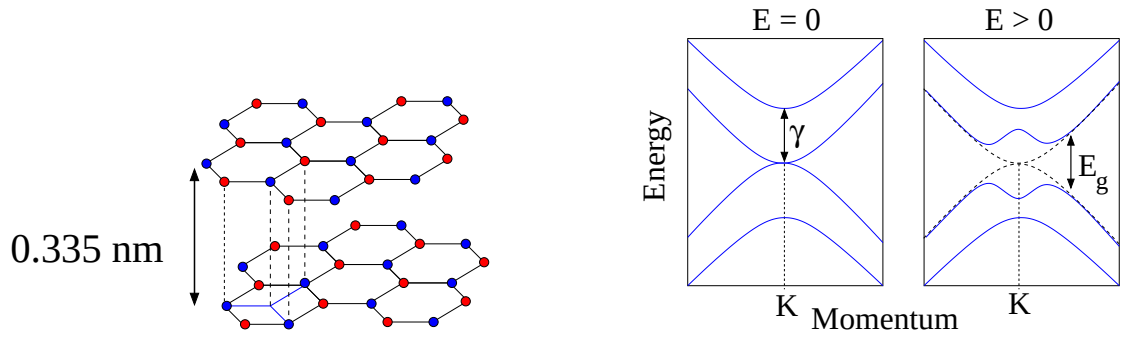

Figure 3.6: (a) The atomic crystal structure, and (b) energy dispersion diagram of AB Bernal-stacked bilayer graphene [54, 61, 136].

Bilayer graphene does not have the same properties as the single-layer graphene although it consists of two single-layer graphenes. By either applying a gate voltage or chemically doping of one side lifts the chiral symmetry in bi-layer and opens a tunable band-gap in the spectrum. Therefore, the tunability property of bi-layer graphene opens a new prospect of future optoelectronics components.

3.1.3.2 Graphene Nanoribbon

Graphene nanoribbons are strips of graphene with armchair, zigzag or chiral edges as shown in Fig. 3.7 where the cutting of the graphene layer is dependent on chiral angle θ which is between 0^o called *zigzag* and 30^o called *armchair*. The chiral angle depends on the index (n, m) with the following relation,

$$\theta = \tan^{-1}\left(\sqrt{3}\, m/(2n+m)\right) \tag{52}$$

where for example with $(n,\ m) = (3,\ 1)$ it equals to 13.8979^o.

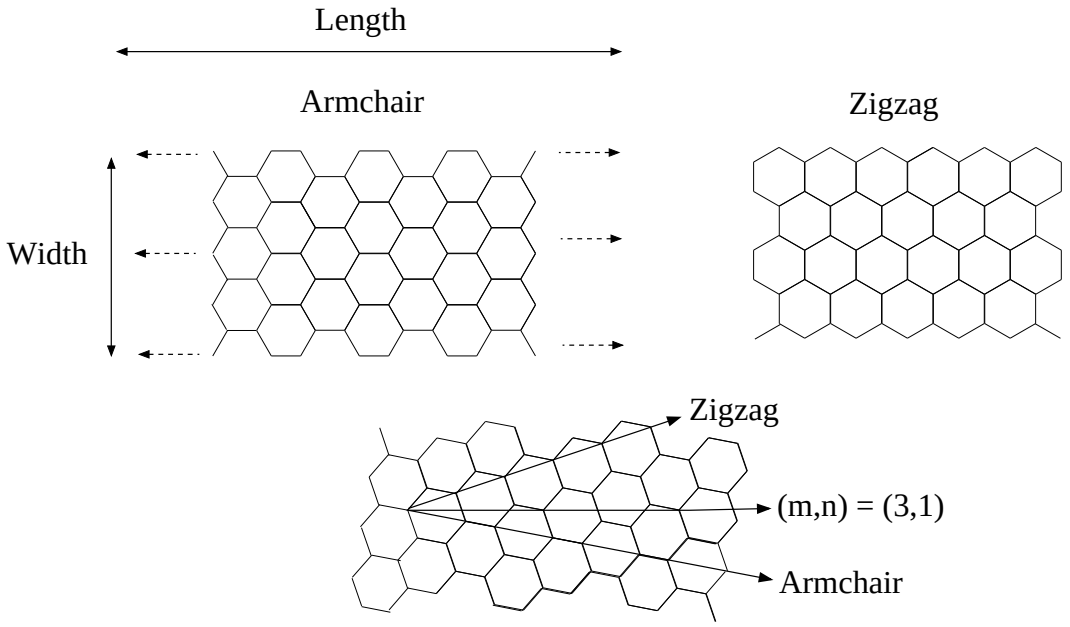

Figure 3.7: The crystal geometry of graphene nanoribbon types [174].

The electronic properties largely depend on the edge structures, i.e., the chiral angle of the nanoribbon. The carriers confined to a quasi-one-dimensional system lead to energy

band-gap giving another method to produce band-gap in graphene [67]. It is observed that the band-gap scales inversely proportional to the GNR width as the following

$$E_g = \frac{\alpha}{W - W^*} \tag{53}$$

where $\alpha = 0.2$ eV and $W^* = 16$ nm are obtained in [67]. In recent studies, it is stressed out that as much as 0.5 eV band-gap opening is possible with 4 nm width zigzag GNR [153]. The ab inito calculations reveal that chiral GNRs have semiconducting properties due to edge effects with increasing bandgap with decreasing GNR width as shown in (53) [51].

GNRs can be used in field effect transistors as either n-type or p-type with a modulating top-gate [175]. One of the disadvantages of patterning GNRs is the reduced mobility with increased band-gap, e.g., $< \ 200\,\text{cm}^2\,\text{V}^{-1}\text{s}^{-1}$ for 1-10 nm wide GNRs and $\approx 1500\,\text{cm}^2\,\text{V}^{-1}\text{s}^{-1}$ for 14 nm wide GNR [164]. GNRs with simple and easily producible 2D structure, high electrical and thermal conductivity and tunable band-gap make GNRs very important building blocks in future nanoscale optical communication architectures.

3.2 Introduction to Graphene Photodetectors

Graphene photodetectors forming transistors, p-n junctions or p-i-n detectors are experimentally and theoretically analyzed in detail in various works showing remarkable performances [20, 89, 95, 124, 125, 140, 141, 161, 187, 188, 194]. Graphene based photodetectors absorb light over a broad wavelength range from UV to THz and it can be an ultrafast wide-spectrum photodetector device due to its huge mobility. Graphene photodetectors have generally metal-graphene-metal device geometries working based on photothermoelectric effect [194], p-n junctions sweeping the photogenerated carriers by built-in electric field [187, 188], which is the main scope of the thesis, phototransistor opto-electric gains [159, 160], and p-i-n geometries with multiple graphene layers [161]. These devices are either electrostatically doped by top/back gates or chemically doped by molecular dopants [161, 187, 188].

3.2.1 Graphene Photo-thermoelectric Photodetectors

In [95, 194], photocurrent response in junctions of metal-graphene-metal devices is analyzed considering photothermoelectric contributions without analyzing fundamental performance characteristics. Temperature gradient can be generated by incident light across an interface between materials with different thermoelectric power and the resulting photocurrent generation is due to photothermoelectric effect (PTE) [194]. In [194], zero-bandgap graphene heterostructures are formed with single-bilayer graphene interface as shown in Fig. 3.8(a).

Photocurrent at graphene interface changes sign as the gate voltage is swept from negative to positive. Photocurrent generated by PTE is modeled as

$$I_{ph} = \frac{(S_2 - S_1)\,\Delta T}{R} \tag{54}$$

where $S_{1,2}$ denotes thermoelectric powers of single-layer and bi-layer graphene layers, R and ΔT denote the resistance and temperature difference between them, respectively. It is observed that the photocurrent profile at the interface exactly follows the thermoelectric power profile for varying gate voltages as shown in Fig. 3.8(b) and (c). PTE is shown to be the dominating mechanism of the current generation compared with the built-in electric field at the interface. Therefore, future graphene photodetector devices can be formed by using thermo-electric effect in more efficient ways.

3.2.2 Graphene Junction Photodetectors

Single-layer, bi-layer or multi-layer metal-graphene-metal devices are analyzed theoretically and experimentally in [89, 124, 125, 140, 141, 161, 187, 188] emphasizing the collection of carriers by Schottky barriers at metal-graphene interfaces or applied external bias. These devices are denoted by *metal-graphene-metal photodetectors* in this thesis. Two common experimentally tested graphene photodetectors, i.e., symmetric and asymmetric metal types, and theoretically analyzed p-i-n structures obtained with multiple graphene layers are presented by comparing their properties.

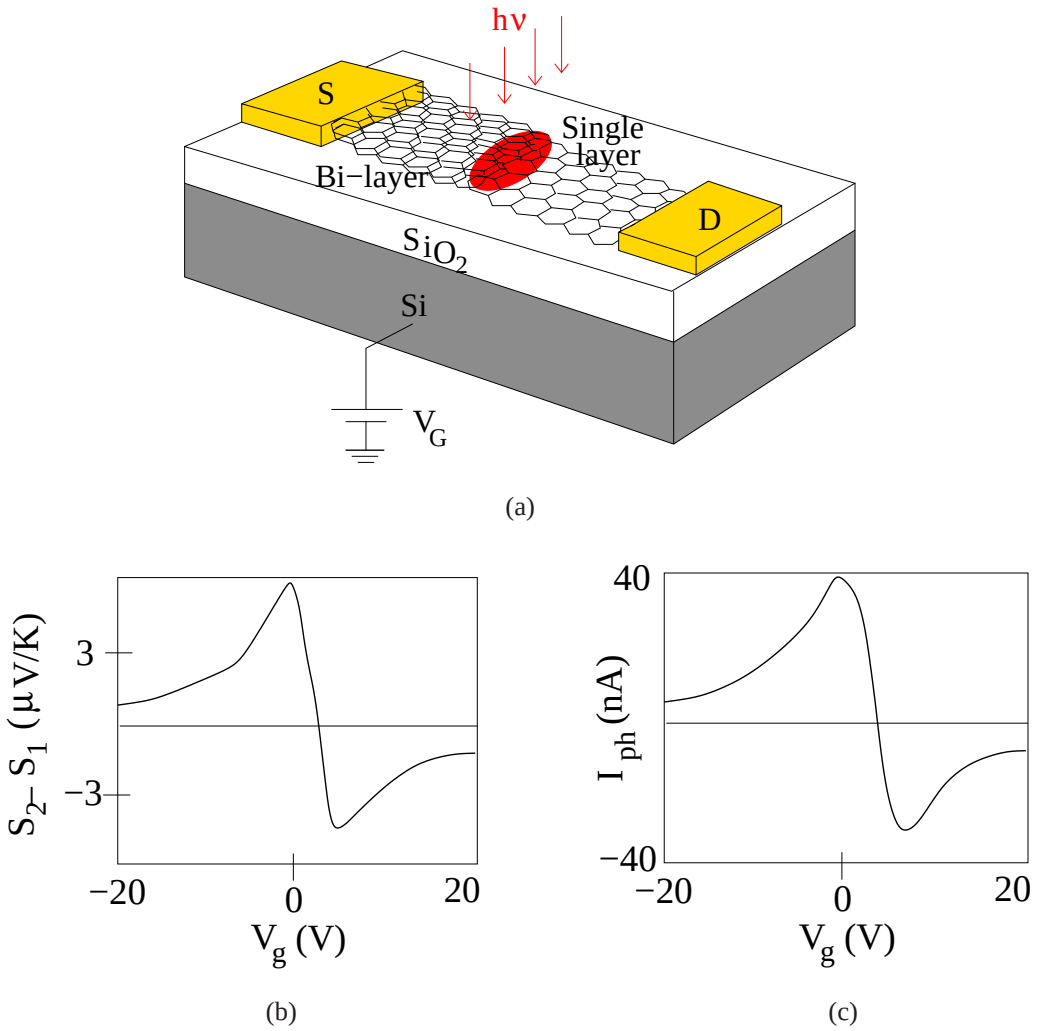

Figure 3.8: (a) Device model of graphene photothermoelectric photodetector formed by single/bilayer heterojunction interface [194], (b) thermoelectric power profile, and (c) photocurrent profile for varying gate voltages.

3.2.2.1 Symmetric Metals

In [188], an ultrafast metal-graphene-metal photodetector is introduced for single-layer and multi-layer graphene prepared by mechanical exfoliation of graphite and graphitic flakes deposited on Si surface covered with a 300-nm-thick SiO_2 with symmetric S-D contact electrodes (Ti/Pd/Au) as shown in Fig. 3.9(a).

Graphene channels have $L = 1\text{-}2\,\mu$m length and $W = 1\text{-}2.5\,\mu$m width. The zero bias short circuit operation energy-band diagram and I-V characteristics of the ultrafast detector

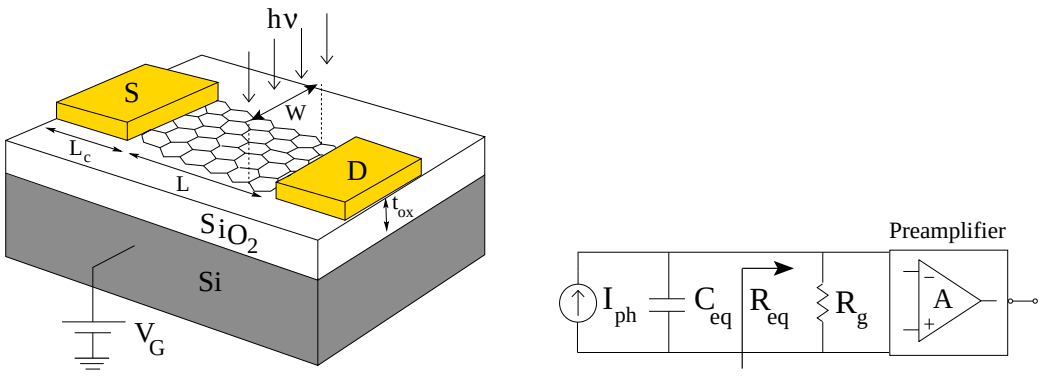

Figure 3.9: (a) Device model of metal-graphene-metal photodetector with metallic contacts on source/drain and a modulating back gate [124,188], (b) equivalent circuit for metal-graphene-metal photodetectors [124, 188].

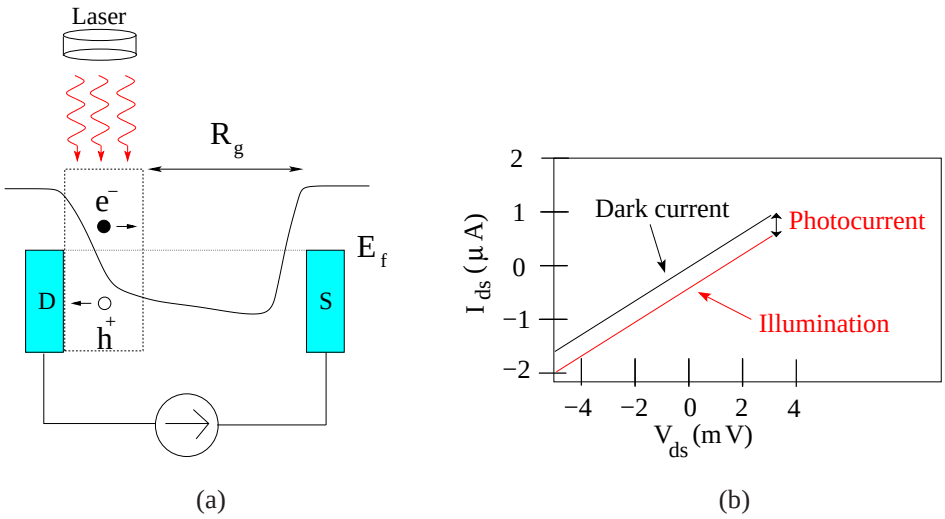

Figure 3.10: (a) Short circuit energy band diagram of ultrafast symmetric metal-graphene-metal photodetector, and (b) I-V characteristics [188].

are shown in Fig. 3.10(a) and (b), respectively.

The device is operated near the short-circuit or zero-bias conditions in order to obtain zero dark current as shown in Fig. 3.10(b) such that the dark current curve passes through the origin. Furthermore, the resistance of the graphene channel along the way to the contact is assumed to be much larger than the load resistance, e.g., $50\,\Omega$, at zero-bias and the device is operated under short circuit conditions for high frequency applications. The equivalent

circuit of the device is given in Fig. 3.9(b) where a photoconductive mode of operation is assumed which is the main circuit model for single-layer graphene wireless optical receivers analyzed in this thesis. In Schottky barrier metal-semiconductor-metal photodetectors, a high reverse bias overcoming the flat-band condition is necessary for high-bandwidth operation, however, the zero gap nature in single layer graphene permits the unobstructed transmission of carriers through the potential barriers shown in Fig. 3.10(a).

It is demonstrated that ultra-high bandwidth and ultrafast photodetectors using single and few layer graphenes have bandwidths larger than 500 GHz light detection, ultra-wide range optical spectrum, zero dark current, good internal quantum efficiency ($\%$ 6-16) and fabrication advantages.

On the other hand, in [125] and [187], photocurrent is observed in gate doped *p-n* and *p-n-p* junctions with device geometries similar to ultrafast photodetector. In these works, photocurrent is observed near metal-graphene interfaces and p-n junctions reaching ≈ 500 nm depth from the metal to graphene. S-D contacts of the same metal results in a symmetric energy band diagram. Local absorption induce spatially changing photocurrent whereas shining the whole graphene channel leads to zero photocurrent due to reverse currents canceling each other at each side of graphene.

The band diagram and the photocurrent profile along the graphene layer are shown in Fig. 3.11 where optical excitation from Ar-ion laser illuminates the graphene junctions locally at the wavelength 514.5 nm with upper spatial resolution of 150 nm in [125].

The gate bias (V_g) tunes the device near graphene-metal contacts as p-$p+$ or p-n junction as shown in Fig. 3.11(c) and (d). The photocurrent is proportional to the potential gradient at the optical line-scan excitation position. For $V_g < 0$, the photoexcited electrons drift to the nearby electrode and holes to the bulk of graphene due to the formed electric field near the contact where the field is maximum at the contacts such that the photocurrent is maximum at the illumination position corresponding to the contacts as shown in Fig. 3.11(a). For $V_g > 0$, the main body of the graphene becomes n-type and the p-n-p

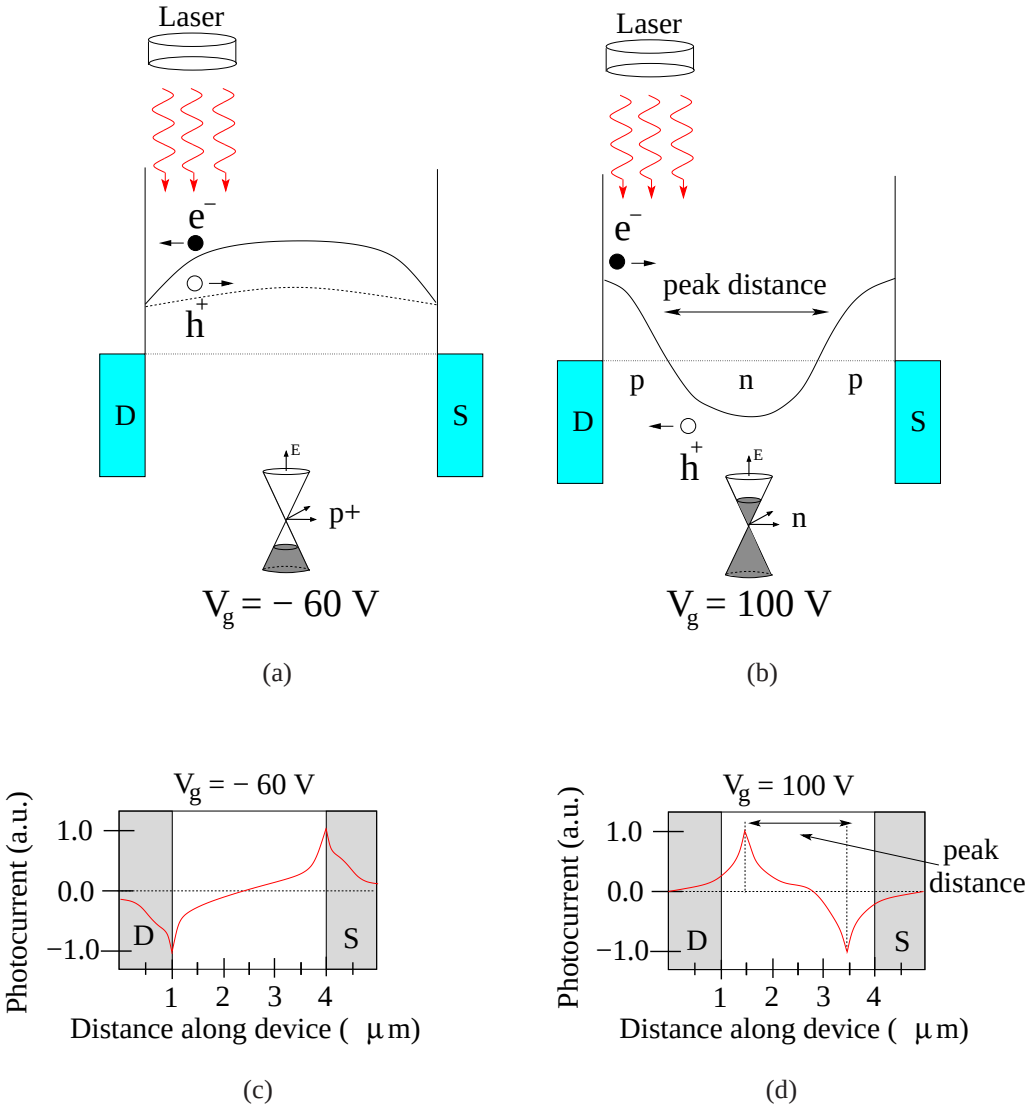

Figure 3.11: Energy band diagrams of symmetric metal-graphene-metal photodetector for (a) $V_g = -65$ V making graphene $p+$ doped, (b) $V_g = 100$ V making graphene n doped, and their photocurrent (I_{SD}) profiles with respect to the illumination line-scan position for (c) $V_g = -65$ V, and (d) $V_g = 100$ V [125].

junctions form sweeping carriers to the reverse side compared with the negative gate bias. The maximum of the electric field is inside the graphene away from the contacts which is understood from the photocurrent profile in Fig. 3.11(d). Furthermore, p-n junctions are experimented to be formed with single-multi layer graphene interfaces in [125] in order to obtain heterojunction photodetector devices. The similar device geometry and experimental works in [187] show that with $30\,\mu$W incident power, the responsivity of 0.001

A/W and external quantum efficiency of $\%\,0.2$ are achieved at the wavelength 632.8 nm such that a single layer of graphene atoms with 0.3 nm thickness shows impressive performance. Therefore, graphene is a promising ultrafast material for nanoscale optoelectronic applications with its high mobility.

3.2.2.2 Asymmetric Metals

On the other hand, metal-graphene-metal photodetectors utilizing the whole bulk graphene channel for photocurrent are formed with multiple metal fingers of different work functions, e.g., Ti/Pd, on a SiO_2/Si substrate with backgate modulation [124]. Asymmetric metals result in better electric field modulation along graphene channel and increase photocurrent. The combined effect of multiple metal fingers and the asymmetric metals brings a 15-fold increase in [124] compared with [188]. The main photocurrent generation mechanism in both symmetric and asymmetric metal graphene detectors is the electric field which can be tuned with changing gate voltages, changing metal types and multiple fingers separated to optimize the electric field [124, 188]. The device geometry, photocurrent profile vs. the line-scan position and the photocurrent vs. gate voltage for wholly illuminated device are shown in Figs. 3.12(a), (b), (c) and (d), respectively.

Total generated photocurrent of the device is calculated by summing the local contributions obtained from each line-scan as shown in Fig. 3.12(b) to find the total response as shown in Fig. 3.12(c) [124]. It is observed that 10 Gb/s optical data link at the wavelength of 1.55 μm can be achieved with error-free detection. Furthermore, the photoresponsivity of 6.1 mA/W is achieved at room temperature which is 15-fold improvement compared with the symmetric ultrafast graphene photodetector in [187].

The performance of the asymmetric device compared with the symmetric device depends on the electric field improvement, number of fingers and the absorption area which can be changed significantly with various device geometries, metal types and illuminated

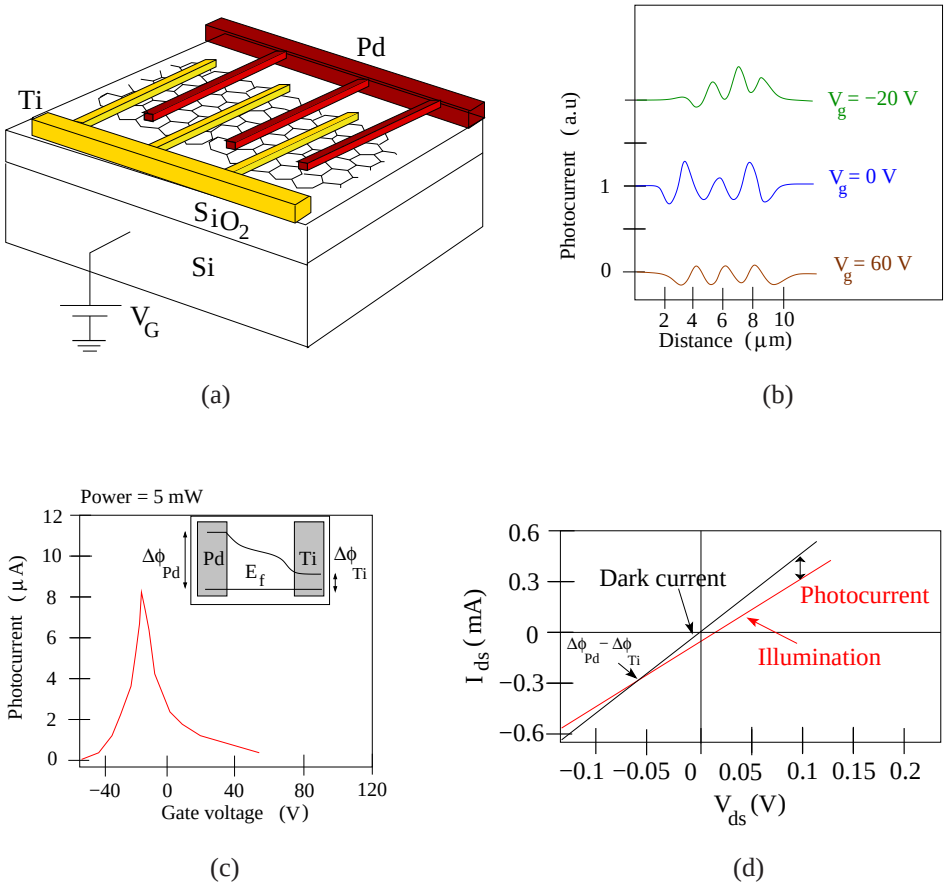

Figure 3.12: Multiple-finger asymmetric metal-graphene-metal photodetector (a) device geometry, (b) photocurrent profile, (c) photocurrent vs. gate voltage bias, the inset shows the zero-bias energy band diagram of the detector where $\Delta\phi_{Pd}$ and $\Delta\phi_{Ti}$ are the differences between the Dirac point energy and the Fermi level in metal doped graphene, and (d) I-V characteristics [124].

region. The communication theoretical comparison of the asymmetric metal-graphene-metal detector of various geometries with the symmetric photodetector is for the future work and is out of scope of the thesis. More experimental works with asymmetric devices and their detailed theoretical modeling are necessary to formulate the asymmetric metal-graphene-metal device performance on each line-scan channel. However, photocurrent analysis of any graphene photodetector, whether symmetric or asymmetric, can be performed by finding the potential profile of the device along its length, then finding electric field dependent local internal quantum efficiencies and finally summing the contributions

obtained from each local line-scan. The change in the quantum efficiency, absorption constant, graphene area and total contribution of varying number of line-scan channels for different device geometries can be easily reflected in our formulations developed in the next sections.

3.2.2.3 Multi-layer Graphene p-i-n Detector

The efficiency of single-layer devices can be increased by using stacked independent layers of single-layer graphene, i.e., multi-layer graphene (MLG) [161]. The device is formed of multiple graphene layers in a p-i-n junction device geometry as shown in Fig. 3.13(a) and (b).

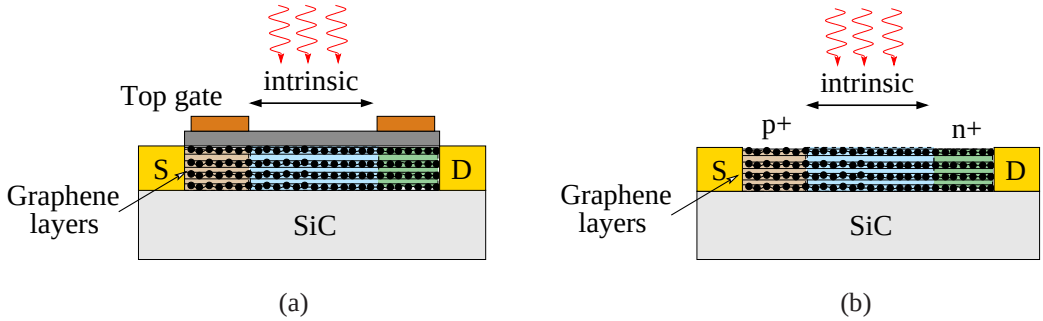

Figure 3.13: Simplified device scheme of multi-layer graphene p-i-n device either (a) electrostatically or (b) chemically doped [161].

The device has ohmic side contacts with multiple graphene layer on Silicon Carbide (SiC) substrate and the doping can be achieved either with electrostatically or chemically by using molecular dopants. If a sufficiently strong reverse bias is applied, electrons and holes generated in the intrinsic region are swept to the contacts. The multi-layer graphene absorbs light with the ratio $\alpha_{ML} \approx 1-(1-\alpha)^K$ where K is the number of layers and efficiency of light absorption in a single graphene layer is $\alpha = \%\,2.3$ of the incoming light. Therefore, the significant advantage of the device comes from the increased absorption efficiency with high number of K, i.e., layers. Furthermore, the device shows better performance compared with quantum-well (QWIP) and quantum-dot (QDIP) photodetectors having same K such that the device shows the same dark current in different spectral

ranges as different from QDIP and QWIP. Moreover, it exhibits better detectivity performance compared with narrow-gap and gapless bulk semiconductors like HgCdTe due to lower thermo-generation rate.

3.2.3 Graphene Phototransistors

Theoretical analysis of dark current detectivity of graphene bi-layer (BLG) and nanoribbon (GNR) phototransistors is achieved in [159, 160]. An array of parallel graphene nanoribbons of width d and inter-spacing $ds \ll d$ is used in a top/back gate graphene field effect transistor device geometry as shown in Fig. 3.14 [159].

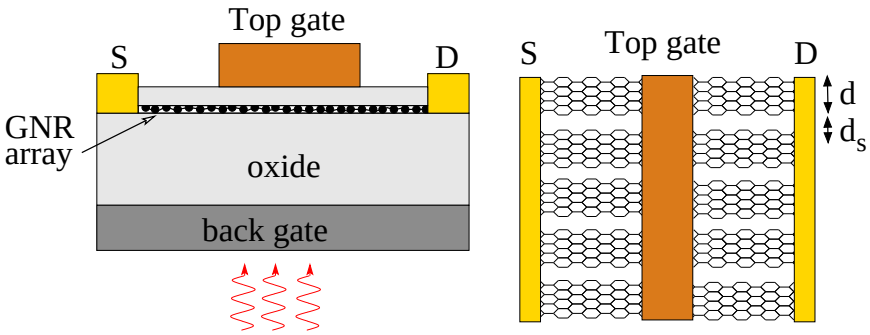

Figure 3.14: Simplified device scheme of phototransistor constructed with parallel array of graphene nanoribbons in a top/back gate field effect transistor configuration [159].

The responsivities as much as 10-20 A/W are obtained significantly exceeding intersubband quantum-well, quantum-wire, and quantum-dot photodetectors in IR and THz range of operation. Furthermore, the maximum responsivity exceeds the performances of conventional narrow gap semiconductor photodetectors, e.g., PbSnTe and CdHgTe, with a few A/W responsivities. The GNR phototransistor has high quantum efficiency due to lateral quantization at the series of band-gaps $n\,\Delta$, $n = 1, 2, 3, ...$ where $\Delta = 2\,\pi\,\hbar\,/\,d$ is the band-gap of the GNR depending on width d. Moreover, the device shows large photoelectric gain ($g \gg 1$) due to the long life time of the photogenerated holes confined in the gated section by high barriers.

On the other hand, graphene bi-layer with gate electric field tunable (gate voltage)

band-gap forms a promising phototransistor with high photoelectric gains [160]. Graphene bi-layer channel is placed over a substrate providing the formation of a two dimensional electron gas in the channel when it is biased positively with respect to the source and drain, i.e., $V_b > V_d > 0$ as shown in Fig. 3.15(a). The top gate is biased negatively such that the channel beneath it forms a depletion region.

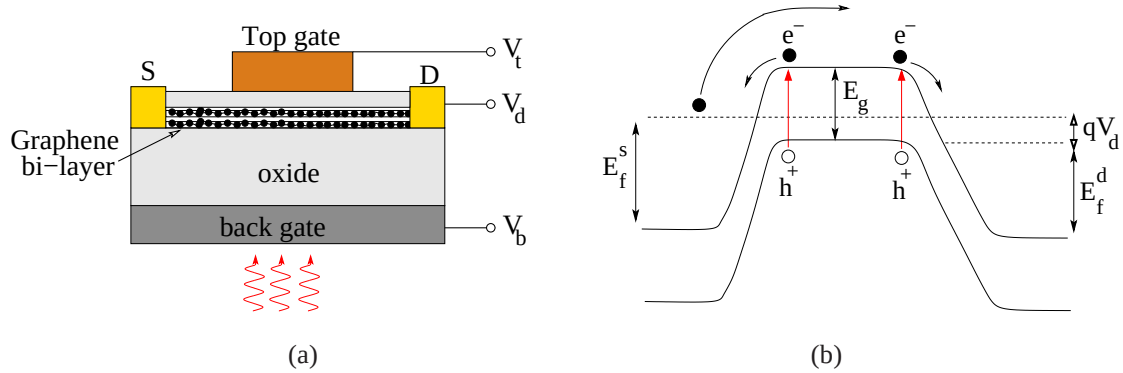

Figure 3.15: (a) Simplified device scheme of phototransistor constructed with bi-layer graphene in a top/back gate field effect transistor configuration and (b) its operating condition band-diagram [160].

The photogenerated electrons are swept to the source and drain contacts virtually in equal portions such that the overall photocurrent generated by electrons can be neglected. However, the potential barrier is formed in the depletion section for electrons passing through source to drain as shown in Fig. 3.15(b). This barrier is lowered by the photogenerated holes accumulated in the gated section such that the variation of the injected electron current is significant leading to large photoelectric gain. The mechanism of the device operation is different from the symmetric and asymmetric metal photodetector devices discussed previously which sweep the photogenerated electrons and holes by internal barriers without any gain. Furthermore, it is observed that the device responsivity and detectivity can exceed QWIP and QDIP performances at room temperatures due to high quantum efficiency and large photoelectric gain . Moreover, the advantages of BLG phototransistor are emphasized in terms of the ease of fabrication, integration with silicon readout circuits and voltage tunable band-gap compared with QWIPs, QDIPs, HgCdTe and InSb detectors.

3.3 Efficiency of Graphene Photodetectors

Single-layer graphene is only one atom thick and absorbs $\alpha = \%\,2.3$ of the incoming white light independent of the optical wavelength [6, 128]. Although the efficiency of the single-layer symmetric detectors discussed above are low, there are different methods to increase the efficiency of the graphene detectors. Symmetric detectors give zero current under the illumination of the whole device and only a small area is effective to form the photocurrent [44]. This can be solved with multiple (asymmetric) metal fingers of different work functions [124]. Furthermore, the efficiency is improved by creating a wider photo-detection with a longer light graphene interaction length with waveguides [190]. The reducing of the internal resistance is another improvement factor [188].

The low efficiency of light absorption, i.e., $\alpha = \%\,2.3$ of the incoming light, highly restricts the potential utility of the detector [44, 161, 188]. Bi-layer, tri-layer or multi-layer graphene structures absorb linearly increasing amounts of incident light, i.e., $\alpha_{ML} \approx 1-(1-\alpha)^K$ where K is the number of layers [161]. Besides that, the energy spectrum of disoriented stacks of multiple layers is the same with the single layer by preserving the capabilities of single-layer detector in multi-layer scheme too. The comparable efficiencies of multi-layer detectors are calculated in [161] compared with quantum well and quantum dot array photodetectors.

Recently, a highly efficient, i.e., 20 times improvement compared with [124, 188], light absorption is achieved by combining graphene with plasmonic nanostructures placed near the contacts creating a field concentration at the junction regions where the generated pairs are swept [44]. The plasmonic nanostructures give the capability of the selective amplification and filtering at optical resonance frequencies depending on the geometry of the nanostructures. The contact resistances decrease and the capacitance does not change too much leading to increase in the frequency response performance. More theoretical study is necessary to analyze the dependence of the photocurrent on the combined effect of the electric field profile and the plasmonic nanostructure geometry. Next, the fundamental noise

sources are computed for metal-graphene-metal devices and SNR is computed.

3.4 Single-Layer Graphene Photodetector Model

In this thesis, experimentally validated metal-graphene-metal photodetectors are used as basic nanoscale receivers. Firstly, metal-graphene-metal device geometries in literature formed with symmetric and asymmetric metals are discussed and the symmetric one is chosen as the receiver building block in this work. Secondly, symmetric metal-graphene-metal photodetectors are analyzed by using the equivalent circuit defined in literature. Then, position dependent photocurrent and noise sources are modeled leading to basic SNR expressions.

In this work, symmetric metal-graphene-metal structure with line-scan transmit power is taken as the basic receiver unit due to formation of higher resolution nanoscale spatial channels along graphene channel which is more suitable for optical nanonetwork topologies. Furthermore, asymmetric metal-graphene-metal devices in experiments [124,188] are entirely illuminated to best utilize the devices. The proposed diversity combining scheme in this work creates high resolution channels with uniform performance which are not available and desired in asymmetric metal-graphene-metal devices performing under entirely illuminated conditions. However, the analysis performed for symmetric metals in the thesis can be easily extended to include asymmetric metal cases and various device geometries by using the experimental potential profiles of asymmetric photodetectors with the respective proportional internal quantum efficiencies. The improvements coming from higher electric fields, multiple fingers or combining effect of multiple devices can be found based on the calculation procedure of local photocurrents in each line-scan.

Next, the basic equivalent circuit of symmetric metal-graphene-metal devices are discussed by using the models defined in recent literature.

3.4.1 Equivalent Circuit Model

Photodetectors are described by equivalent circuits to compute R_b and SNR [79]. Single-layer metal-graphene-metal photodetectors are modeled in [188] as shown in Fig. 3.9(b) like a photoconductor where photocurrent is parallel to the intrinsic resistance of graphene [188]. Single-layer graphenes having widths larger than 10-25 nm are assumed to have zero band-gap such that 2D graphene layer forms ohmic contacts with the metals and have linear I_{ds}-V_{ds} relationship [51, 192]. The device has zero dark current with zero bias [188].

R_g denotes the graphene resistance, R_{eq} is the equivalent resistance of preamplifier and graphene combination and I_p denotes photocurrent. The total resistance of the graphene flake, i.e., R_{tot}, is given in (45) where it is assumed that photodetectors have same L with varying W. Therefore, $R_g = R_0(L, L_c) \,/\, W$ where $R_0(L, L_c)$ is the unit resistance per width.

Device capacitance includes the series combination of quantum capacitance given in (49), i.e., $C_Q \approx 2E_F\, q^2/(\pi\hbar^2 v_F^2)$, and oxide capacitance, i.e., $C_{ox} = \epsilon_r\epsilon_0 \,/\, t_{ox}$. Furthermore, parallel pad capacitances of the contacts are important in graphene photodetector experiments [188]. C_{eq} is used to find RC-limited cut-off data rate in the next sections. Next, photocurrent is modeled by extracting from experimental photocurrent profile of symmetric metal-graphene-metal devices and using fundamental equalities of optical absorption on incident area of graphene layer.

3.4.2 Photocurrent Model

Optical communication channels convert the input power to photocurrent where generated electron-hole (e-h) pairs are separated and collected at the external circuit [64, 79]. In this thesis, IM/DD baseband channel is modeled as shown in Figs. 2.3 and 2.4 of Section-2.2 where the basic channel modeling is presented. The output current in (2) can be expressed as $I_r(t,\nu) = I_p(t,\nu) + n(t)$, where $I_r(t,\nu)$ is the receiver current at optical frequency ν, $I_p(t,\nu) = \mathcal{R}(t,\nu)\, P_i(t,\nu)$ is the signal carrying current, $\mathcal{R}(t,\nu)$ is the responsivity,

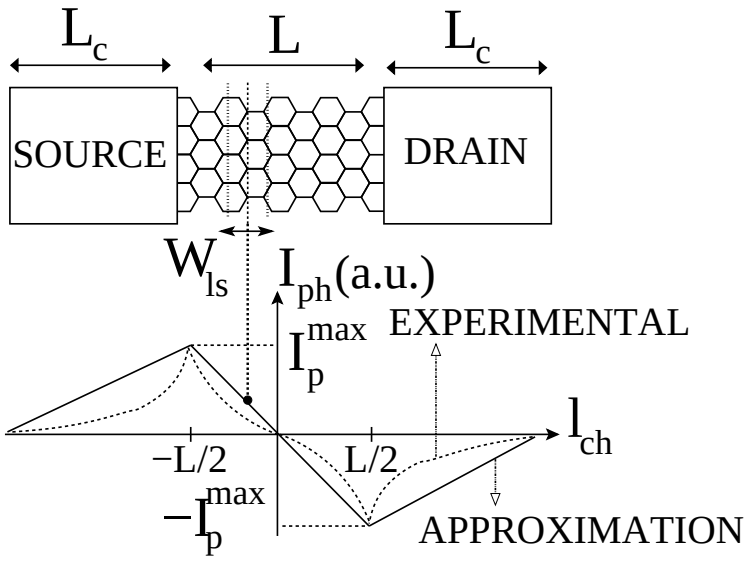

Figure 3.16: Photocurrent dependence on incident optical line-scan position for metal-graphene-metal graphene photodetector with symmetric metal contacts for large negative V_G [125, 187].

$P_i(t,\nu)$ is incident power and $n(t)$ is the independent white Gaussian noise [64, 79]. In order to compute BER, power and spatial position dependent photocurrent is modeled with position dependent internal quantum efficiency by extracting from the experimental photocurrent profile of symmetric metal-graphene-metal devices [125,187] and using universal absorption constant of graphene [6, 128].

As shown in [187] and similar to the observed photocurrent profile previously discussed for symmetric metals shown in Fig. 3.11(a), for photodetector with length $L = 1.45\,\mu$m, at large negative gate voltages, e.g., $V_G = -40V$, photocurrent shows maximum near contacts, decays to zero at middle and shows almost a linear behavior as shown in Fig. 3.16 as a result of the electric fields formed along photodetector carrying generated e-h pairs. It is approximated by linear curves without changing the overall behavior significantly based on experiments [125, 187] by concentrating on effects of line-scan position and W for constant L. Furthermore, smoother photocurrent decaying is observed in [187] which could be due to 550 nm width of line-scan incident light while in [125] 100-150 nm width leads to more nonlinear decaying. Photocurrent depends on potential gradient [125], and

in [84] induced potential is shown to decay with distance x from the metal contact as $x^{-1/2}$ and x^{-1} for undoped and doped graphenes, respectively. However, more theoretical and experimental models are needed to exactly formulate photocurrent dependence in metal-graphene-metal photodetectors and is out of scope of the thesis. Next, the efficiency metrics used in the thesis are described and potential methods to increase the efficiency of the graphene based photodetectors are discussed.

3.4.2.1 Quantum Efficiency Model

The photocurrent at line-scan position l_{ch} is approximated as shown in Fig. 3.16 as

$$I_p(\nu, l_{ch}) \;=\; -\,q\,\frac{P_a(\nu, l_{ch})}{h\,\nu}\,\eta_{In}(l_{ch})\,\text{sgn}(l_{ch}) \tag{55}$$

where $\eta_{In}(l_{ch}) \;=\; 2\,C_1\,|l_{ch}|\,/\,L$ is internal quantum efficiency at $l_{ch} \;\in\; [-0.5\,L,\,0.5\,L]$, $C_1 \;>\; 0$ is a normalization constant and sgn$(.)$ is the *sign* function. Photocurrent from contacts is due to internal photoemission and thermal injection [53, 187] and it is ignored to concentrate on intrinsic graphene properties.

Single-layer graphene being only one atom thick is shown to absorb $\alpha \;=\; \%\,2.3 \;=\; \pi\,/\,137$ of the incoming white light independent of wavelength as a result of its unique electronic structure as discussed in subsection-3.1.2 [6, 128]. It absorbs light over a wide spectral range spanning visible and infrared ranges allowing photodetectors working in a wideband spectrum. In [124], strong photocurrent response is observed at wavelengths $0.514,\,0.633,\,1.55$ and $2.4\,\mu$m emphasizing the ultrawide 0.3-$6\,\mu$m range of operation. Therefore, photocurrent for incident light of width W_{ls}, i.e., $I_{ph}(\nu, l_{ch})$, at incident power density $P(\nu)$ (W/m^2) is described by the following,

$$I_p(\nu, l_{ch}) = \varsigma(l_{ch})\,\frac{\alpha\,P(\nu)\,W_{ls}\,W}{h\,\nu} \tag{56}$$

where $\varsigma(l_{ch}) \;\equiv\; -2\,q\,C_1\,l_{ch}\,/\,L,\; l_{ch} \;\leq\; |L/2|$. Typical line-scan width, i.e., W_{ls}, ranges from 100 nm to $5\;\mu$m in graphene photodetector experiments [51, 90, 124, 125, 145, 186–188, 194]. Therefore, graphene channel is divided into $N_{ls} \;=\; L\,/\,W_{ls}$ spatial channels.

Although the efficiency of the single-layer symmetric detector is low, the developed communication theoretical method in this thesis can be applied to other device geometries where the main mechanism is the developed electric field sweeping the generated pairs to the metal contacts with a specific internal quantum efficiency and light absorption rate.

3.4.3 Noise Model and SNR

The noise types previously discussed in Section-2.6 for photodetectors in an optical wireless communication architecture are valid for graphene photodetectors too. Three dominant types of noise are *thermal* or Nyquist-Johnson noise due to interaction of electrons with vibrating ions in resistive elements, *shot noise* due to fluctuations by the discrete nature of charge carriers [70] and 1/f noise in the low frequency regime, e.g., $f < 100$ KHz, for the graphene layer [106]. Since the operating frequencies reach GHz values with ultrafast graphene photodetectors, 1/f noise is neglected [188]. Shot noise is either due to photocurrent or graphene layer. For preamplifier, sources of noise other than thermal noise are neglected [70]. In [188], short circuit and $R_L = 50\,\Omega$ load conditions are discussed whereas R_L is generalized to take any value in this thesis. Photocurrent shot noise spectral density is described by $(\sigma_s^p)^2 = 2\,q\,I_p$ [70]. Shot noise measurement of graphene coupled to an amplifier with R_L shows that noise spectral density, i.e., $\sigma^2 = (\sigma_{therm}^{eq})^2 + (\sigma_s^g)^2$, is given as

$$\sigma^2 = \frac{4\,V_{T_{eq}}}{R_L} + \frac{4\,V_T}{R_g}\left(1 - \mathcal{F} + \mathcal{F}\,\frac{q\,I\,R_g}{2\,V_T}\coth\left(\frac{q\,V}{2\,V_T}\right)\right) \tag{57}$$

where I and V are the current and voltage across the sample, respectively, T_{eq} and T are the noise temperature of the amplifier and the bath temperature of the reservoir, respectively, $\mathcal{F}$ is the bias-dependent Fano factor [36] and $V_T = \kappa\,T$. Along the thesis, it is assumed that $T_{eq} = T$. At zero dark current, only thermal components are remaining, i.e., $(\sigma_s^g)^2 + (\sigma_{therm}^{eq})^2 = 4\,\kappa\,(T_{eq}\,/\,R_L + T\,/\,R_g)$ [36]. Zero dark current for symmetric metal-graphene-metal photodetector under zero bias is a significant property for power limited nanonetworks [188].

Derived photocurrent and noise models can be used to compute SNR of IM/DD non-return-to-zero on-off keying modulation [79] such that information signal modulates the instantaneous transmitted optical power where photocurrent is proportional to the received power. For example, 10 Gb/s optical link is achieved in [124] with a pseudo-random bit sequence generator modulating the light. Therefore, SNR for the ON signal is $\gamma(\nu, l_{ch}) = I_p^2(\nu, l_{ch}) \,/\, (B\,\sigma_{tot}^2)$ where $\sigma_{tot}^2 = (\sigma_s^p)^2 + (\sigma_s^g)^2 + (\sigma_{therm}^{eq})^2$ and B is the modulating signal bandwidth. Therefore, SNR for shot and thermal noise limited regions denoted by T-R_g ($R_{eq} \approx R_g$) and T-R_L ($R_{eq} \approx R_L$), respectively, is given as

$$\gamma_s(\nu, l_{ch}) = \frac{(I_p(\nu, l_{ch}))^2}{2\,q\,|I_p(\nu, l_{ch})|\,B} = C_2^{'}\,|\varsigma(l_{ch})|\,W \tag{58}$$

$$\gamma_{T\text{-}R}(\nu, l_{ch}) = \frac{(I_p(\nu, l_{ch}))^2}{4\,\kappa\,T\,B\,/\,R} = C_k^{'}\,\varsigma^2(l_{ch})\,W^j \tag{59}$$

where $k = 3$, $j = 1$ for $R = R_g$ and $k = 4$, $j = 2$ for $R = R_L$, $C_2^{'} = C_2\,W_{ls}$, $C_3^{'} = C_3\,R_0(L, L_t)\,W_{ls}^2$, $C_4^{'} = C_4\,W_{ls}^2$, and the constants $C_2 = \alpha\,P(\nu) \,/\, (2\,q\,B\,h\,\nu)$, $C_3 = \alpha^2 P^2(\nu) \,/\, (4\,\kappa\,T\,B\,h^2\nu^2)$ and $C_4 = C_3\,R_L$ are not dependent on L, W, W_{ls} and l_{ch}. After finding width dependent SNR for single receiver, next, diversity combining methods are applied on a set of receivers with different graphene layer widths.

3.5 Diversity Combining for Multi-receiver Graphene Photodetector

Diversity combining methods improve SNR by combining multiple received signals [60], e.g., angle diversity for infrared optical communications [80]. Single-layer graphene experiments show position dependent photocurrent and significant loss if high responsivity metal-graphene interface regions do not get light. Moreover, low efficiency of the graphene photodetectors imposes a performance limitation and various methods such as multiple graphene layers, multiple metal fingers with asymmetric metals and plasmonic nanostructures are invented to better utilize the graphene photodetectors [44, 124, 161]. Therefore, to create more robust photodetectors performing independent of the illumination position

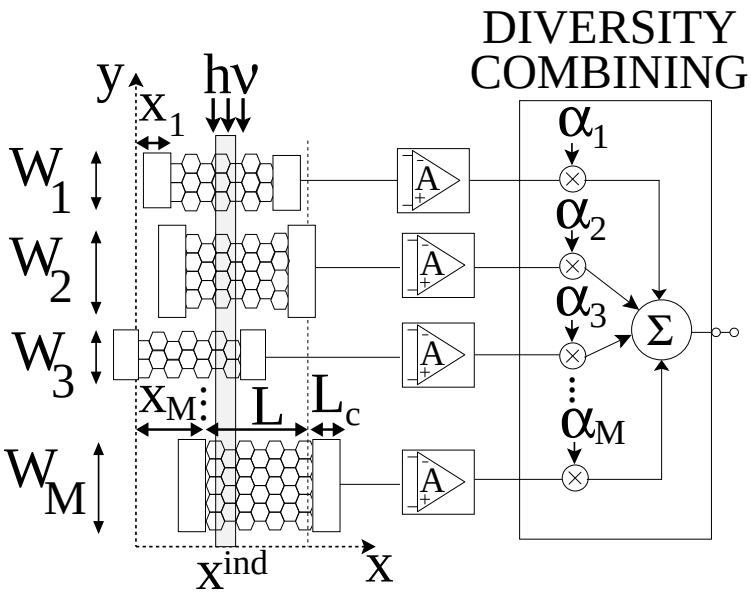

Figure 3.17: Diversity combining multi-receiver graphene photodetector formed of individual graphene photodetectors with various widths and positions where line-scan optical light is incident at x^{ind}.

of the line-scan and to increase the efficiency, a diversity placement of multiple photodetectors can be used. Besides that, photodetectors with varying widths can occur due to the nonperfect production mechanisms. Diversity methods best utilize these generated devices by increasing the efficiency and create a larger area device without compromising the speed since large area leads to lower R_b [80, 188].

A multi-receiver graphene photodetector design is shown in Fig. 3.17 where the light is incident on $0 < x^{ind} < L$ where there are M receivers with widths W_i, same length L, x-axis coordinates x_i for $i \in [1, M]$ and the same orientation with respect to a reference coordinate system. Furthermore, photocurrent contributions from contacts are ignored to concentrate on graphene properties of wide-band absorption and fast carrier velocity.

Conventional diversity combining schemes, i.e., maximal ratio and equal gain combining, are utilized in this work. Maximal ratio combining maximizes the output SNR resulting in sum of input SNRs and equal gain combining is the solution without using the knowledge of SNRs [60]. Each branch is multiplied by $\alpha_i = r_i\, e^{-j\theta_i}$ where $e^{-j\theta_i}$ is the

co-phasing component to constructively add the components. Here θ_i is $\pm\pi$ since photocurrent can take negative values. Then, output SNRs for equal gain and maximal ratio combining, i.e., γ^{EC} and γ^{MC}, respectively, are given by [60],

$$\gamma_s^{EC}(\nu, x^{ind}) = \frac{\left(|\mathbf{I}_p^T|\,\mathbf{1}\right)^2}{2\,q\,B\,|\mathbf{I}_p^T|\,\mathbf{1}} = C_2'|\boldsymbol{\varsigma}_s^T|\,\mathbf{w} \tag{60}$$

$$\gamma_{T\text{-}R}^{EC}(\nu, x^{ind}) = \frac{\left(|\mathbf{I}_p^T|\,\mathbf{1}\right)^2}{\sum_{i=1}^{M}\frac{4\,\kappa\,T\,B}{R_i}} = C_k'\frac{\left(|\boldsymbol{\varsigma}_s^T|\,\mathbf{w}\right)^2}{Y_R} \tag{61}$$

$$\gamma_s^{MC}(\nu, x^{ind}) = \gamma_s^{EC}(\nu, x^{ind}) \tag{62}$$

$$\gamma_{T\text{-}R}^{MC}(\nu, x^{ind}) = C_k'\sum_{i=1}^{M}\varsigma_s^2(x^{ind}, x_i)\,W_i^j \tag{63}$$

where $R = R_g$ or R_L, $R_i = R_{g,i}$ or R_L, j, k are defined in (59), $Y_{R_g} = \mathbf{w}^T\,\mathbf{1}$, $Y_{R_L} = M$, $\mathbf{I}_p(i) = I_p(\nu, x^{ind}, x_i)$, $\boldsymbol{\varsigma}_s(i) = \varsigma_s(x^{ind}, x_i)$, $\mathbf{w}(i) = W_i$, $i \in [1, M]$, $\mathbf{1}$ is the vector of ones and $\varsigma_s(x^{ind}, x_i) = \varsigma(x^{ind} - L/2 - x_i)$. Next, parallel line-scan topology is defined where diversity is utilized.

3.6 Parallel Line-scan Optical Nanonetworking

Line-scan transmitter-receiver networking topology is better suited for broadcast to cover the whole width of graphene channel in a rectangular planar receiver geometry and to create distinct and controlled spatial subchannels with high resolution. Therefore, line-scan topology can be used to broadcast the information among different devices. Although the physical mechanism to construct the topology is out of scope of the thesis and in future nanoscale optical networks it can be realized, in current technology it can be realized by systems similar to a confocal Raman microscope to form the uniform intensity line illumination pattern. Next, diversity combining methods are applied on single receiver by cutting the graphene to smaller width receivers with the same total area to create uniform spatial channels with improved SNR performance.

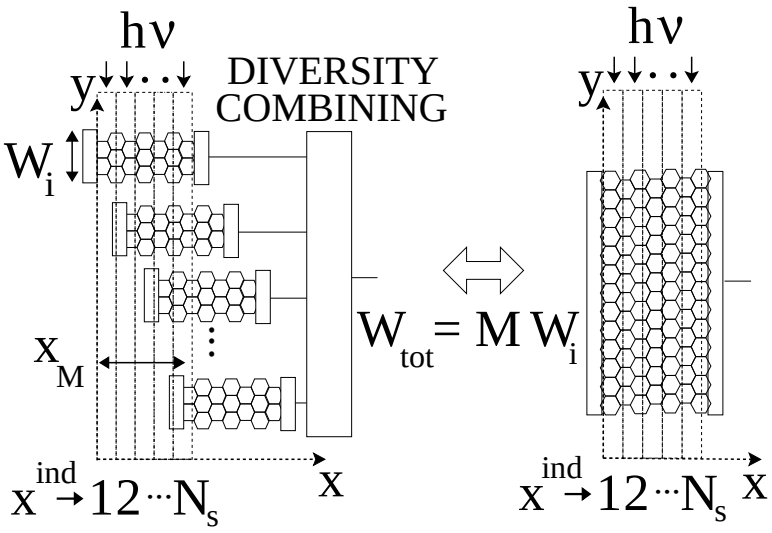

Figure 3.18: A diversity combining optimization framework for spatial parallel line-scan channels by forming smaller width graphene photodetectors with sum $W_{tot} = M\,W_i$ where the minimum SNR for channels is maximized.

3.7 Optimum graphene photodetector placement and Width Selection

Symmetric metal-graphene-metal devices give nonuniform photocurrent, e.g., even zero response at the middle of graphene channel. Therefore, without changing length, but cutting to M parts with $W_i,\ i \in [1, M]$ and placing them at positions x_i can increase the minimum SNR among channels as shown in Fig. 3.18.

Denoting the SNR output of combining scheme at $x_p^{ind} = (p - 0.5)\,W_{ls},\ p \in [1, N_s]$ as $\gamma_{ntype}^{DC}(\nu, p)$ where $ntype$ denotes noise limited regimes, nonlinear optimization problem maximizing the minimum SNR among parallel line-scan channels is defined as

$$\begin{aligned} &\max_{\mathbf{w},\mathbf{x}} \min_{p=1,2,...,N_s} \quad \gamma_{ntype}^{MRC,EGC}(\nu, p) \\ &\textbf{s.t. } \mathbf{w}^T\,\mathbf{1} = W_{tot},\ W_{min} \le \mathbf{w} \le W_{tot},\ 0 \le \mathbf{x} \le L \end{aligned} \tag{64}$$

where $\mathbf{x} = [x_1\, x_2 \ldots x_M]$ and W_{min} is the minimum zero-band gap width, i.e., ≈ 25 nm [51, 192]. The problem complexity is reduced by separating the width and placement selection by forming M equal width receivers. Furthermore, since $|\varsigma_s(x^{ind}, x_i)|$ and $\varsigma_s^2(x^{ind}, x_i)$

are discontinuous at $x^{ind} - x_i \in \{0, 0.5\,L, L\}$ and $\{0,\ L\}$, respectively, $\mathbf{x}$ is divided into intervals to obtain continuous constraints. Hence, problem of shot noise limited regime is converted to the following,

$$\max_{\mathbf{x}}\ u\ \ \textbf{s.t.}\ C_2^{'}\sum_{i=1}^{M}\varsigma_s(x_p^{ind}, x_i)\,W_i \geq u,\ \ p \in [1, N_s] \tag{65}$$

which is a linear programming (LP) problem solved with LIPSOL (Linear Interior Point Solver) implemented under MATLAB [200]. Problem for thermal noise limited case is given as

$$\max_{\mathbf{x}}\ u\ \ \textbf{s.t.}\ C_k^{'}\sum_{i=1}^{M}\varsigma_s^2(x_p^{ind}, x_i)\,W_i^j \geq u,\ \ p \in [1, N_s] \tag{66}$$

where $\mathbf{x}_{min} \leq \mathbf{x} \leq \mathbf{x}_{max}$, k equals to 3 and 4, j equals to 1 and 2 for T-R_g and T-R_L noise limited cases, respectively. The constraints can be represented as $\mathbf{x}^T\,\mathbf{Q_p}\,\mathbf{x}+\mathbf{b_p}^T\mathbf{x}+c_p+u \leq 0$ where Q_p is diagonal matrix with elements h_i on diagonal. If $x_p^{ind} - L < x_i < x_p^{ind}$, then $h_i = 4\,f_{i,j,k}$, $b_p(i) = 4\,f_{i,j,k}\,y_p$ and $c_p = -\sum_{i=1}^{M} f_{i,j,k}\,y_p^2$ and they are all zeros otherwise where $i \in [1, M]$, $f_{i,j,k} = -C_k^{'}W_i^j q^2 C_1^2/\,L^2$ and $y_p = (L - 2\,x_p^{ind})$. Quadratic concave problem (negative semidefinite Q_p) can be solved by either using semidefinite programming relaxation introducing $\mathbf{X} = \mathbf{x}\mathbf{x}^T$ or LP relaxation of reformulation-linearization technique (RLT) [4],

$$\begin{aligned}\max_{\mathbf{x}}\ \ u\ \ \textbf{s.t.}\ \ &\mathrm{Tr}(\mathbf{Q_p}\mathbf{X}) + \mathbf{b_p}^T\mathbf{x} + \mathbf{c_p} + u \leq 0,\\ &\mathbf{X} - \mathbf{x}_{min}\,\mathbf{x}^T - \mathbf{x}\,\mathbf{x}_{min}^T + \mathbf{x}_{min}\,\mathbf{x}_{min}^T \geq 0,\\ &\mathbf{X} - \mathbf{x}_{max}\,\mathbf{x}^T - \mathbf{x}\,\mathbf{x}_{max}^T + \mathbf{x}_{max}\,\mathbf{x}_{max}^T \geq 0,\\ &\mathbf{X} - \mathbf{x}_{min}\,\mathbf{x}^T - \mathbf{x}\,\mathbf{x}_{max}^T + \mathbf{x}_{min}\,\mathbf{x}_{max}^T \leq 0\end{aligned} \tag{67}$$

where $p \in [1,\ N_s]$, Tr() is the trace operator, $\mathbf{X} = \mathbf{X}^T$. Then, by dividing the interval for $0 \leq \mathbf{x} \leq L$ into various $\mathbf{x}_{min} \leq \mathbf{x} \leq \mathbf{x}_{max}$ where $|\varsigma_s(x^{ind}, x_i)|$ and $\varsigma_s^2(x^{ind}, x_i)$ are continuous and trying all combinations of intervals for each receiver, the maximum of the optimum solutions is chosen. Next, graphene photodetector models and optimizations are numerically simulated for practical power levels.

3.8 Numerical Simulations and Results

In this thesis, η_{In} is based on experiments from [141, 187, 188] choosing the observed maximum $\approx 30\%$ which can be further improved by better receiver design in future.

Single receiver width and length are chosen as $W_{tot} = 1\,\mu$m and $L = 1.45\,\mu$m, respectively, based on [187]. Single receiver device is cut to $M \in [2, 40]$ receivers of $W_i = W_{tot}/M$ in multi-receiver combining scheme.

The resistance measurements show variations among experiments [181, 189] as discussed in the subsection-3.1.1.1. In [189], $R_c \approx (185\,\Omega\,\mu\text{m})\,/\,W$ is measured for Pd/Au contact at room temperature and for negative V_G (p-channel) emphasizing perfect contacts can decrease R_c 2 to 3 times. Thus, assuming perfect contacts, $R_c \approx (60\,\Omega\,\mu\text{m})\,/\,W$ is taken in this work. $\rho_{sh} \approx 400\,\Omega\,/$ sq can be inferred from the plots in [189] for negative V_G. Therefore, $R_g = (400\,L + 60)\,/\,W$ where L and W are in μm.

For $0.025 < W < 1$ μm and $L = 1.45\,\mu$m, R_g is between 0.64-25.6 KΩ. Even for $R_{eq} \approx 25.6$ KΩ for $R_L \gg R_g$, to observe shot noise limited regime, i.e., $(\sigma_s^g)^2 + (\sigma_{therm}^{eq})^2 < 0.1\,(\sigma_s^p)^2$, I_p needs to be larger than $80\,\mu$A which is out of range for experiments with nA range photocurrents for practical power levels [187, 188]. Therefore, for diversity optimizations, only thermal noise limited regimes are analyzed. Two different R_L values are used, i.e., $R_L = 50\,\Omega$ [188] and $R_L \geq 256\,$KΩ leading to T-R_L and T-R_g noise limited regimes with $R_{eq} \approx 50\,\Omega$ and $R_{eq} \approx R_g$, respectively.

Transmit power levels are chosen based on experiments having $\approx$ 50-1000 W/mm^2 densities [145, 187, 188]. Therefore, $P_{in} \approx 1$ KW/mm^2 is used to find practical BER. However, BER is computed for wide range of power levels. In comparison of multi-receiver combining schemes with single receiver, total incident power on $0 < x^{ind} < L$ is assumed to be same for both. Since in diversity combining scheme the incident area is smaller than single receiver which covers whole $0 < x^{ind} < L$, incident optical power density of diversity combining schemes are increased to give the same total incident power by calculating the graphene area.

The optical wavelength is chosen as $\lambda = 1.55\,\mu$m (193 THz) based on the experiments [6, 124, 188] which can be chosen from the ultrawideband region among wavelengths 0.3-$6\,\mu$m where zero-band gap absorption of light is possible.

Line-scan positions are chosen as $\mathbf{x}^{ind} = [0.1\ 0.3\ 0.5\ 0.7\ 0.9] \times L$ where N_s = 5 and $W_{ls} = 0.29\,\mu$m which is approximately average of 150-550 nm of experiments in [125, 187]. The number of positions can be increased with higher resolution W_{ls}, however, to reduce the complexity, experimental W_{ls} resolution is good enough.

In this thesis, SiO_2 of $\epsilon_r = 3.9$ and $t_{ox} = 300$ nm is used [188]. As discussed in subsection-3.1.1.3, for large negative V_G and thick oxide substrates, $C_Q \gg C_{ox}$ [48] and it results in $C_g \approx C_{ox} = 0.115$ fF/μm^2. However, receiver pad capacitance is generally 2 to 3 orders of magnitude higher than graphene gate capacitance, e.g., C_p of 20-25 fF [188], which results in a parasitic capacitance limited cut-off rate [102, 188]. RC and transit time limited rates are $f_c = 1\,/\,(2\,\pi\,R_{eq}\,C_{eq})$ and $f_c = 3.5\,/\,2\,\pi\,t_{tr}$, respectively, where t_{tr} is delay of generated carriers to reach contacts. Carrier saturation velocity of 5.5×10^5 m/s assumed as the saturation velocity as discussed in subsection-3.1.1.2 leads to maximum $t_{tr} = 1.32$ ps and minimum 0.26 ps for light incident on $0.5\,L$ and $0.1\,L$, respectively [188]. The intrinsic RC limited rates are $f_c^{min} = 1\,/\,(2\,\pi\,R_0\,0.115\,L) \approx 1.5$ THz for T-R_g noise limited regime and $f_c^{max} = 1\,/\,(2\,\pi\,R_L\,0.115\,W_{min}\,L) \approx 760$ THz for T-R_L noise limited regime with $W_{min} = 25$. Transit time limited rates are $f_c^{min} \approx 0.42$ THz and $f_c^{max} \approx 2.2$ THz for $\mathbf{x}^{ind}$. Pad capacitance ($C_p = 20$ fF) RC limited rates are ≈ 310 MHz with $W = W_{min}$ and ≈ 12 GHz with $W = W_{tot}$ for T-R_g noise limited case. However, same rates are ≈ 160 GHz for T-R_L noise limited case for both W_{min} and W_{tot}. By using C_p limited rates, maximum ≈ 12 GHz and ≈ 0.16 THz rates for T-R_g and T-R_L noise limited regimes, respectively, are simulated for $W = W_{tot}$. Minimum rate is fixed to 100 KHz to diminish 1/f noise.

To reduce search space in (65) and (67) for large M, the optimum $\mathbf{x}$ for $M \leq 10$ is analyzed and $\mathbf{x}_{opt}$ values are observed to be around the elements of $\mathbf{x}^{ind}$. Then, by averaging the optimum placements, the sets $x_i\,/\,L \in S_1 = \{0.05, 0.297, 0.497, 0.687, 0.887\}$ and

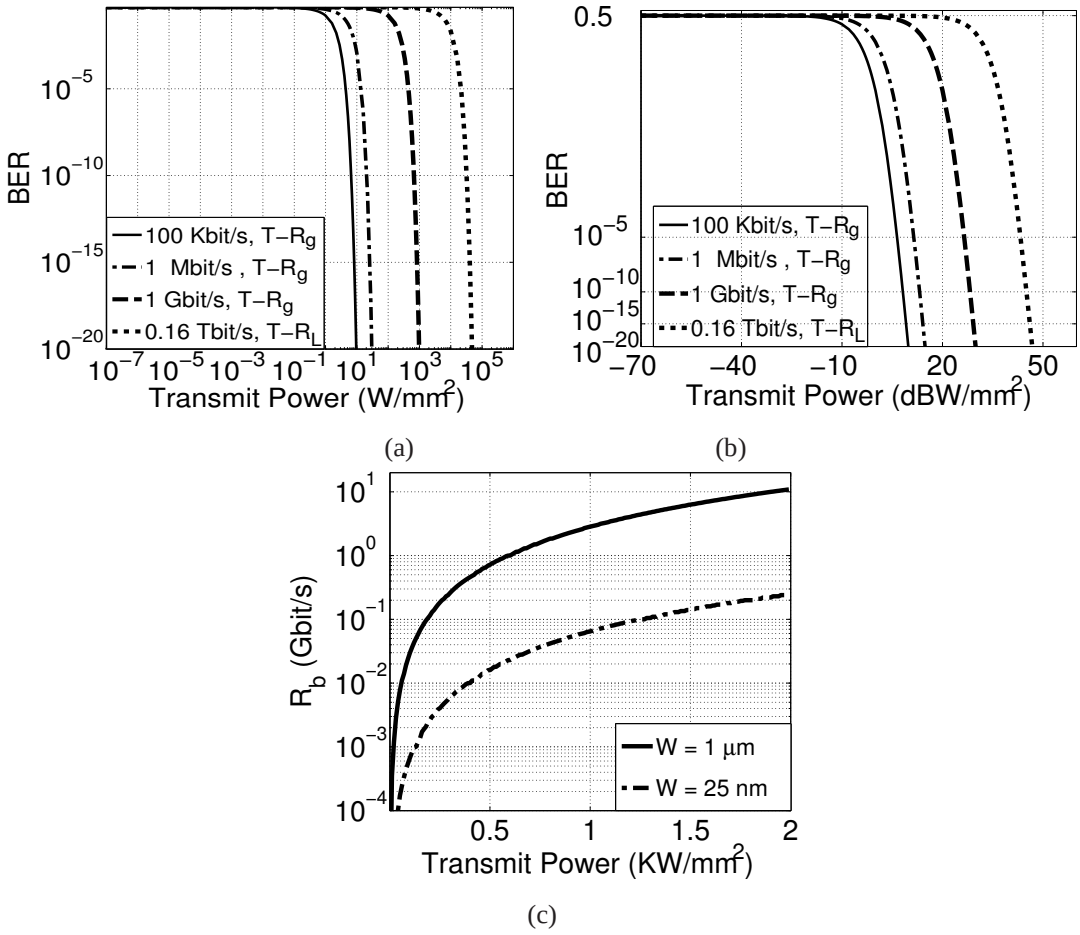

Figure 3.19: BER vs. transmit power for varying R_b and thermal noise limited regions with graphene photodetector of $W_{tot} = 1\ \mu$m for (a) logarithmic and (b) double logarithmic (y-axis) plot, (c) R_b vs. practical transmit power levels for T-R_g noise limited region with graphene photodetectors of $W = 1\ \mu$m and 25 nm where BER is 10^{-8}.

$S_2 = \{0.075, 0.27, 0.483, 0.696, 0.883\}$ are constructed for shot and thermal noise limited cases, respectively, to be used as placement sets for larger M. Furthermore, the number of photodetectors with placements $S_{1,2}(n)$ is observed to be larger than the ones with $S_{1,2}(n+1)$ as M gets larger by further reducing the search space. Next, BER performance of single receiver is analyzed, and then combining methods are applied on multi-receiver graphene photodetector devices.

3.8.1 BER Performance of Graphene Photodetectors

BER of IM/DD non-return-to-zero on-off keying modulation type is found by using (38). In Fig. 3.19(a) and (b), BER of single receiver for incident light on whole $0 \leq x^{ind} \leq L/2$ region is shown for T-R_g noise limited regime. Furthermore, for BER threshold of 10^{-8}, R_b vs. transmit power is shown in Fig. 3.19(c) with practical power levels for both $W = W_{min}$ and $W = W_{tot}$. It is observed that even with very low power of ≈ 1 W/mm^2, it is possible to achieve hundreds of Kb/s transmission with very low BER where the photocurrent generation region is $W_{tot} \times L/2 = 0.725\,\mu$m^2. It can also succeed tens of Gb/s rate with 2 KW/mm^2 input power. Moreover, even with small area of $0.025 \times 0.775 = 0.02\,\mu$m^2, it is possible to achieve the rate of hundreds of Mb/s with 2 KW/mm^2 transmit power. Next, performance of multi-receiver combining methods with optimum placement are compared with single receiver.

3.8.2 Diversity Combining and Optimum Receiver Placement

In comparing multi-receiver diversity schemes with single receiver, metrics $G_{MR/SR}^{max,min} \equiv SNR_{DC}^{max,min}/SNR_S^{max}$, $G_{MR/SR}(x_{ind}) \equiv SNR_{DC}(x_{ind})/SNR_S(x_{ind})$ and $G_{MRC/EGC}$ are defined. $SNR_{DC}(x_{ind})$ is the SNR obtained when x^{ind} is illuminated and its minimum SNR_{DC}^{min}, i.e., the optimized value, and SNR_{DC}^{max} are the minimum and maximum SNR, respectively, among multi-receiver spatial channels when only the respective channel at x^{ind} receives optical signal. Similarly, $SNR_S(x_{ind})$ is the SNR for optical signal at x^{ind} for the single receiver device and SNR_S^{max} is the maximum SNR observed in single receiver channels, i.e., at $x_1^{ind} = 0.1\,L$. The rate $G_{MR/SR}(x_{ind})$ gives the achievable SNR gain at the respective channels which can be used to observe the improvement in efficiency at channel level. The ratio gives the infinity value at the middle channel since zero output current is obtained with the single receiver device. Ratio of optimized minimum values of diversity combining methods is $G_{MRC/EGC} \equiv SNR_{MRC}^{min}\,/\,SNR_{EGC}^{min}$.

In Fig. 3.20(a) and (b), for T-R_g noise limited case, SNR^{min} is increased and saturates

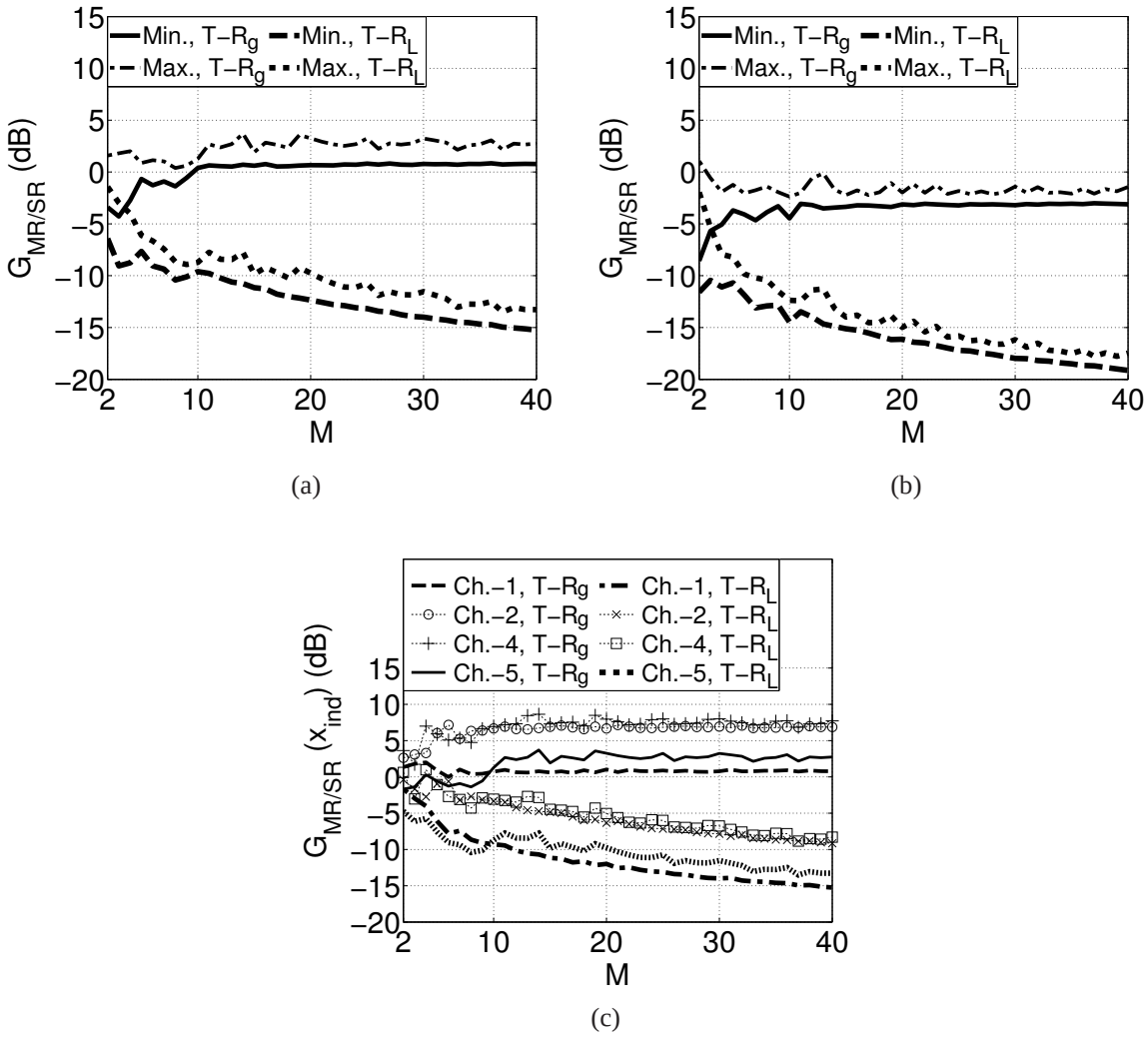

Figure 3.20: $G_{MR/SR}^{max,min}$ vs. M for (a) maximal ratio combining and (b) equal gain combining, (c) $G_{MR/SR}(x^{ind})$ vs. M for maximal ratio combining at various channel indices, i.e., x_k^{ind}, $k = \{1,\ 2,\ 4,\ 5\}$ for T-R_g and T-R_L noise limited cases.

for larger M. Maximal ratio combining in T-R_g noise limited regime not only creates more uniform SNRs among channels but also achieves higher SNR than the maximum SNR of single receiver channels, i.e., SNR_S^{max}. Therefore, the optimization increases the efficiency of the graphene photodetector not only by increasing SNR in the worst performance channels, e.g., zero SNR at the middle of single receiver, and creating a illumination position independent device performance but also increases the SNR of other channels exceeding the performance of the single receiver at specific line-scans. SNR_{MRC}^{min} reaches ≈ 0.8

dB gain and SNR_{MRC}^{max} reaches $\approx$ 3 dB gain such that the ratio between minimum and the maximum saturates. Furthermore, it is observed that the gain $G_{MR/SR}(x_{ind})$ of maximal ratio combining at various channels of line-scan positions, i.e., $Ch.$-1 to $Ch.$-5 for $x_k^{ind} = (2\,k\,-\,1)\,0.1\,L,\, k \in \{1,\,2,\,4,\,5\}$, reaches as much as ≈ 8 dB for large M as shown in Fig. 3.20(c) concluding that diversity combining improves the line-scan performance of single receiver significantly. The performance of the channel at the middle, i.e., $Ch.$-3 of x_3^{ind}, is not plotted in Fig. 3.20(c) since it gives zero SNR in single receiver device. The optimization with respect to equal gain combining achieves to have SNR^{min} and SNR^{max} performances of -3 and -2 dB, respectively, at large M.

For T-RL noise limited regime, diversity combining performs best at minimal number of M, i.e., $M = 2$. SNR_{MRC}^{min} and SNR_{EGC}^{min} gains are ≈ -6.5 and ≈ -11.5 dB, respectively, and SNR_{MRC}^{max} and SNR_{EGC}^{max} gains are ≈ -1.5 and ≈ -2 dB, respectively, such that maximum SNR channels do not degrade too much. Therefore, for T-RL noise limited region, uniform performance channels are obtained by sacrificing SNR in other channels. However, ≈ 0.5 and ≈ 1 dB $G_{MR/SR}(x_{ind})$ gains are achieved with maximal ratio combining for $M = 2$ and 4, respectively, at x_4^{ind} as shown in Fig. 3.20(c). Therefore, it is possible to improve SNR in some channels for T-RL noise limited regime in addition to obtaining homogeneous channels.

The ratio between $G_{MR/SR}$ values of T-R_g and T-R_L noise limited regimes is M which can be calculated by using (60-63) and observing both schemes give same optimal placements. Due to this decreasing performance with increasing M, the degradation observed in Fig. 3.20(a) and (b) occurs. The increase in SNR^{min} performance with increasing M for T-R_g noise limited case of maximal ratio combining scheme is explained as the following. From (59) and (63), it is calculated that

$$\frac{SNR_{DC}^{max,min}}{SNR_{S}^{max}} = \frac{P_{MR}^2}{P_{SR}^2} \frac{\sum_{i=1}^{M} \varsigma_s^2\left(x_{p_1,p_2}^{ind}, x_i\right)}{M\,\varsigma_s^2\left(x_1^{ind}, 0\right)} \tag{68}$$

where $p_1,\, p_2 \in [1, N_s]$ are the respective channel indices of maximal ratio combining scheme giving the maximum and minimum SNR, respectively, and P_{MR} and P_{SR} are the

incident powers on multi-receiver and single receiver geometries, since the power density is increased for multi-receiver scheme to make the total incident power same with single receiver case. It is observed that the second fractional expression in (68), i.e., placement gain, is ≈ 0.23 for $M = 2,\ 3$ and then starts to oscillate around 0.35 as M increases. The power gain, i.e., P_{MR} / P_{SR}, starts from 1.38 and gradually increases with M and oscillates around 1.83 as M further increases. Therefore, SNR improvement with increasing M is the result of the combined effect of power and placement gains.

The comparison between optimum equal gain and maximal ratio combining placements of multi and single receiver devices is shown in Fig. 3.21(a). If optimization is performed independently for two schemes, maximal ratio combining gain over equal gain combining is maximum at $M = 2$ with ≈ 5.2 dB, minimum at $M = 3$ with 1.39 dB and saturates around 4 dB as M is increased. If maximal ratio combining optimum placement is used for equal gain combining, gain saturates around 6 dB for large M, i.e., higher than independent one since optimization is performed for maximal ratio combining. Furthermore, if equal gain combining optimum placement is used for maximal ratio combining, gain becomes much less showing that maximal ratio combining performance is not much different from equal gain combining in an optimized placement for equal gain combining. $G_{MRC/EGC}$ by using (61, 63) can be analyzed as

$$G_{MRC/EGC} = \frac{P_{MRC}^2}{P_{EGC}^2} \frac{M \sum_{i=1}^{M} \varsigma_s^2 \left(x_{p_1}^{ind}, x_i\right)}{\left(\sum_{i=1}^{M} |\varsigma_s \left(x_{p_2}^{ind}, x_i\right)|\right)^2} \tag{69}$$

where $p_1,\ p_2 \in [1, N_s]$ are channel indices having minimum SNR. The power and placement gains start from 1.15 and 2.5, respectively, at $M = 2$ to values oscillating around 1.3 and 1.4, respectively, for larger M. Therefore, power gain of maximal ratio combining increases with M, but the placement gain decreases leading to combined effect shown in Fig. 3.21.

The rates on channels comparing multi and single receiver devices are shown in Fig. 3.21(b) where BER is 10^{-8} and incident power for single receiver is 1 KW/mm^2. Even the

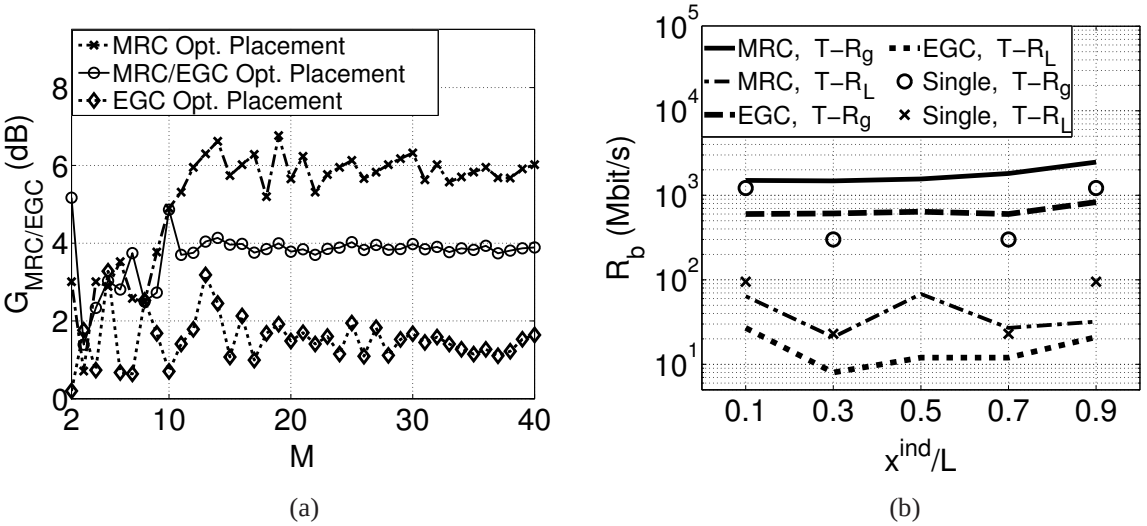

(a) (b)

Figure 3.21: (a) Maximal ratio combining vs. equal gain combining for varying M showing the gain $G_{MRC/EGC}$ for placements optimized with respect to maximal ratio and equal gain combining, (b) R_b vs. parallel line-scan channel for single receiver and multi-receiver devices for BER threshold of 10^{-8} and incident power of 1 KW/mm^2.

equal gain combining scheme for T-R_g noise limited regime achieves almost uniform rates as much as ≈ 600 Mb/s by increasing single receiver rates between 2nd and 4th channels, i.e., between $\approx$ 0-300 Mb/s. Maximal ratio combining scheme increases the corresponding rates to $\approx$ 1.5-1.8 Gb/s showing the significant improvement and uniformity along the channel.

In conclusion, single-layer symmetric metal-graphene-metal photodetectors are analyzed in terms of SNR, BER and data rate performance metrics for IM/DD non-return-to-zero on-off keying optical modulation by emphasizing the graphene layer width dependence. Shot and thermal noise limited regimes are defined observing the prevailing character of thermal noise limited region for practical power levels. Tens of Gbit/s data rates are shown to be achievable with very low BERs for nanoscale size graphene photodetectors. Furthermore, multi-receiver graphene photodetectors are defined combined with maximal ratio and equal gain diversity combining schemes presenting a method to

increase the graphene photodetector efficiency. Parallel line-scan optical networking transmit topology is introduced by emphasizing the nonuniform SNR among single receiver spatial channels. The homogeneity of channel performances are achieved by optimizing the geometrical placement of the defined multi-receiver devices with same total graphene area combined with diversity techniques. Maximization of the minimum SNR in spatial channels are defined as concave quadratic and linear optimization problems with a reformulation-linearization technique solution. Multi-receiver device with diversity combining techniques and optimum placement is shown to have spatial channels with more uniform and stronger SNR. This novel communication theoretical study lays the foundations of graphene photodetectors to be utilized in the future nanoscale optical communication networks.

CHAPTER 4

CARBON NANOTUBE NANOSCALE WIRELESS OPTICAL COMMUNICATION RECEIVERS

Carbon nanotube starting with the fundamental works of Iijima [71,73] is a ground-breaking material discovered two decades ago with tremendous number of applications in physical and technological sciences including molecular electronics, quantum computing and nanoscale communications. Single-walled carbon nanotubes (SWNTs) as one dimensional nanometer size strips of graphene are promising to be utilized in future nanonetworks due to fascinating mechanical, electrical and thermal properties [5, 78]. Its basic properties compared with graphene and other conventional materials are seen in Table-3.1 of Chapter-3. The summary of the history of carbon nanotube with emphasis on the important events especially related to carbon nanotube photodetectors can be seen in Table-4.1.

Its story begins in cosmetic eyeliners of ancient times and the strong Damascus swords in middle ages and extends to its modern generation in 20th century resulting in photodetectors, CNT field effect transistors and nanoscale light sources.

Carbon nanotube field-effect transistors competitive with the state-of-the-art silicon transistors are promising candidates for future nanoscale electronics [78]. Furthermore, with tunable band-gap, wide spectral range response and polarized absorption, SWNTs are efficient photodetectors in nanoscale optoelectronics. Moreover, Schottky barrier CNTFET photodiodes composed of semiconducting SWNT and metal contacts (M-SWNT-M) have a considerable quantum efficiency and very small dark currents [26, 29, 30, 52, 65, 147, 150, 196]. Photodiodes built with CNT p-n junctions show current-voltage characteristics similar to conventional diodes [92, 114, 168, 182]. SWNTs can be used as photovoltaic

Table 4.1: Carbon Nanotube Timeline

Year	Event
800 B.C.	the presence of CNTs in sooty cosmetic eyeliner *kajal* of Indian women
M.A.	the presence of CNTs on Damascus steel probably due to forging process
1946	observation of tubular carbon structures with 100 nm diameter by Watson and Kaufmann
1947	50 nm diameter graphitic carbon fibers by Radushkevich and Lukyanovich
1976	nanometer scale diameter tubes with vapor-growth technique by Oberlin, Endo, and Koyama
1979	evidence of CNTs found on carbon arc anodes by John Abrahamson
1981	suggestion of the first chirality models of CNTs by Kolesnik et al.
1991	the discovery of double-walled and multi-walled CNTs by Iijima
1993	the discovery of single-walled CNT by Iijima in NEC and Bethune et al. in IBM
1998	first carbon nanotube FET by Tans, Verschueren and Dekker
2001	observation of photoconductivity of single-walled CNT films by Fujiwara et. al.
2003	observation of photoconductivity of single CNTFET by Freitag et al. in IBM
2003	observation of electrically induced IR optical emission from single CNT-FET
2009	observation of multiple-electron hole pair generation in single CNT p-n junction photodiode possibly opening the way for ultra-efficient photo-voltaic devices exceeding the Shockley-Queisser limit by Gabor et al.
2011	ultra fast response of CNT photodetector with picosecond photocurrent response by Prechtel et al.

cells [25–27,97,182]. These devices perform optical-to-electrical conversion and are strong candidates for nanoscale optoelectronics.

In addition, SWNTs are candidates in Network-on-Chip (NoC) platforms for future wireless interconnects as optical antennas. CNTs operate in THz and optical frequency range, have large bandwidth and perform as both transmitter and receiver with simple ON-OFF keying [24, 56, 133, 134]. CNTs performing as optical antennas can achieve low-cost ultra-fast computer technologies [74]. In [24, 56, 133, 134], CNTs are offered as THz range on-chip nanoscale antennas. The advantages of wireless NoCs (WiNoC) in terms of

throughput and large bandwidths of CNT optical antennas (500 GHz) are discussed. Antenna absorbance is shown to depend quadratically on the nanotube diameter and linearly on the conductivity. Furthermore, the time (TDM), frequency (FDM) and polarization division multiplexing schemes are discussed [134]. However, there is no theoretical modeling of performance characteristics, e.g., signal-to-noise ratio, bit error rate and achievable data rates, for a CNT nanoscale optical receiver. It is of fundamental importance to model the diameter-dependent performance, validate with existing experiments and discuss power allocation for a nanoscale optical network of receivers having performance differences due to diameter variation.

In this thesis, for the first time, CNT receivers based on M-SWNT-M photodiodes with small diameter nanotubes, i.e., (0.7-1.2) nm, are modeled theoretically within an optical communication perspective. Photocurrent and noise modeling are combined to compute the diameter dependent performance metrics, i.e., SNR, BER and cut-off bit rate or receiver data rate, i.e., R_b. The parameter fitting of the model with the experiments in literature is achieved. The performance is analyzed for IM/DD non-return-to-zero on-off keying modulation in shot, dark and thermal noise limited (NL) cases. The multi-user CNT ad hoc network topology for information broadcast is presented and the maximization of the minimum SNR is modeled as a NP-hard quadratic power allocation problem among transmitter frequencies for dark and thermal noise limited cases. Linear programming (LP) and semidefinite programming relaxation (SDP) solutions combined with Branch and Bound (BB) framework, i.e., SDP-BB, are presented. Uniform power allocation (UPA) with practical transmit power levels results in hundreds of Mb/s data rate with very low BERs. Furthermore, optimum power allocation (OPA) gives significant improvement in terms of SNR gain and R_b increasing with the diameter range. Thermal noise limited case gives the highest gain while shot noise limited gives the highest data rate.

The organization of the chapter is as the following. Firstly, the physical and optical properties of carbon nanotubes are introduced. Then, CNT photodetector applications in

the literature are reviewed. Then, CNTFETs composed of semiconducting SWNT and metal contacts (M-SWNT-M) are used as photodiode receiver in nanoscale optical communication by theoretically modeling diameter dependent characteristics for shot, dark and thermal noise limited cases. SNR, BER and cut-off bit rate performances are analyzed for IM/DD modulation. Optical transmitter models are discussed. Furthermore, multi-receiver CNT nanoscale network topology and multi-user broadcast for CNT nanoscale optical network topology are presented. The minimum SNR is maximized solving NP-hard max-min power allocation problem with semidefinite programming relaxation and BB framework. The significant performance improvement is observed compared with uniform power allocation. In numerical analysis, after discussing parameter fitting of proposed model with existing experiments, cut-off data rates and transmitter power levels, BER and SNR performances are analyzed. Max-min SNR is numerically evaluated and compared with uniform power allocation. Derived model is compared with existing experiments and hundreds of Mb/s data rate is achievable with very low BERs.

4.1 Properties of Carbon Nanotubes

CNTs are the rolled up version of graphene in a cylindrical fashion [158]. A single-walled carbon nanotube is formed by rolling a sheet of graphene while multi-walled carbon nanotube (MWNT) consists of multiple rolled layers of graphene in a concentric manner. A SWNT has a diameter ranging from 0.5 to 5 nm with 0.6-1.2 nm denoted as small diameter [68] and lengths ranging from micrometers to centimeters [184]. A MWNT has walls with the spacing comparable to the graphite interlayer spacing, i.e., 0.34 nm. Carbon nanotubes have very small diameter confining electrons to move along the length leading to a quasi-1D structure with a significantly large length over diameter ratio not observed in any other structure.

CNTs are indexed by indices $(n,\, m)$ which specifies the way the graphene is rolled up

along the chiral vector defined by

$$\mathbf{C} = \mathbf{n}\overrightarrow{a_1} + \mathbf{m}\overrightarrow{a_2},\ 0 \leq m \leq\leq n \tag{70}$$

where the vectors $\overrightarrow{a_1}$ and $\overrightarrow{a_2}$ are the basis vectors of graphene which are defined in (41) and shown in Fig. 4.1.

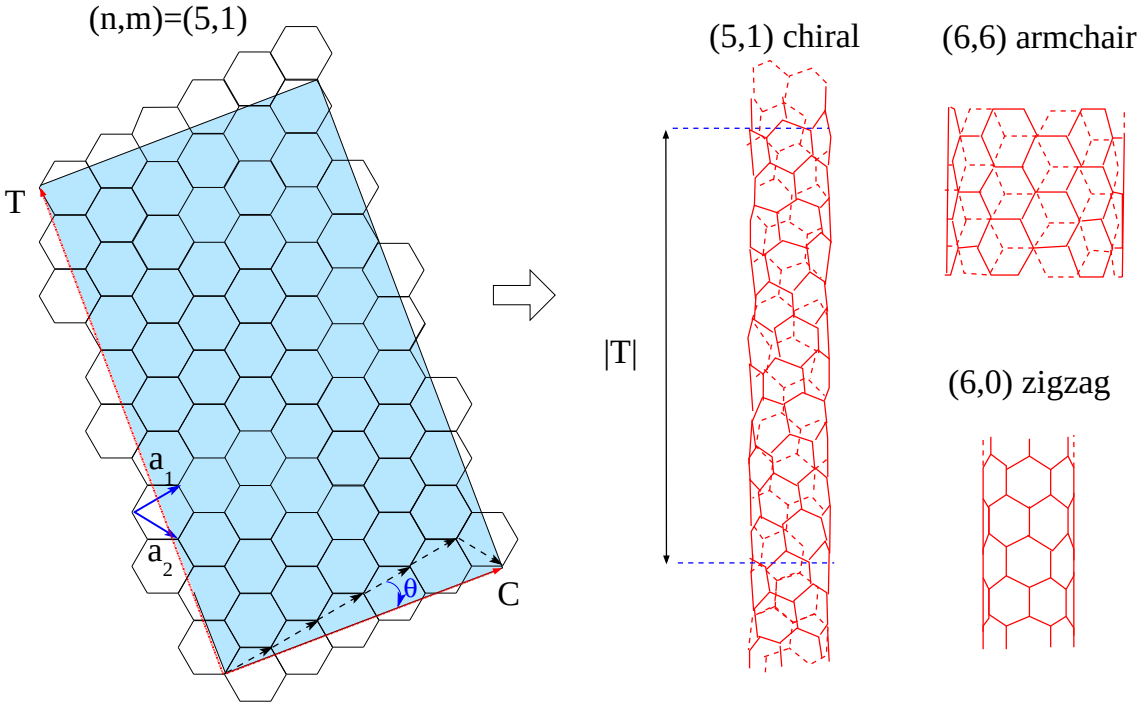

Figure 4.1: Construction of SWNT by rolling the graphene along the chiral vector and the illustrative SWNTS showing (6,0) zigzag, (6,6) armchair and (5,1) chiral nanotube [158, 184].

The chiral vector $\mathbf{C}$ completely characterizes the nanotube type and the circumference of the resulting nanotube is equal to $|\mathbf{C}|$. The other parameters are the translation vector T defining periodicity of the nanotube along the nanotube axis and the chiral angle θ, which is the angle between the chiral vector and the basis vector $\overrightarrow{a_1}$, can be found by using the indices (n, m). The chiral angle is between 0^o (zigzag) and 30^o (armchair) and it is given by the following,

$$\theta = \tan^{-1}\left(\sqrt{3}\, m/(2n+m)\right) \tag{71}$$

The diameter of the tube in terms of the indexes is given as the following,

$$d_t = a_{CC}\sqrt{3(n^2 + nm + m^2)}/\pi \tag{72}$$

The length of the translation vector, which is perpendicular to the chiral vector, is given as the following,

$$|\mathbf{T}| = \frac{\sqrt{3}\,\mathbf{C}}{g_{cd}} \tag{73}$$

where g_{cd} is the greatest common divisor of $2\,n\,+\,m$ and $2\,m\,+\,n$ [184]. In addition to this, the number of hexagons in a unit cell can be found by the following,

$$N_h \,=\, \frac{2\,|C|^2}{3\,a_{CC}^2\,g_{cd}} \tag{74}$$

where $(5, 1)$ nanotube has 62 hexagons as shown in Fig. 4.1. On the other hand, the index $(n,\, m)$ and the chiral vector specify the type of the nanotube as metallic, semimetallic, or semiconducting. Furthermore, if $2\,n\,+\,m\,=3\,q$ or $n\,-\,m = 3\,q$ where q is integer, then, the nanotube shows metallic behavior and otherwise the nanotube is a semiconductor.

Carbon nanotubes have tremendous features which are not observable in any other material. It has a significant atomic-scale perfection making it chemically inert [78] and melting point of perfect SWNTS is around 4800 K better than any other metal. They are the strongest materials in terms of tensile strength due to sp^2 bonds such that two orders of magnitude stronger than steel. Combining with their ultra-light weight brings significant strength-to-weight ratios higher than any other material such that the nanotube is one order of magnitude lighter than steel. Graphene and carbon nanotube have extremely large thermal conductivity which are not observed even in diamond, i.e., single layer graphene has 5300 W/(m K) at room temperature and carbon nanotube has 3000-6600 W/(m K) while Silicon has 145 W/(m K) and nearly isotopically pure diamond has 3320 W/(m K) thermal conductivities [12, 129]. Furthermore, SWNTs with their quasi-1D structure behave as ballistic conductors of electrons at room temperature.

Carbon nanotubes with their magnificent properties are candidates to be utilized in

many areas of physical, chemical or technological sciences. Some of them can be listed as the following [7, 78, 139, 184],

- Opto-electronic and photonic applications; photodetectors, electrically pumped and modulated solid-state nanoscale light sources, light-emitting diodes, and lasers due to unique optical properties like equal effective masses of electrons and holes, tunable bandgap, significant ballistic transport of carriers, photodetection efficiency and electrostatic advantages.

- Molecular electronics circuit applications due to long electron mean-free path, ballistic conduction of carriers, implementation of very efficient carbon nanotube field effect transistors, spintronics and quantum computing based properties.

- Strong, transparent and conductive composites.

- Nanotube yarns which are tough even competing with kevlar.

- Probe tips for scanning probe microscopy, electron guns, and bright, ultra-flat displays due to the large aspect ratio and high melting point.

- Electrodes in super capacitors and fuel cells due to high conductivity and high surface-to-volume ratio.

- Chemical, molecular and biological sensors due to the structural stability and tunable electrical-optical properties, reduced dimensionality and large surface-to-volume ratio.

- Nano-electromechanical systems due to tiny and slender geometry, high directional stiffness, low weight, chemical stability, significant electrical and thermal properties, and enduring large strains without breaking.

- Integrated electronics on flexible substrates due to high mobilities, currents and optical transmittance, and robust mechanical properties.

- Hydrogen storage by SWNTs due to participation of all the carbon atoms in adsorbing and suitability to be used as an empty nano-container.

- Bio-compatible tools due to nanometer-size diameter, cylindrical shape, and chemical inertness.

Next, the electronic and optical properties of nanotubes are analyzed which are the main properties relating to the subject of the thesis.

4.1.1 Electronic Properties

The electronic-band structure of CNT can be obtained by constructing the Brillouin zone and reciprocal lattice of CNTs. The wavevectors defining the CNT Brillouin zone are the reciprocals of the primitive unit cell vectors given by

$$\mathrm{e}^{\imath\,(\mathbf{K}_T + \mathbf{K}_C)\bullet(\mathbf{C}+\mathbf{T})} \tag{75}$$

where $\mathbf{K}_T$ and $\mathbf{K}_C$ are reciprocal lattice vectors along the axis and the circumference, respectively, which can be given in terms of reciprocal lattice base vectors of graphene given in (43). Then by using periodic boundary conditions of Bloch wave function, the general Brillouin zone wavevector of nanotube, i.e., $\mathbf{k}$, is found as the following [184],

$$\mathbf{k} \,=\, k\,\frac{\mathbf{K_T}}{2\,\pi\,/\,|\mathbf{T}|} \,+\, j\,\mathbf{K_C},\; j \,=\, 0,\,1,\,...,\,N_h - 1,\;\; -\pi\,/\,T \,\leq\, k \,\leq\, \pi\,/\,T \tag{76}$$

where the reciprocal lattice vectors with magnitudes $|\mathbf{K}_T| = 2\,\pi\,/\,|\mathbf{T}|$ and $|\mathbf{K}_C| = 2\,\pi\,/\,|\mathbf{C}|$ are as the following,

$$\mathbf{K}_T = = \,\frac{m\,\overrightarrow{b_1} \,-\, n\,\overrightarrow{b_2}}{N_h};\;\; \mathbf{K}_C \,=\, \frac{(2\,n \,+\, m)\;\overrightarrow{b_1} \,+\, (2\,m \,+\, n)\;\overrightarrow{b_2}}{N_h\,g_{dc}} \tag{77}$$

Therefore, for each value of j, a 1D band of the wave vectors k ranging from $-\pi\,/\,T$ to $\pi\,/\,T$ is the cut of graphene's 2D Brillouin zone as shown in Fig. 4.2 for tubes of various family.

The family of the tubes are defined with respect to the passage through reciprocal K such that the nanotube will gain metallic behavior. It is seen that armchair nanotubes with

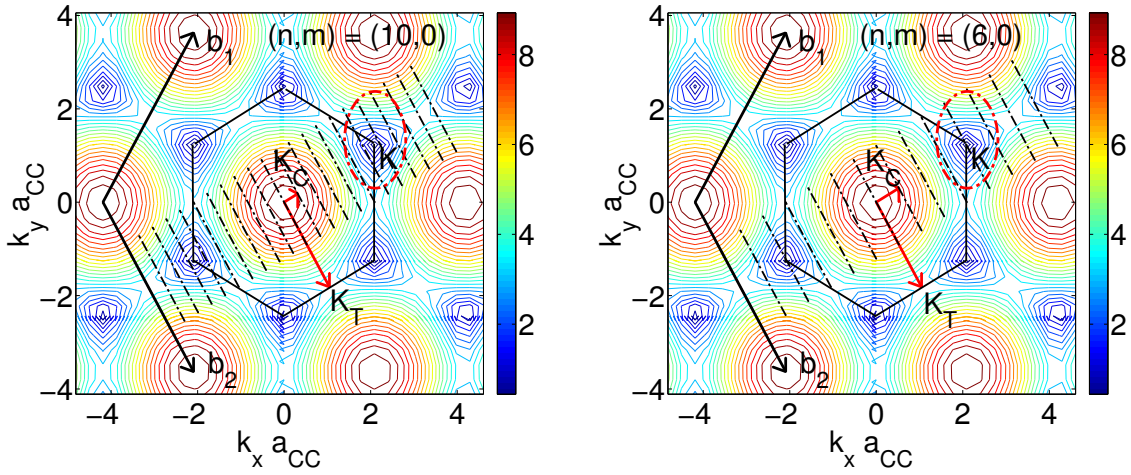

(a) (b) (c) (d)

Figure 4.2: Brillouin zones of nanotubes formed by periodic 1D cuts of graphene's Brillouin zone for nanotubes with indexes (a) $(10,\,0)$, (b) $(6,\,0)$, (c) $(4,\,1)$, (d) $(3,\,3)$. Observe that for metallic tubes, 1D cuts pass through K point and for the semiconductor tube, i.e., $(10,\,0)$, 1D cuts do not pass through K.

$n = m$ (Fig. 4.2(d)) and zigzag nanotubes with $n = 3\,q$ (Fig. 4.2(b)) where q is an integer are metallic. An arbitrary chiral nanotube is metallic if $n - m = 3\,q$ (Fig. 4.2(c)). Furthermore, the semiconducting nanotubes are denoted by type-I and type-II semiconductor for $r = 1$ and $r = 2$, respectively, where $2\,n + m = 3\,q + r$. Based on this derived rule, it is observed that for large values of n, the probability of a nanotube to become metallic

and semiconductor approaches to $1 \, / \, 3$ and $2 \, / \, 3$, respectively.

The carbon nanotube band structure for any chiral nanotube is computed by inserting the 1D wavevectors in (76) into the graphene energy dispersion relation in (42). Metallic and semiconductor behavior of nanotubes can be analyzed based on modeling armchair and zigzag nanotubes in terms of their energy-bands. For armchair nanotubes, (76) can be written as the following,

$$\mathbf{k} = j \, \frac{2 \, \pi \, j}{3 \, a_{CC} \, n} \, \overrightarrow{k_x} + k \, \overrightarrow{k_y} \tag{78}$$

which can be inserted into (42) resulting into the following energy-band dispersion relation for armchair nanotubes,

$$E(j, \, k) = \pm \gamma \sqrt{1 + 4 \cos\left(\frac{j \, \pi}{n}\right) \cos\left(\frac{a_{CC} \, \sqrt{3} \, k}{2}\right) + 4 \cos^2\left(\frac{a_{CC} \, \sqrt{3} \, k}{2}\right)}, \tag{79}$$
$$j = 0, \, 1, \, ..., \, 2 \, n - 1, \; -\frac{\pi}{a \, \sqrt{3}} \leq k \leq \frac{\pi}{a \, \sqrt{3}}$$

The similar analysis can be achieved for zigzag nanotubes leading to the following energy-band dispersion,

$$E(j, \, k) = \pm \gamma \sqrt{1 + 4 \cos\left(\frac{j \, \pi}{n}\right) \cos\left(\frac{a_{CC} \, \sqrt{3} \, k}{2}\right) + 4 \cos^2\left(\frac{a_{CC} \, \sqrt{3} \, k}{2}\right)}, \tag{80}$$
$$j = 0, \, 1, \, ..., \, 2 \, n - 1, \; -\frac{\pi}{a \, \sqrt{3}} \leq k \leq \frac{\pi}{a \, \sqrt{3}}$$

The dispersion relation can be seen in Figs. 4.3(a), (b), (c), (d), (e) and (f) for $(10, \, 0)$ semiconducting zigzag nanotube, $(6, \, 0)$ metallic zigzag nanotube, $(4, \, 1)$ metallic chiral nanotube, $(3, \, 3)$ metallic armchair nanotube, $(10, \, 5)$ type-I semiconducting chiral nanotube and $(10, \, 6)$ type-II semiconducting chiral nanotube, respectively. Observe the metallic nanotubes with degeneracy at either $k = 0$ or $k = 2 \, \pi \, / \, (3 \, |\mathbf{T}|)$.

By analyzing the energy-bands of nanotubes in a tight-binding approximation, the band-gaps of nanotubes are generally and roughly modeled as the following,

$$E_g = 2 \, \gamma \, \frac{a_{CC}}{d_t} \tag{81}$$

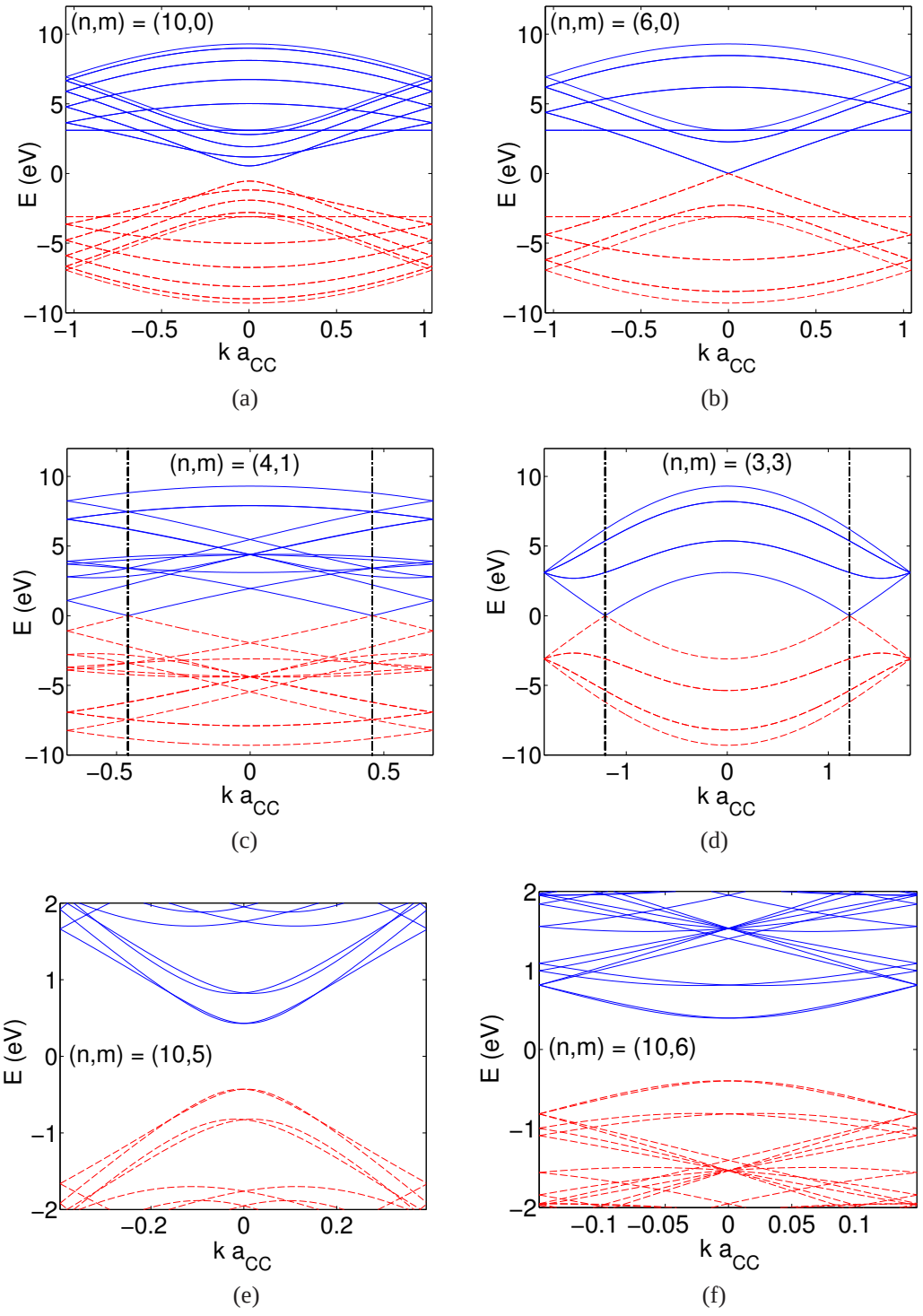

Figure 4.3: Energy-band diagrams for nanotubes with indexes (a) $(10,\,0)$, (b) $(6,\,0)$, (c) $(4,\,1)$, (d) $(3,\,3)$, (d) $(10,\,5)$ and (d) $(10,\,6)$. Observe that for metallic tubes the valence and conduction bands touch each other at $k = 0$ or $k = 2\,\pi\,/\,(3\,|\mathbf{T}|)$.

where the band-gap is inversely proportional to the diameter [184]. However, tight-binding approximation is a limited approximation and there are various effects like electron-hole asymmetries at high energies, σ-bond electrons at high energies, curvature effects in small-diameter nanotubes (which are our main concern in the thesis) and the substrate effects [184].

4.1.1.1 Carbon Nanotube Field Effect Transistors

CNTs as quasi-1D devices show exceptional electron transport properties such as ballistic carrier transport at room temperature and high carrier mobilities. The mobility, i.e, $\nu = v_c / E$, measures the speed of response of the charge carriers to an external electric field where v_c is the carrier velocity and E is the applied electric field. Due to 1D nature of semiconducting nanotubes, which are the main concern in the thesis to be used in a FET geometry as a tunable band-gap photodetector, the mobilities of SWNTs are generally measured based on the analysis of the FET transfer characteristics. The electrical transport properties of carbon nanotubes are generally measured by using the field-effect transistor devices, i.e., CNTFETs, as shown in Fig. 4.4.

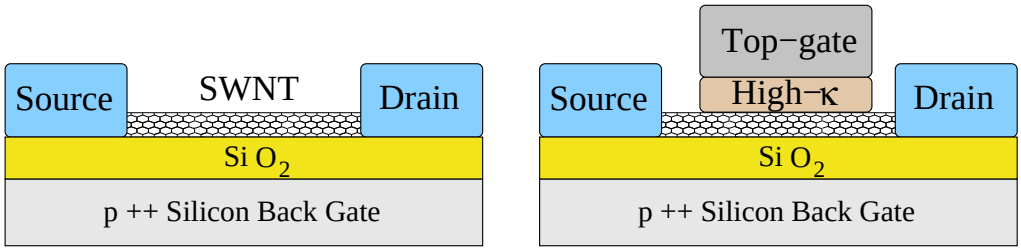

Figure 4.4: CNTFET geometries used for designing transistor, photodetectors and similar devices and also measuring electrical transport and optical properties of nanotubes [78, 184]. The devices are the configurations with (a) single back-gate and (b) double gates of back and top.

A SWNT is connected to two metallic source and drain contacts where the back gate can change the charge density on the tube by switching the device on and off similar to

metal-oxide- semiconductor field-effect transistor (MOSFET) where the channel is the carbon nanotube. Transport measurements include source-drain current (I_{DS}) vs. source-drain (V_{DS}) or gate (V_{GS}) voltage. It is observed that I_{DS} vs. V_{GS} for Fig. 4.4(a) geometry depends on the type of the nanotube [75]. The gate voltage tunes the Fermi level by changing the relative positions of the SWNT bandgap with respect to the Fermi levels of the contacts resulting a large On-Off modulation ratio as shown in Fig. 4.5 for semiconductor nanotubes with large band-gaps. On the other hand, metallic SWNTs and SWNTs with small band-gaps, e.g., curvature induced, and finite constant density of states do not let the On-Off modulation.

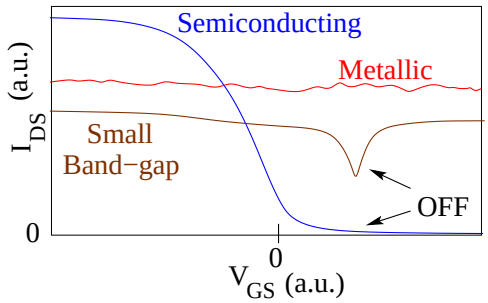

Figure 4.5: The modulation of the FET transistor by gate voltage for three different types of nanotubes [75].

CNTFETs operate such that the gate creates a vertical electric field controlling the amount of charge in the channel whereas a horizontal electric field between the metallic contacts drives the charges from one contact to the other. The types of free carriers in CNTFET devices are either holes (p++) or electrons (n++). If the majority charge carriers are holes (electrons), then the CNTFET is a p-type (n-type) transistor. The charge transport of a CNTFET is determined by the ratio of the length of the nanotube, i.e., L, to the mean free path, i.e., l_m and by the metallic contact with the nanotube.

The type of the contact can be either ohmic, i.e., simple resistive contact permitting carrier injection two-way, or Schottky barrier (SB) contact resulting a barrier for the carriers at

the metal-nanotube junction. On the other hand, if the mean free path is larger than the nanotube length, the charges travel without diffusive scattering leading to the *ballistic* transport of the carriers across the tube. The diffusive scattering is observed for the nanotube length larger than the mean free path.

Ambipolar CNTFET is used to denote the device which can change the majority carrier from holes to electron by changing gate voltages such that it shows symmetric behavior. As shown in Chapter-I while discussing metal-semiconductor-metal Schottky barrier photodiodes, it is shown in (18) that the contact type is determined from the work function difference between the contact metal and the CNT, e.g.,

$$\Phi^{p}_{SB} = \phi_{CNT} + E_g / 2 - \phi_m; \;\; \Phi^{n}_{SB} = \phi_m + E_g / 2 - \phi_{CNT} \tag{82}$$

where E_g is the nanotube band-gap, ϕ_m is the metal work function and ϕ_{CNT} between 4.7-4.9 eV is the work function of carbon nanotube [109].

Similar to the modeling for graphene, in order to measure the high frequency performance of carbon nanotube photodetectors in a transistor configuration, the resistance, carrier velocity and capacitance are modeled next.

4.1.1.2 Resistance Model

The total resistance of a source-nanotube-drain device can be found by summing the contributions coming from the nanotube and the contacts as the following [50],

$$R = R_Q \left(1 + \frac{L}{l_m}\right) + R_c \tag{83}$$

where L is the length of the nanotube, l_m is the mean free path length for scattering, R_c is the part of the contact resistance due to Schottky barriers and contacting geometry, and R_Q is the intrinsic lower limit of the contact resistance given by the Landauer formula,

$$R_Q = \frac{h}{4\,e^2} \approx 6.5\,\mathrm{K}\Omega \tag{84}$$

which is the universal limit for the ballistic transport in a strictly one-dimensional system [13, 75]. In a typical semiconducting CNTFET, the mean free path l_m is around hundreds of nanometers which is larger than the length of the nanotubes with nanometer scales permitting the high mobility ballistic transport across the tube to be used in fast photoconductor applications. Furthermore, the contacts can be realized perfectly close enough to the intrinsic limits of R_Q using the methods like ultrasonic nanowelding method and parallel array of nanotubes [27, 116]. In the diffusive regime, SWNTs are capable of carrying current densities on the order of 10^9 A/cm^2 which is three orders of magnitude larger than copper [32].

4.1.1.3 Carrier Velocity Model

The response speed performance of photodetectors depends on the carrier velocity saturation as discussed in Section-2.4. It determines the speed of propagation of the information for the ideal case of no scattering [184]. The electron group velocity is defined as the following,

$$v_c = \frac{1}{\hbar}\left|\frac{\partial E}{\partial k}\right| \tag{85}$$

The electron-hole symmetry results in the flexibility that the velocities found for electrons can be applied to holes. Fermi velocity, i.e., v_F, is the carrier velocity at the Fermi energy for metallic nanotubes which can be found by finding the derivative of (80) at $j = 2\,n\,/\,3$ and $k = 0$ which gives the following velocity [184],

$$v_F = \frac{3\,a_{CC}\,\gamma}{2\,\hbar} \tag{86}$$

which gives the same Fermi velocity with the graphene, i.e., $\approx 10^6$ m/s for $\gamma \approx 3.1$ eV, which is within factor 2 of common metals, e.g., 1.6×10^6 m/s and 1.4×10^6 m/s for copper and gold, respectively. For semiconducting nanotubes, the carrier velocity at a sub-band index j can be found by using the density of states, i.e., DOS, as the following,

$$v_c = \frac{1}{\hbar}\left|\frac{\partial k}{\partial E}\right|^{-1} = \alpha\,\frac{1}{\hbar\ \pi\ g_s(E,\,j)} \tag{87}$$

where $g_s(E,\, j) \,=\, (\,1\,/\,\pi)\,(\partial k\,/\,\partial E)$ is the general formula for the electron DOS in a semiconducting 1D solid and α equals to 2 for semiconducting nanotubes [184]. The universal semiconducting DOS for lower sub-bands is approximated by the diameter dependent formulation using the DOS of semiconducting zigzag nanotubes as the following,

$$g_s(E,\, j) \;=\; \frac{g_0\,\gamma}{E_{vh2}(j)}\,\frac{|E|}{\sqrt{E^2 \,-\, E^2_{vh1(j)}}} \tag{88}$$

where g_0 is the DOS at the Fermi energy for all metallic zigzag nanotubes given by

$$g_0 \;=\; 8\,/\,3\,a_{CC}\,\pi\,\gamma \;\approx\; 2\,\mathrm{nm}^{-1}\mathrm{eV}^{-1} \tag{89}$$

$E_{vh1}(j)$ and $E_{vh2}(j)$ are the energies of the Van Hove singularity points (VHS) in zigzag nanotubes defining the energy space of the real valued DOS given by the following,

$$E_{vh1}(j) \;\;=\;\; \pm\gamma\left|1 \,+\, 2\cos\left(\frac{j\,\sqrt{3}\,a_{CC}}{d_t}\right)\right| \tag{90}$$

$$E_{vh2}(j) \;\;=\;\; \pm\gamma\left|1 \,-\, 2\cos\left(\frac{j\,\sqrt{3}\,a_{CC}}{d_t}\right)\right| \tag{91}$$

where j is the sub-band index. The energy-band diagram and DOS for nanotube with index $(10, 0)$ are shown in Fig. 4.6. The DOS is found by summing the contributions from each sub-band in (88).

Based on the approximation in (87), the carrier velocity for three sub-bands of interest at the valence band is shown in Fig. 4.7. The zero velocity at the top of the bands results from the mathematical formalism due to continuous modeling where the quantum mechanical discrete nature is violated. Therefore, for semiconducting nanotubes, the Fermi velocity range of order 0.1-1×10^6 m/s is in the achievable range. Furthermore, in a recent experimental study of [94], CNTs contacted by metal electrodes show that the photogenerated charge carriers have average group velocity $0.9 \,\pm\, 0.1 \times 10^6$ m/s leading to ultrafast time response to optical excitations.

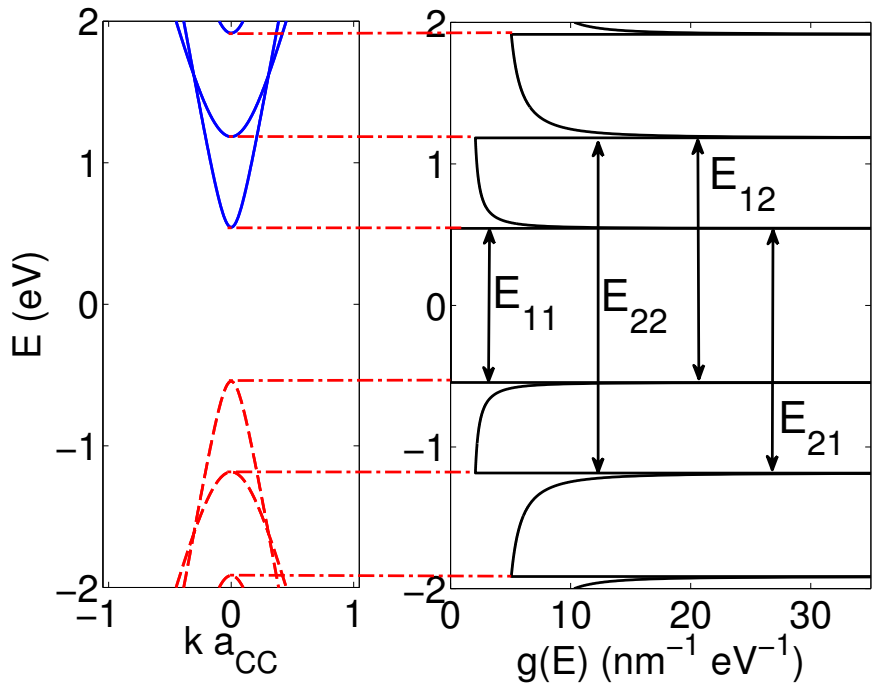

Figure 4.6: The energy-band and DOS relation of semiconducting zigzag nanotube with index $(10, 0)$ [184].

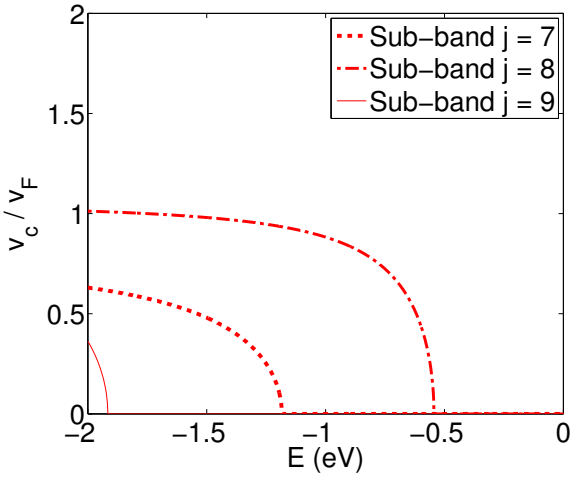

Figure 4.7: The carrier velocity of semiconducting zigzag nanotube with index $(10, 0)$ based on the approximation in (87) [184].

4.1.1.4 Capacitance Model

RC time constant specifies the cut-off frequency performance of a high frequency circuit which is determined by the capacitive elements of circuit. The nanotube transistors are

theoretically modeled by [22] to measure their AC performance characteristics as shown in Fig. 4.8.

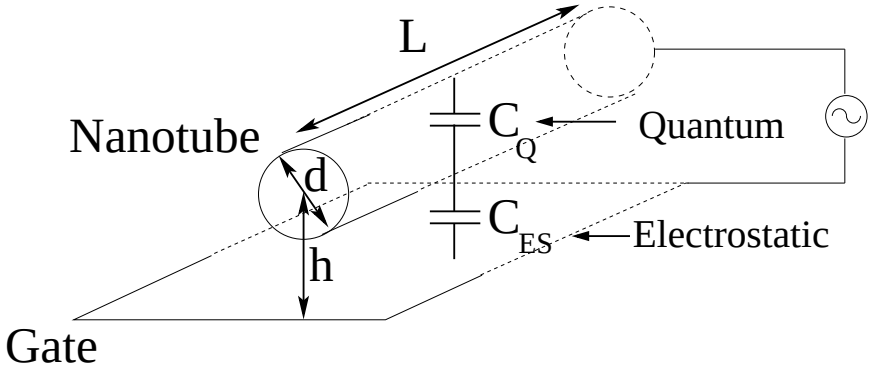

Figure 4.8: The capacitive model of a nanotube within a gate structure of transistors where the total capacitance is the series capacitance of the quantum capacitance (C_Q) of nanotube with electrostatic capacitance (C_{ES}) of nanotube [22, 184].

The total capacitance is the sum of the series capacitances of quantum capacitance C_Q and electrostatic capacitance C_{ES}. The quantum capacitance is previously discussed for graphene and defined in (47) which is due to quantized energy levels having a finite number of states [22, 184].

The quantum capacitance of metallic nanotubes is computed with $C_Q = q^2\, g_0$ as the following [22, 184],

$$C_Q = \frac{8\, q^2}{h\, v_F} = \frac{4\, q^2}{\hbar\, \pi\, v_F} \approx 310\,\text{aF}/\mu\text{m} \tag{92}$$

The semiconducting nanotubes have quantum capacitance changing with the Fermi level which is modulated by gate voltages in a carbon nanotube field effect transistor. Assuming large modulation of Fermi level by back-gate voltages for photodetector applications, it can be observed that small-diameter semiconductor nanotubes give much larger quantum capacitance than the metallic counterparts [101]. Therefore, in cases where the metallic quantum capacitance is large compared with the electrostatic capacitance, the same condition is assumed to hold for the semiconductor nanotube with the same device geometry.

The electrostatic capacitance between a metallic wire of diameter d and a ground plane

at the distance h where the medium between them has dielectric constant of ε can be calculated by the following,

$$C_{ES} \approx \frac{2\,\pi\,\varepsilon}{\ln(h\,/\,d)},\ h > 2\,d \tag{93}$$

C_{ES} is calculated between $\approx$ 89-115 aF/μm for $h = 8$ nm and $\approx$ 33-35 aF/μm for $h = 500$ nm where $\varepsilon = 3.9\varepsilon_0 \approx 0.0345$ aF/nm of SiO_2 and d is between 0.7-1.2 nm. It can be observed that $C_Q \gg C_{ES}$ leading to the negligible quantum capacitance in calculations. It seems that for typical device geometries with $h \gg d$ and small diameter nanotubes, $C_{ES} \approx 30$ aF/μm and it is much larger than the quantum capacitance.

4.1.2 Optical Properties

Semiconducting CNTs are direct band gap materials with diameter tunable optical transition energies which make them potential candidates for optoelectronic applications [8, 10]. The first optical absorption studies were experimented with bulk mixtures of metallic and semiconducting CNTs resulting in broad spectral absorption [10]. Novel optoelectronic applications including electrically driven CNT light emitting and photodetectors are achieved. Ambipolar CNTFETs are used as a gate-controlled and polarized along the axis light emitting source for future photonic and optoelectronic devices [120]. Electroluminescence position on the carbon nanotube field effect transistor can be tuned with gate bias. Furthermore, ambipolar and unipolar carbon nanotube FETs can be used to generate photocurrent and photovoltage [78]. Moreover, significant anisotropic optical absorption of single walled CNTs opens the way for polarization sensitive optoelectronic devices [126].

The photodetectors constructed with semiconductor nanotubes show optical wavelength dependent optical responses. The maximum internal quantum efficiency of photodetectors at their peaks with respect to the optical wavelength is shown to be almost independent of the nanotube radius based on experimental observations performed with nanotube p-n junctions [168]. The peaks are at allowed optical transition energies denoted with E_{ii} where $i = 1, 2, ...$ for light polarization parallel to the nanotube axis and at E_{12}, $E_{2,1}$, ... and

so on (cross-polarized states) for light polarization perpendicular to the nanotube axis as shown in Fig. 4.6 [69]. E_{ii} denotes the energy difference for an optical transition between i'th valence and i'th conduction band within a one-electron picture keeping in mind that the excitonic picture modifies the optical transition energies [42]. Semiconducting CNTs show strong anisotropy for the absorption of polarized light [126] and in this thesis, the incident light is assumed to be polarized parallel to the nanotube axis as shown in Fig. 4.9.

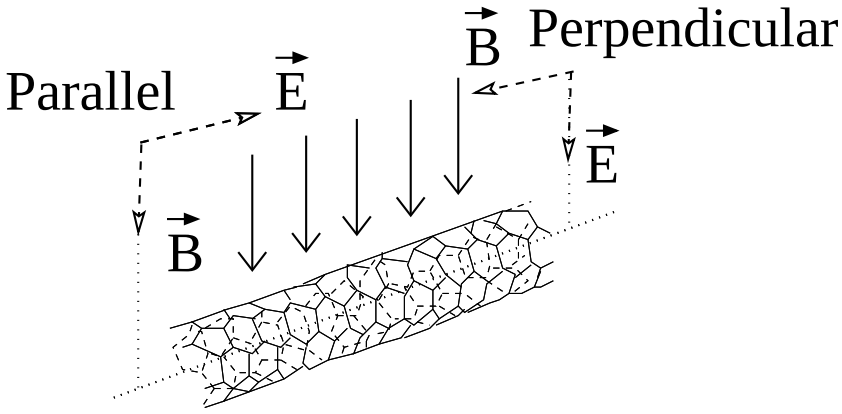

Figure 4.9: The perpendicular and parallel polarized light illumination of a carbon nanotube [96].

The theoretical and experimental studies show that optical transition intensity is concentrated on the excitons rather than the interband transition differently from the conventional semiconductors and the optical transition energies do not directly correspond to the band-gap [150]. Conventional bulk semiconductors like Si and Ge has exciton binding energies, i.e., electron-hole attraction energy, on the order of 10 meV but in SWNTS due to their 1D structure this energy can reach 1 eV making excitonic effects important at room temperature, i.e., E_{11} and E_{22} are directly related to strongly bound excitons [42, 78].

The excitonic states can dissociate forming an unbound e-h pair and contribute the generated photocurrent [87]. Although higher-energy excitons create free e-h pairs by embedding in lower energy states, E_{11} excitons are difficult to dissociate due to large exciton binding energies on the order of several hundreds of meV [8]. In experiments of photocurrent measurement, the photocurrent corresponding to E_{22} is measured in [52, 150]

while corresponding to both E_{11} and E_{22} is measured in suspended double gate SWNT p-n diode [92,93,114], with applied bias field using a displacement photocurrent technique in [121,122] and through the Auger recombination process under an applied high-intensity laser irradiation and low-bias electric field in [86]. Therefore, the photocurrent corresponding to only E_{22} is considered in this thesis. Furthermore, for the diameter range 0.7-1.2 nm of nanotubes, the maximum E_{11} is 1.352 eV and the minimum E_{22} is 1.449 eV as shown in Table 4.2 which is described next. With the assumption of full width at half maximum (FWHM) linewidth of 100 meV, the spectrum region near E_{11} and E_{22} are almost independent. Therefore the optimization framework performed for E_{22} in the next sections can be applied to E_{11} whenever desired.

The nanotube optical transition energy E_{ii} includes contributions from the diameter dependent quantum confinement energy proportional to $i\,/\,dt$, chiral angle dependent trigonal warping perturbation modeled as $\beta_i \cos 3\theta\,/\,d_t^2$ and the excitonic contribution of the many-body effects proportional to $(i\,/d_t)\log(c\,d_t\,/\,i)$ where c is an empirical constant [68]. E_{11} excitons are difficult to dissociate due to large binding energies [8]. Therefore, photocurrent corresponding to E_{22} is considered while the developed framework can be applied to E_{11}. Optical transition frequencies corresponding to $E_{ii} = h\,\nu_{ii}$ vs. d_t is modeled by,

$$E_{ii}(d_t) \;=\; a\,\frac{i}{d_t} \;+\; a\,b\,\frac{i}{d_t}\log(\frac{c}{i\,/\,d_t}) \;+\; \beta_i\,\frac{\cos 3\theta}{d_t^2} \tag{94}$$

where $a = 1.049$ (eV nm), $b = 0.456$, $c = 0.812$ nm^{-1}, $\beta_i = \beta'_{i,p}$ for the tube with index (n,m) where $p = \text{mod}(2n+m,3)$, $\left[\beta'_{1,1}\,\beta'_{1,2}\,\beta'_{2,1}\,\beta'_{2,2}\right] = [0.05\;-0.07\;-0.19\;0.14]$ [78].

These values can be used to form *Kataura plots*, i.e., plots showing the optical transition energies for a diverse set of nanotube types [82], as shown in Fig. 4.10. The specifications of the nanotubes within the diameter range of 0.7-1.2 nm considered in this thesis are shown in Table 4.2 showing their chiral index $(n,\,m)$, diameter d_t, chiral angle θ, β_i values, E_{11}, E_{22} with their corresponding optical transition frequencies and the CNT type.

Experimentally measured spectrum of CNTs and CNT photodetectors are generally fitted by Lorentzian curves for absorption [112,127,130] and for photocurrent [52,150]. In

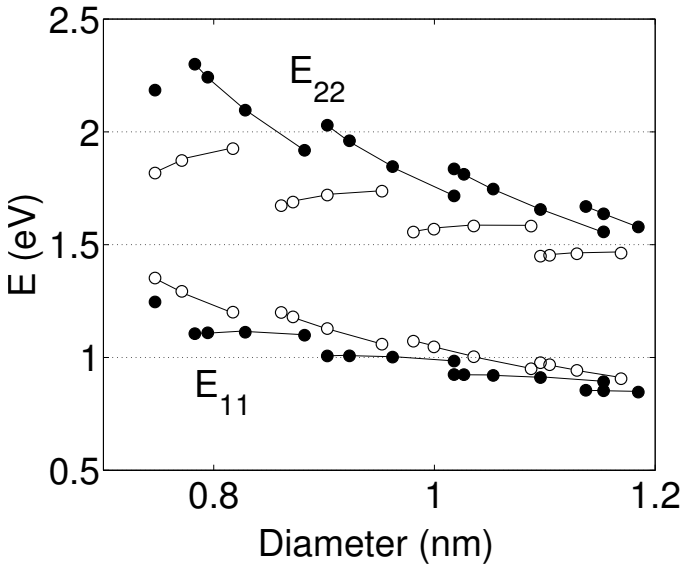

Figure 4.10: The Kataura plot showing the first and second transition energies corresponding to semiconducting small-diameter nanotubes where the open and filled circles correspond to mod$(2\,n\,+\,m,\,3)\,=\,1$ and mod$(2\,n\,+\,m,\,3)\,=\,2$, respectively [78].

this thesis, Lorentzian fitting is used for absorption spectra,

$$\alpha_a(E) = \sum_{i=1}^{2} A_i \frac{\Gamma_{i,a}}{\pi\,\left(\Gamma_{i,a}^2 + (E - E_{ii})^2\right)} \tag{95}$$

where A_i is absorption strength corresponding to the excitation energy E_{ii} , $\Gamma_{i,a}$ is the corresponding linewidth, i.e., full width at half maximum where at the edges it drops the half of the maximum, and $E = h\nu$. $A_i \propto d_t$ in a non-orthogonal tight-binding framework and follows a power law behavior, i.e., $\propto 1\,/\,\sqrt{E_{ii}}$ [146]. Therefore, A_i can be modeled as $A_1 = C_2\,d_t$ and $A_2 = A_1\,\sqrt{E_{11}\,/\,E_{22}}$.

4.2 Introduction to Carbon Nanotube Photodetectors

CNTs are increasingly being used in various CNTFET photodetectors [52, 147, 150, 196], photodiodes [92, 97, 114, 168, 182] or M-SWNT-M devices [26, 29, 30, 65]. CNT devices performing optoelectronic conversion are discussed theoretically and analyzed experimentally in these studies. CNTFETs are utilized as photodetectors converting optical input power to an electrical output signal in [52, 65, 147, 150, 196]. Similarly, photodiode devices

Table 4.2: Optical transition parameters for small diameter (0.7-1.2) (nm) semiconducting SWNTs [78, 82]

n	m	d (nm)	$\theta(^\circ)$	β_1	β_2	E_{11} (eV)	E_{22} (eV)	ν_1 (THz)	ν_2 (THz)	Type
6	5	0.747	26.996	-0.07	0.14	1.246	2.185	301.237	528.248	Chiral
7	5	0.817	24.504	0.05	-0.19	1.2	1.925	290.269	465.55	Chiral
7	6	0.882	27.457	-0.07	0.14	1.099	1.918	265.619	463.856	Chiral
8	3	0.771	15.295	0.05	-0.19	1.293	1.873	312.612	452.81	Chiral
8	4	0.829	19.107	-0.07	0.14	1.112	2.096	268.798	506.801	Chiral
8	6	0.952	25.285	0.05	-0.19	1.059	1.737	256.02	420.035	Chiral
8	7	1.018	27.796	-0.07	0.14	0.984	1.716	237.931	414.967	Chiral
9	1	0.747	5.209	0.05	-0.19	1.352	1.817	326.866	439.414	Chiral
9	2	0.795	9.826	-0.07	0.14	1.109	2.242	268.19	542.098	Chiral
9	4	0.903	17.48	0.05	-0.19	1.128	1.72	272.704	415.844	Chiral
9	5	0.962	20.633	-0.07	0.14	1.001	1.846	242.149	446.371	Chiral
9	7	1.088	25.872	0.05	-0.19	0.95	1.582	229.665	382.592	Chiral
9	8	1.153	28.055	-0.07	0.14	0.892	1.557	215.785	376.363	Chiral
10	0	0.783	0	-0.07	0.14	1.105	2.3	267.307	556.128	Zigzag
10	2	0.872	8.948	0.05	-0.19	1.18	1.689	285.239	408.279	Chiral
10	3	0.923	12.731	-0.07	0.14	1.007	1.96	243.496	474.006	Chiral
10	5	1.036	19.107	0.05	-0.19	1.003	1.583	242.598	382.658	Chiral
10	6	1.096	21.787	-0.07	0.14	0.911	1.656	220.205	400.373	Chiral
11	0	0.861	0	0.05	-0.19	1.199	1.673	289.973	404.532	Zigzag
11	1	0.903	4.307	-0.07	0.14	1.007	2.029	243.425	490.675	Chiral
11	3	1	11.742	0.05	-0.19	1.047	1.569	253.164	379.321	Chiral
11	4	1.053	14.921	-0.07	0.14	0.92	1.746	222.529	422.277	Chiral
11	6	1.169	20.363	0.05	-0.19	0.906	1.463	219.001	353.634	Chiral
12	1	0.981	3.963	0.05	-0.19	1.072	1.556	259.217	376.139	Chiral
12	2	1.027	7.589	-0.07	0.14	0.924	1.812	223.338	438.072	Chiral
12	4	1.129	13.898	0.05	-0.19	0.942	1.46	227.864	352.983	Chiral
12	5	1.185	16.627	-0.07	0.14	0.847	1.578	204.685	381.674	Chiral
13	0	1.018	0	-0.07	0.14	0.924	1.836	223.472	443.885	Zigzag
13	2	1.104	7.053	0.05	-0.19	0.968	1.453	233.958	351.248	Chiral
13	3	1.153	10.158	-0.07	0.14	0.852	1.637	206.111	395.711	Chiral
14	0	1.096	0	0.05	-0.19	0.977	1.449	236.143	350.382	Zigzag
14	1	1.137	3.418	-0.07	0.14	0.855	1.669	206.645	403.572	Chiral

are formed of CNT p-n junctions by means of electrostatic doping using gate voltages in [91–93, 114, 167, 168] or Schottky barrier *metal-single walled carbon nanotube-metal* (M-SWNT-M) CNTFETs [26, 29, 30, 65, 199]. Furthermore, photodiodes by using CNTs are presented in a BFBD device [182] and in a chemically doped p-n device [1]. Photovoltaic cells made of SWNTs obtaining output work power from the incident light are analyzed theoretically and experimentally in [1, 25–27, 45, 91, 97, 99, 182]. In these works,

it is observed that it is possible to obtain efficient photocurrent conversion efficiencies, open circuit voltages and low dark currents making SWNT a candidate optical nanoreceiver. These works are generally experimental and theoretical modeling of the receivers and networking basics are not available.

Photodetectors using CNTs can also be based on thermal detection mechanism in addition to the photon detection devices discussed above. The change in temperature based on illumination using visible or infrared light can be used to generate an electrical response leading to various devices called bolometers and pyroelectric detectors [78]. In this thesis, the photon detectors, i.e., the photocurrent or photovoltage obtained by the photogenerated electrons and holes due to absorbed light on carbon nanotubes, are the main topics of the interest. These devices generates excitons decaying to free electrons and holes which are separated by an external electric field or internal fields at the p-n junctions or Schottky barriers creating a photocurrent or photovoltage response at the external circuit.

Early works on carbon nanotube photoconductivity concentrated on CNTFET photoconductive devices realized in [52, 147, 150, 196] which discuss the dependence of the generated photocurrent on excitation wavelength, power, nanotube type and polarization while considering excitonic effects in detail. Single nanotube ambipolar field effect transistors generated photocurrents and photovoltage in [52] with an internal quantum efficiency of $\%\,10$. The carbon nanotubes produced with laser-ablation method having 1.3 nm diameter are dispersed from a dichloroethane suspension on p++ doped Si wafer coated with 150 nm SiO^2 where the contacts are made from Ti. Photovoltages reaching to 150 mV for incident IR power density of 5 kW/cm^2 were observed. Furthermore, the photocurrent ratio for parallel and perpendicular excitation is found to be bigger than 2. The basic Lorentzian curves for photocurrent vs. photon energy relations are observed based on the experimental results. Photocurrent is observed to depend on incident laser power linearly. A similar device geometry in [150] analyzes the exciton sidebands unique to the CNT optical absorption by measuring E_{22} of individual semiconducting carbon nanotubes. A sideband about 200

meV higher than second excitation energy is observed in the photocurrent spectra due to exciton-phonon coupling. Furthermore, strong depolarization effects are observed on the photocurrent response. These fundamental experimental works present the basic mechanism of CNTFET photodetectors experimentally.

Photodiode devices using CNT p-n junctions with tunable gate voltages are explored in [91–93, 114, 167, 168]. In [167, 168], power efficiency of nanotube p-n junctions under bias is analyzed by using non-equilibrium Green's function (NEGF) formalism where it is observed that $\%\,10$ energy conversion rate is possible for simulations of nanotubes with indexes $(10, 0)$, $(14, 0)$ and $(17, 0)$ and illuminated region of 26.74 nm length. The doping of the tube regions are achieved by insertion of atoms inside the carbon nanotube. The device scheme with the band-bending along the tube is shown in Fig. 4.11(a) and (b). The maximum internal quantum efficiencies of $\%\,16$ for $(17, 0)$ and $(10, 0)$ junctions are observed concluding that the maximum quantum efficiency is independent of nanotube radius and band gap. Furthermore, the CNT p-n junction photodiode is compared with conventional devices such that the maximum responsivity of CNT device is 0.35 A/W where GaAs and InGaAs p-i-n photodiodes have 0.5 A/W and 0.9 A/W, respectively, and quantum dot infrared photodetectors based on InAs/GaAs stacked layers have 0.21 A/W peak responsivities.

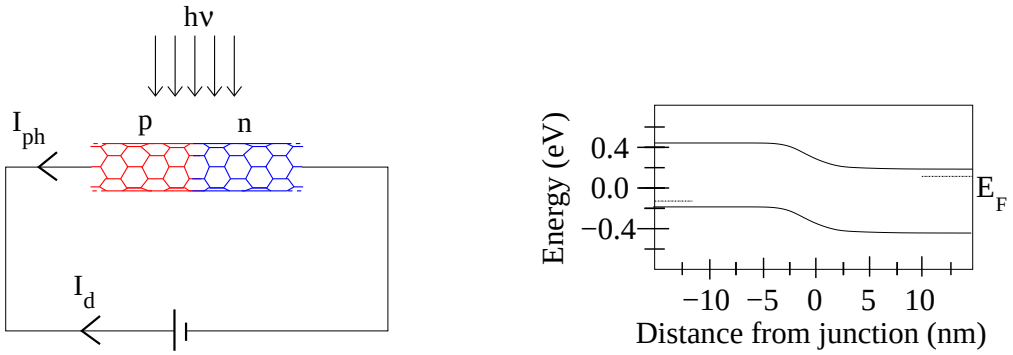

Figure 4.11: (a) Simplified device scheme and (b) energy band diagram of a p-n junction photodiode of doped CNT [168].

On the other hand, in [91–93], electrostatically doped suspended CNT p-n junction diode photocurrent spectroscopy and band-gap are analyzed where doping is achieved by two back-gates. The device geometry and energy-band diagram of devices are shown Fig. 4.12(a) and (b). The studies show that saturation current of p-n junction diodes scales with the band-gap providing a valuable experimental result for modeling leakage current dependence on diameter. Opposite gate polarities V_{G1} and V_{G2} create separate electrostatically n-doped and p-doped regions along the nanotube. SWNT is suspended creating an ideal p-n junction diode.

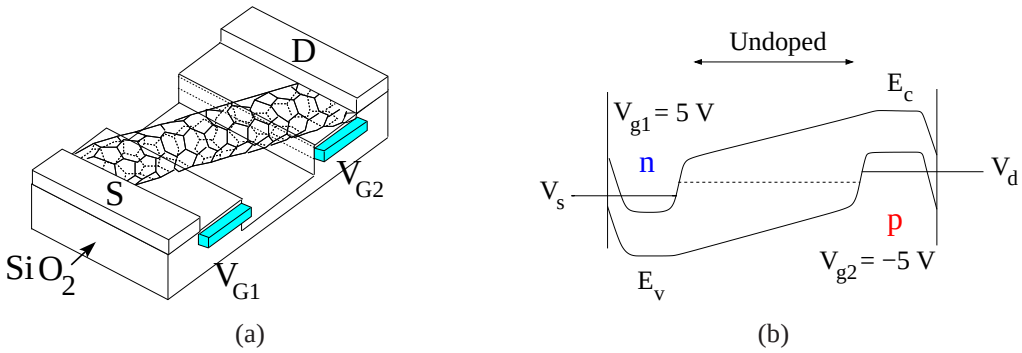

Figure 4.12: (a) Simplified device scheme and (b) energy band diagram of a p-n junction suspended CNT photodiode electrostatically doped with two back gates [91–93].

One of the important type of CNT photodetectors is Schottky barrier CNTFET [26, 29, 30, 199] which forms the main photodetector model used in this thesis. The CNTFET structures with two metallic contacts and the nanotube between them forming Schottky barrier contacts are denoted by Schottky barrier M-SWNT-M carbon nanotube field effect transistors. They are mainly formed by symmetric and asymmetric metal contacts. Furthermore, p-n-p type device geometries are observed in [29, 30]. The symmetric metal device geometry, energy-band diagram, its illustrative I-V plots and the photocurrent vs. dark current relationship for zero source-drain bias are shown in Figs. 4.13(a), (b), (c) and (d), respectively.

As the gate voltage increases, the device behaves more like a diode as can be seen in Fig. 4.13(c). A linear relationship exists for negative gate voltages due to shrinkage of the

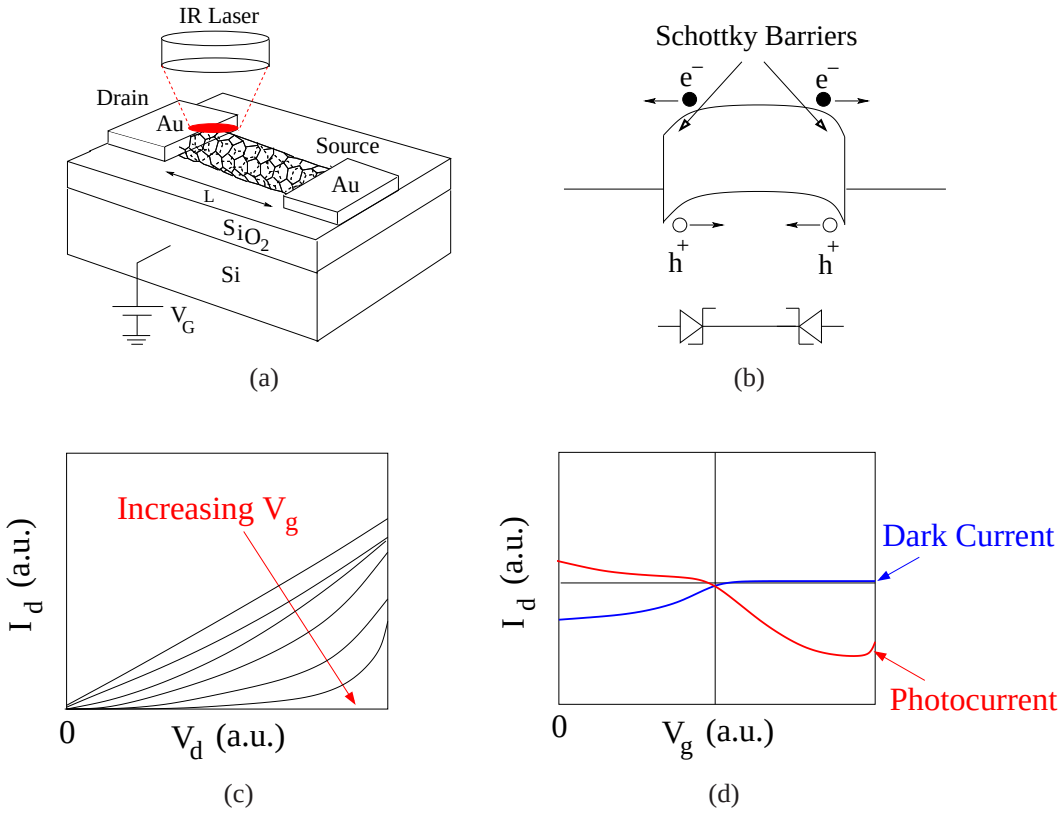

Figure 4.13: (a) Symmetric (Au contacts) M-SWNT-M Schottky barrier CNTFET photodetector (a) device scheme, (b) energy band diagram, (c) I-V characteristics, and (d) photocurrent vs. dark current characteristics at zero source-drain bias [29, 30].

junction where the conductance increases. The conductance decreases with positive gate voltage due to the reduction of the p-doping where CNT in air behaves as a p-type semiconductor channel. The photocurrent to dark current ratio is significantly large at positive voltages where it operates like a reverse biased diode as shown in Fig. 4.13(d). Furthermore, using a lower work function material, e.g., Ag with 4.2-4.5 eV, the photocurrent to dark current ratio and the On-Off diode characteristics are improved since a larger and higher Schottky barrier leads to more diode characteristics.

On the other hand, asymmetric metals, i.e., the main model used in the thesis, bring better improvements by creating a Schottky contact at source with lower work function materials, e.g., Ag, and creating an ohmic contact at the drain with higher or equal work function materials, e.g., Au [30]. The device band diagram, I-V characteristics compared

with symmetric Au-CNT-Au device and the photocurrent vs. dark current characteristics for zero source-drain bias are shown in Figs. 4.14(a), (b) and (c), respectively.

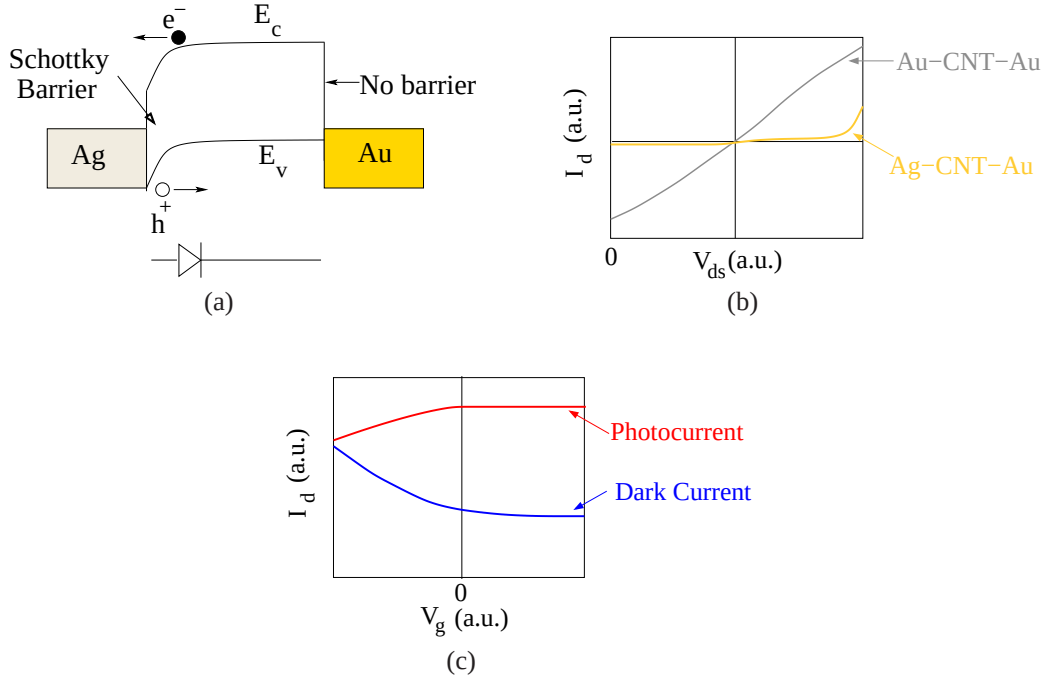

Figure 4.14: (a) Asymmetric (Ag-CNT-Au contacts) M-SWNT-M Schottky barrier CNT-FET photodetector (a) energy band diagram, (b) I-V characteristics, and (c) photocurrent vs. dark current characteristics at zero source-drain bias [30].

This device behaves like a Schottky diode dominated by the Schottky barrier between Ag and nanotube. Au and nanotube interface provides an ohmic contact where the carriers can pass easily. Typical diode characteristic is observed in Fig. 4.14(b). The on-off ratio of the device is found as 10^3 and the open circuit voltage for 50 mW IR radiation is found as 0.45 V which is the highest experimental achievement obtained until today using a single carbon nanotube.

The summary of the CNT photodiode photocurrent and dark current performances compatible with the simplified equivalent circuit of p-n junction photodiodes in Fig. 2.9 and Shockley-diode equation in (16) are given in Table 4.3 such that the typical series resistances, saturation and photo currents, and ideality factors obtained from the plots and measurement results for the experimentally implemented SWNT diodes in the literature are

presented. There is a wide range of experiments showing as much as nA range photocurrents and as low as fA range dark currents, and these studies form the experimental basis of the nanoscale carbon nanotube optical communication architectures.

Table 4.3: Experimental performance of SWNT diodes

n	R_s	R_{sh}	I_s	I_{ph}	Source
1 to 2	20-120 MΩ	-	fA to pA range	-	[114]
-	-	-	$\leq$ 100 fA	fA to pA range	[93]
1.04	-	-	-	fA to nA range	[92]
1	18 MΩ	-	fA to pA range	pA range	[91]
-	-	-	0.5-1.5 pA	15 pA to 1 nA	[30]
-	-	-	$\approx$ 1-50 pA	$\approx$ 180 pA to 10 nA	[199]
1.2	7.9 MΩ	35 GΩ	6.1 pA	2.4 nA to 12.4 nA	[182]
1.03 to 2	9.6-42.5 MΩ	-	$\lesssim$ 5 nA	$\approx$ 2 nA	[1]
4.2 to 13.4	6 MΩ	1.1-9 GΩ	-	$\approx$ 0.5 nA	[97]
1.9	400-640 KΩ	-	1.3 nA	-	[116]
1.2 to 1.5	1-6 MΩ	$\approx$ 1 GΩ	$\leq$ 10 nA	-	[21]

4.3 Carbon Nanotube Wireless Optical Receiver Model

In this thesis, SWNT optical receiver is assumed to be of Schottky barrier CNTFET M-SWNT-M photodiode type with better efficiencies compared with other experiments and as shown in Fig. 4.14 [30]. The physical structure of an asymmetric M-SWNT-M photodiode is shown in Fig. 4.15. It consists of two metals with different work functions connected to SWNT either suspended or on SiO_2 substrate and a Si back-gate managing Schottky barriers.

The characteristics of the devised asymmetric metal Schottky barrier CNTFETs are determined by the Schottky barriers and their behavior changing with respect to the metal types and bias voltages [195]. Actually, the device is the Schottky barrier device introduced in Fig. 2.12 in subsection-2.5.2. SWNTs are p-type devices having holes as the majority when they are exposed to air due to oxygen adsorption [111]. In our networking topologies, the devices are assumed to be in air at room temperature conditions similar to macroscale communication networks. Schottky barrier forms between the low work function metal

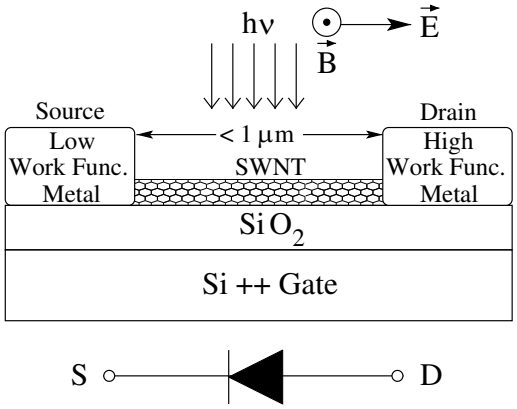

Figure 4.15: Physical structure of an asymmetric M-SWNT-M photodiode where the electric field of the optical signal is polarized along the NT axis [26, 30].

and p-type nanotube. The conduction is dominated by the formed barrier for p carriers at the source [195]. The Schottky diodes have reverse and forward currents due to carriers overcoming the barrier and majority carrier injection from the semiconductor, respectively. If the forward bias is applied, the device shows ohmic conduction almost independent of the substrate bias. For photodiode region of operation, i.e., reverse biased, the energy band diagram of the device is shown in Fig. 4.16 for varying gate voltages.

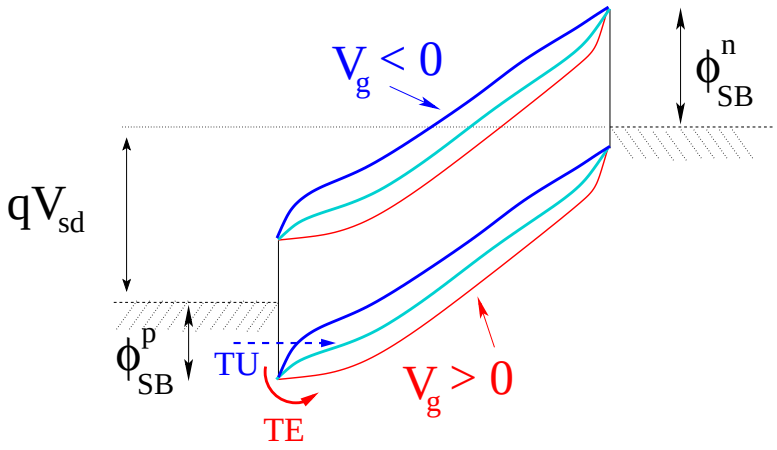

Figure 4.16: The tuning of the operation of reverse biased asymmetric Schottky barrier M-SWNT-M photodetector [111, 195].

Asymmetric thermionic emission (TE) and the symmetric tunneling (TU) are the two major mechanisms for carrier transport through Schottky barrier as discussed previously

in subsection-2.5.2 [111]. The thermionic emission is the responsible mechanism for the rectifying behavior of a diode such that Schottky barrier becomes thick enough allowing only the thermionic emission preventing the tunneling current at the reverse bias conditions of the diode. If the device is negatively back gated, the tunneling current dominates the transport due to decrease in Schottky barrier height and the thickness by making I-V curves more symmetric.

The modulation type is assumed to be of type IM/DD with non-return-to-zero on-off keying similar to the model assumed for graphene photodetectors. Next, the basic CNT optical photodiode receiver is analyzed and modeled in terms of its equivalent circuit, photocurrent and SNR.

4.3.1 Equivalent Circuit Model

Photodiodes are described by their equivalent circuits to model noise sources and cut-off frequency, by evaluating the resistive and capacitive elements of the amplifier and photodiode itself. Then, SNR and R_b, can be evaluated for IM/DD optical channel [79]. In this thesis, M-SWNT-M photodiodes showing diode-like behavior with asymmetrical contacts are used [30]. The reverse bias region is chosen to minimize dark current, i.e., I_d, and maximize photocurrent, i.e., I_p.

CNT photodiode equivalent circuit is given in Fig. 4.17 which is the same with the equivalent circuit model used in Fig. 2.9 for p-n junction photodiodes implying the fact that the MSM transistor behaves like a diode with only one Schottky barrier contact. The model is used for SWNT diode in [116] and p-n junction in [97]. I_p is modeled as a current source parallel to a diode and the shunt (junction) resistance R_{sh}, and in series with resistance R_s of CNT and R_{eq} of CNT and amplifier combination. R_s is the sum of resistances of the contact, i.e., R_c, and nanotube [78, 103]. It changes with tube diameter d_t, contact metals, Schottky barrier height, i.e., Φ_{SB}, and the gate voltage [78, 103, 116]. R_c approaches the quantum limit of $\sim$ 10 KΩ depending on the contact length [103] as

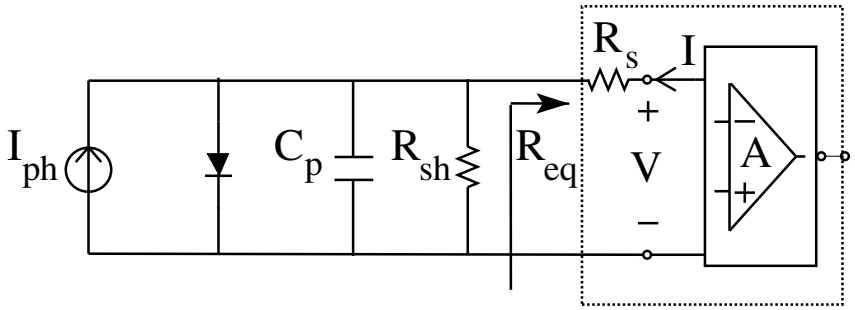

Figure 4.17: Equivalent circuit of a CNT photodiode [97, 116].

discussed in subsection-4.1.1.2. However, more theoretical results are required to model the diameter dependence and out of scope of the thesis. Furthermore, ultrasonic nanowelding method and parallel array of nanotubes decrease R_c [27, 116] substantially. R_s is measured for M-SWNT-M between 400 KΩ and 120 MΩ [97, 114, 116, 182]. R_{sh} which is large compared with R_s is ignored, i.e., 1.1 - 35 GΩ [97, 182]. Various model parameters for CNT photodiodes extracted from the experimental literature work is given previously in Table-4.3.

C_p is the equivalent capacitance found as 30 aF/μm in [116] and in subsection-4.1.1.4, and $\approx$ 50 aF/μm (neglecting the much larger quantum capacitance) [22] leading to THz range cutoff frequency. C_p is $\propto 1/\ln(h_s/d_t)$ as shown in (93) where h_s is the separation between metal plate and the nanotube [22]. For h_s between 8-500 nm, e.g., oxide thickness is 8, 200 and 500 nm in [65], [30] and [182], respectively, C_p ratio of the 0.7 and 1.2 nm diameter tubes is between 0.78-0.92 and their capacitances can be assumed equal. Therefore, C_p is set to 30 aF/μm as in [116].

I_d depends on Φ_{SB} and d_t [114, 116]. If Fermi-level pinning is not taken into account, Schottky barrier height of holes (assuming p-type CNT [111, 116]) at the source is given by (82). I_d is computed by using TE current given in (21) as the following,

$$I_d = D_s \exp\left(-\frac{a_{CC}\,\gamma}{d_t\,\kappa\,T}\right) = D_s \exp\left(-\frac{15.78}{d_t}\right) \tag{96}$$

where $D_s = A\,A^*\,T^2 \exp\left((\Phi_M - \Phi_{CNT}) / \kappa\,T\right)$, κ is the Boltzmann constant, T is the absolute temperature, q is the electric charge, $A^* = (4\,\pi\,q\,m^*\,\kappa^2) / h^3$ is Richardson constant, A is the contact area (assume a constant value for all nanotubes), m^* is CNT effective mass, $a_{CC} = 0.142$ nm is bond length, $\gamma = 2.89$ eV is overlap integral, h is Planck's constant and $E_g = 2\,a_{CC}\,\gamma / d_t$ [78, 103]. Small diameter tubes are chosen for obtaining small I_d.

Shockley diode equation for the circuit shown in Fig. 4.17 is given by (16). In reverse bias of $V < 0$ and $R_{sh} \gg 0$, $I = -I_d - I_p$, i.e., the sum of dark and photocurrent. Next, the diameter dependent photocurrent is modeled.

4.3.2 Photocurrent Model

The channel model is the same with the analysis performed for graphene, i.e., IM/DD optical communication baseband channel and the modeling of the channel and the power loss analysis between transmitter and the receiver are out of scope and a line-of-sight link is assumed [79].

The maximum internal quantum efficiency η_{In} at the wavelength peaks observed in carbon nanotube experiments is almost diameter independent [168]. Semiconducting CNTs show strong absorption anisotropy as discussed previously in subsection-4.1.2 [25], and the incident light is assumed to be polarized parallel as shown in Fig. 4.15. They are direct band gap materials with diameter tunable E_{ii} making them efficient photodevices [8].

Optical transition frequencies corresponding to $E_{ii} = h\,\nu_{ii}$ vs. d_t shown in Fig. 4.18 are modeled by (94) where E_{22} transitions are given the priority in our analyses as discussed before.

Nonequilibrium Green's Function (NEGF) theoretical simulation shows that $\eta_{In} \approx \%\,17$ [168] and $\approx \%\,58.97$ [26] for an asymmetric photovoltaic device. Experimentally, $\eta_{In} > \%\,10$ for SWNT p-n junction [52] and the responsivity $\mathcal{R} = 2 \times 10^{-3}$ A/W [196] make CNT photodiodes very efficient with only a nanometer diameter size for nanoscale

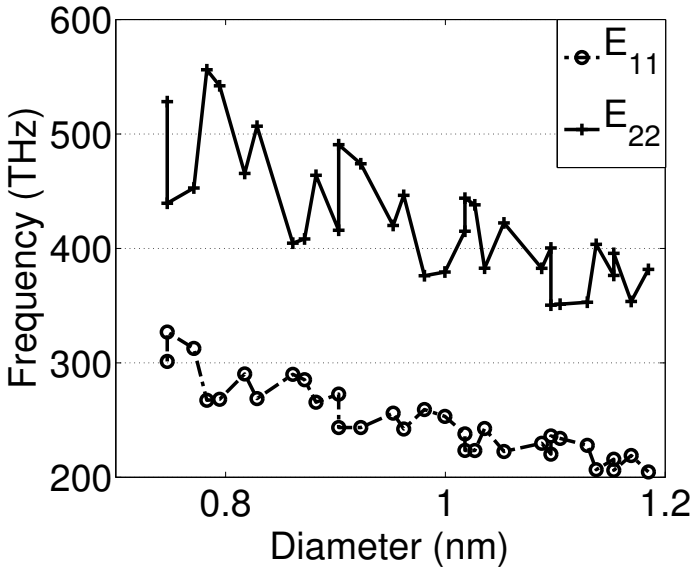

Figure 4.18: Optical transition frequency vs. semiconducting CNT diameter.

optical networks.

Photocurrent should be modeled in terms of ν and d_t dependence to compare different diameter CNTs. Photocurrent spectrum of CNTs are fitted by Lorentzian curves [52, 112, 150] similar to the absorption spectrum modeled in (95).

Furthermore, it can be assumed that $P_a(\nu)$ is linearly proportional to the frequency (ω) dependent imaginary part of SWNT dielectric function ($\varepsilon_i(\omega)$) by treating them as lossy dielectric cylinders [25, 52]. By using $\alpha_a = \varepsilon_i(\omega)\,\omega\,/\,(n_d\,c)$ where n_d is refractive index [155] and c is speed of light and assuming $P_a(\nu)$ depends linearly on d_t^2 [25] and length L, $P_a(\nu)$ can be approximated as,

$$P_a(\nu) = \Upsilon_1 \sqrt{\frac{\nu_{11}}{\nu_{22}}}\, \frac{d_t^3\, L\, P_i(\nu)\, B_l}{\pi\, h^2\, \nu\, \left(B_l^2 \,+\, 4\, \left(\nu - \nu_{22}\right)^2\right)} \tag{97}$$

where $B_l = \Gamma_{2,ph}/h$, Υ_1 is a global normalization constant, $\Gamma_{2,ph}$ is the photocurrent Lorentzian bandwidth with values of 90-100 meV [52, 65, 114, 150]. Therefore, $\Gamma_{2,ph}$ is set to 100 meV. Total photocurrent is given by

$$I_p = \int_{\nu_{min}}^{\nu_{max}} q\, \eta_{In}(\nu)\, \left(P_a(\nu)/(h\nu)\right)\, d\nu \tag{98}$$

where $P_i(\nu)$ (W / Hz) is the transmit optical power density and the total incident power is $P_{tot} = \int_{\nu_{min}}^{\nu_{max}} P_i(\nu)\, d\nu$.

The absorbed power in the frequency interval of ν to $\nu + d\nu$ is $P_a(\nu)\, d\nu$. The normalized absorption spectrum of nanotubes is shown in Fig. 4.19 for the nanotubes with diameters of 0.746, 0.95 and 1.18 nm representing the minimum, average and the maximum diameter tubes for the small diameter range of 0.7-1.2 (nm).

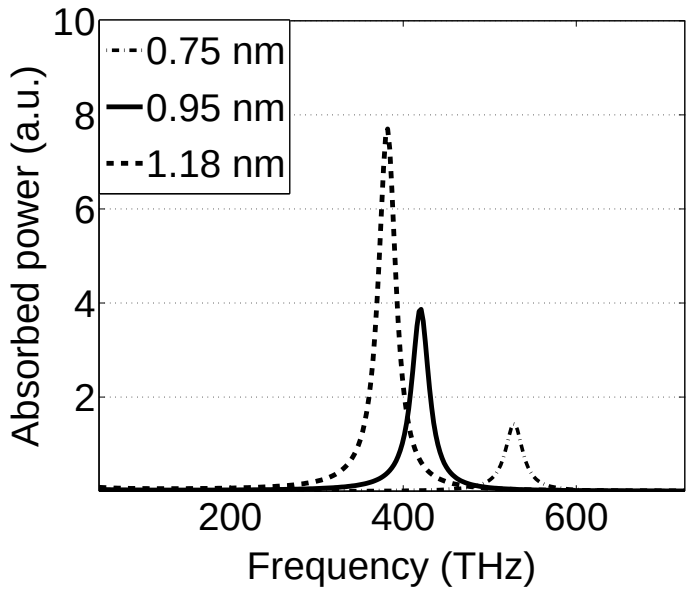

Figure 4.19: The proportional absorbed powers (in arbitrary units) for the nanotubes with minimum, medium and the maximum diameters.

Then, combining with (97), I_p is given by the following,

$$I_p = \Upsilon_2 \sqrt{\frac{\nu_{11}}{\nu_{22}}}\, d_t^3 \int_{\nu_{min}}^{\nu_{max}} \frac{P_i(\nu)}{\nu^2 \left(B_l^2 + 4\,(\nu - \nu_{22})^2\right)}\, d\nu \tag{99}$$

where $B_l = 24.18$ THz, $\Upsilon_2 = \Upsilon_1\, q\, \eta_{In}\, B_l\, L/(\pi\, h^3)$ is a constant. Next, the noise is modeled and SNR is computed.

4.3.3 Noise Model and SNR

The dominant types of photodiode noises discussed previously are valid also for CNT photodetectors which are *thermal noise*, *shot noise* and low frequency $1/f$ noise [76,79]. There

is no theoretical modeling and experimental validation of SNR calculation for an SWNT photodiode.

CNT shot noise depends on *Fano factor*, i.e., $\mathcal{F}$, suppressing the noise compared with the conventional bulk semiconductors [16]. $1/f$ noise is neglected due to the assumption of operating frequencies higher than 1 kHz [76]. The noise spectral densities of thermal and shot noise components can be described by $\sigma_t = 4\,\kappa\,T\,/\,R_{eq}$ where $\kappa = 1.38 \times 10^{-23}$ J/K, $T = 300$ K (room temperature), and $\sigma_{Shot} = \sigma_s + \sigma_d = 2\,q\,I_p + \mathcal{F}\,2\,q\,I_d$ where $0 < \mathcal{F} \leq 1$ and $q = 1.602 \times 10^{-19}$ C. Depending on R_{eq} and the comparison of σ_{Shot} and σ_t, three different noise limited operating regimes are defined as the following,

1. Shot-NL, if $\sigma_t \ll \sigma_{Shot} \approx 2\,q\,I_p$ s.t. $I_p \gg I_d$
2. Dark-NL, if $\sigma_t \ll \sigma_{Shot} \approx \mathcal{F}\,2\,q\,I_d$ s.t. $I_d > I_p$
3. Thermal-NL, if $\sigma_{Shot} \ll \sigma_t$ s.t. $R_s \leq R_{eq}$

Therefore, using I_d and assuming η_{In} is constant, SNR, i.e., $\gamma(d_t) = I_p^2/(\sigma B)$, for the shot, dark and thermal noise limited cases, i.e., γ_s, γ_d and γ_t, respectively, are given by

$$\gamma_s(d_t) = h_s(d_t) \int_{\nu_{min}}^{\nu_{max}} \frac{P_i(\nu)}{\nu^2 \left(B_l^2 + 4\,(\nu - \nu_{22})^2\right)}\,d\nu \tag{100}$$

$$\gamma_{d,t}(d_t) = h_{d,t}(d_t) \left(\int_{\nu_{min}}^{\nu_{max}} \frac{P_i(\nu)}{\nu^2 \left(B_l^2 + 4\,(\nu - \nu_{22})^2\right)}\,d\nu \right)^2 \tag{101}$$

where the subscript s denotes shot noise limited case, subscript (d,t) denotes dark and thermal noise limited cases and

$$h_s(d_t) = \frac{\Upsilon_2}{2\,q\,B}\sqrt{\frac{\nu_{11}}{\nu_{22}}}\,d_t^3 \tag{102}$$

$$h_d(d_t) = \frac{\Upsilon_2^2}{2\,q\,\mathcal{F}\,D_s\,B}\,\frac{\nu_{11}}{\nu_{22}}\,d_t^6 \exp\left(\frac{15.78}{d_t}\right) \tag{103}$$

$$h_t(d_t) = \frac{\Upsilon_2^2}{4\,\kappa\,T\,B}\,\frac{\nu_{11}}{\nu_{22}}\,d_t^6\,R_{eq} \tag{104}$$

Except the shot noise limited case all the SNRs depend on the square of the input power. Next, the modeled SNRs are used in a multi-receiver nanoscale optical network.

4.4 Optical Transmitter Model

In this thesis, theoretically modeled CNT photodetector receivers are based on the experimental works [29, 30, 52, 114, 150, 196, 198] carried out with commercially available transmitting laser sources, i.e., near-IR laser with a wavelength of 830 nm and power of $\approx 6\,\text{W/mm}^2$ with spot size around $200\,\mu$m [30, 198], continuous wave (CW) Ti/Sapphire laser tunable between 780-980 nm [52] and 720-1000 nm [150] with incident power around $10\,\text{W/mm}^2$, Ti/Sapphire laser with spot size of $2\,\mu$m [196]. Furthermore, similar experiments are carried out for graphene photodetectors [188] with Agilent Lightwave Component Analyzers, i.e., N4375B and N4373C, with built-in 1550 nm lasers with the light intensity modulation frequencies available up to 67 GHz.

Although experimentally validated macroscale laser sources can be used to send information to nanoscale receivers, nanoscale optical transmitter devices, e.g., highly efficient light emitting sources using CNT p-n diodes [123], low-power dissipating nanoscale lasers reaching 100 GHz modulations, pW to nW radiation powers and $\approx$ 1nm linewidths at room temperature [47], CNT optical antennas [23, 34, 56], can also be used for designing future nanoscale communication networks where both the transmitter and the receiver are formed of nanoscale devices. However, experimental works obtaining the light modulation of nanoscale transmitters using CNT or other technologies, the detection on CNT receivers for the light generated from these nanoscale light sources and the theoretical modeling of the nanoscale transmitters in terms of power radiation is necessary to formulate the nanoscale transmitter-receiver communication channel. The design of the transmitter and the modeling of the power loss in the channel between receiver and the transmitter are out of scope of the thesis. The receiver model is theoretically developed based on the amount

of the incident power on CNT. Therefore, any transmitter device capable of generating optically modulated line-of-sight incident light density on the order of $0.5\,\text{mW/mm}^2$ or larger can be used as the transmitter unit such that 1 Kb/s or more data rate is possible as will be described in the simulations section.

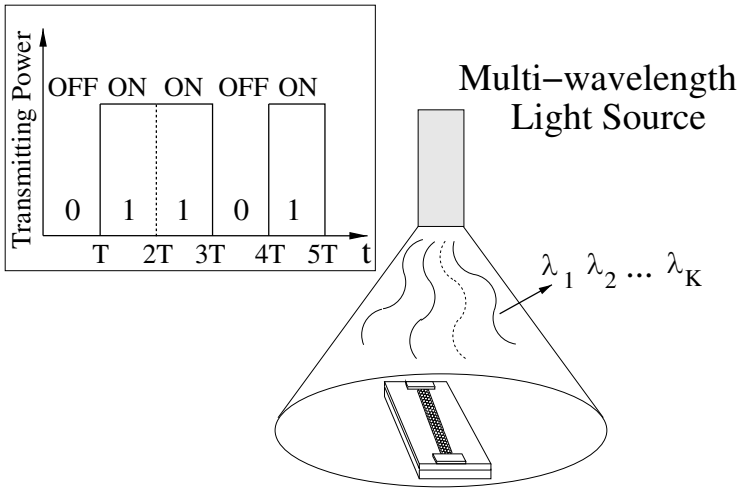

Figure 4.20: Multi-wavelength light source transmitting intensity modulated signal on CNT receiver. The inset shows an illustrative On-Off keyed data pattern modulating the intensity of the light.

Furthermore, the communication medium is the air or free space at room temperature as in experiments forming the basis for the nanoscale receiver models in this thesis [29, 114] and conventional photodetector experiments [79]. Moreover, since CNT receivers are capable of absorbing light on continuous frequency bands with different central frequencies, and broadcast optimization is considered in this thesis, either light sources capable of producing multi-frequency light [176, 179] are needed to broadcast information simultaneously at multiple frequencies or tunable multiple light sources are utilized to broadcast information at various frequencies. However, the physical mechanism and the design of the transmitter light sources are out of scope of the thesis. The transmitter and the receiver network scheme is shown in Fig. 4.20.

4.5 Multiple CNT Receiver Networking Topology

In this thesis, different diameter CNT photodiodes are assumed to form a nanoscale ad-hoc network distributed randomly in a nanoscale communication network topology. Diameter variation is either realized intentionally to form heterogeneous receivers operating at different frequencies or as a result of the synthesis process, e.g., chemical vapor decomposition (CVD) growths nanotubes with Gaussian distributed diameters and uniformly distributed chiral angles [113].

The broadcast channel is important in nanoscale wireless networks where it is difficult to separately interact with individual units in a distributed nanonetwork [2], e.g., to direct the optical power to a single specific CNT receiver. For example, it could be very difficult to find the exact location of the receiver units in a network composed of receivers with different diameter nanotubes and to send specific wavelength light to specific position for a nanotube. Therefore, it is important to introduce and model the broadcast network. The broadcast nanoscale optical network is shown in Fig. 4.21.

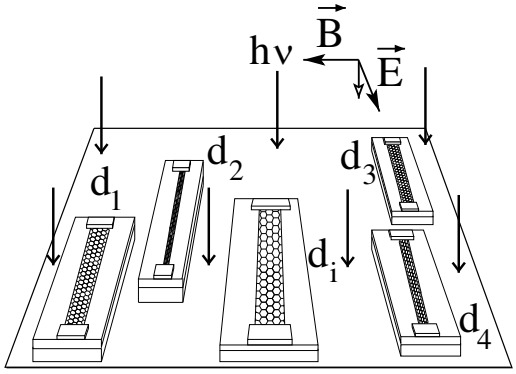

Figure 4.21: Multi-receiver broadcast nanoscale optical network topology of different diameter tubes.

Next, the broadcast power allocation optimization for CNT nanoscale optical network topology is presented.

4.6 SNR Optimization Problem

The broadcast transmission power allocation specifies the minimum SNR of the weakest link determining the maximum data rate in wireless networks [165]. Therefore, in a CNT ad hoc network with a finite amount of transmit power which can occur in future nanoscale optical communication scenarios, it is of uttermost importance to optimize power allocation. This is a *max-min* type optimization and analyzed for wireless networks as a downlink transmit beamforming in [165] and as multicast beamforming in [77].

The transmit optical power is assumed to be constant in finite intervals of frequencies, i.e., $\Delta\nu$, assuming that the total frequency spectrum is divided into intervals of $\Delta\nu$. Therefore, after some manipulations and calculating the indefinite integral, the integral equation for the photocurrent I_p in (100) and (101) can be represented as the following,

$$\int_{\nu_{min}}^{\nu_{max}} \frac{P_i(\nu)}{\nu^2 \left(B_l^2 + 4\,(\nu - \nu_{22})^2\right)}\, d\nu \;=\; \sum_{j\,=\,k_{min}}^{k_{max}} P_i(j\,\Delta\nu)\, f(j, d_t) \tag{105}$$

where $f(j, d_t)$ is the following,

$$f(j,\, d_t) = \frac{1}{j\,(j\,+\,1)\,\Delta\nu\,\left(4\,\nu_{22}^2 + B_l^2\right)} + \frac{4\,\nu_{22}}{\left(4\,\nu_{22}^2 \,+\, B_l^2\right)^2}\,\ln\left(\frac{B_l^2 + 4\,\varsigma^2(j)}{B_l^2 + 4\,\varsigma^2(j+1)}\,\frac{(j+1)^2}{j^2}\right)$$
$$+\,2\,\frac{4\,\nu_{22}^2 \,-\, B_l^2}{B_l(4\,\nu_{22}^2 \,+\, B_l^2)^2}\,\tan^{-1}\left(\frac{2\,\Delta\nu\,B_l}{B_l^2 + 4\,\varsigma(j)\,\varsigma(j+1)}\right) \tag{106}$$

and $\varsigma(j) \,=\, j\,\Delta\nu \,-\, \nu_{22}$. Then, SNR equations in (100) and (101) are transformed to the following,

$$\gamma_s(d_t) = \mathbf{p}^T\,\mathbf{a_s}(d_t);\;\; \gamma_{d,t}(d_t) = \mathbf{p}^T\,\mathbf{A_{d,t}}(d_t)\,\mathbf{p} \tag{107}$$

where

$$\mathbf{A_{d,t}} \equiv h_{d,t}(d_t)\,\mathbf{f}(d_t)\,\mathbf{f}^T(d_t);\;\; \mathbf{a_s} \equiv h_s(d_t)\,\mathbf{f}(d_t) \tag{108}$$

$\mathbf{p} = [P_i\,(k_{min}\,\Delta\nu)\;\ldots P_i\,(k_{max}\,\Delta\nu)]^T$ represents the transmitter power densities at various frequencies and $\mathbf{f}(d_t) = [f(k_{min},\, d_t)\ldots f(k_{max},\, d_t)]^T$.

Then, for the broadcast allocating the transmitter power among K optical frequencies,

the optimization problems maximizing the minimum SNR among N nanotubes in the receiver network can be defined as max-min type problems such that

$$\max_{\mathbf{p}\in\mathbb{R}^{\mathbf{K}}} \min_{i=1,2,...,N} \quad \mathbf{p}^T\,\mathbf{a_s}(d_i) \tag{109}$$

$$\max_{\mathbf{p}\in\mathbb{R}^{\mathbf{K}}} \min_{i=1,2,...,N} \quad \mathbf{p}^T\,\mathbf{A_{d,t}}(d_i)\,\mathbf{p} \tag{110}$$

$$\textbf{s.t.} \quad \mathbf{p}^T\,\mathbf{1} = P_{max},\ \mathbf{p} \geq 0$$

where the subscript s denotes shot noise limited case, subscript (d,t) denotes dark and thermal noise limited cases, respectively, $\mathbf{1_K}$ is the vector of length $K = k_{max} - k_{min} + 1$ (the number of distinct frequencies) with all ones, the total power is restricted to P_{tot} with total maximum density $P_{max} = P_{tot}/\Delta\nu$ and the minimum SNR value among all N nanotubes is maximized with respect to $\mathbf{p}$.

For shot-NL case, (109) is converted the following,

$$\textbf{min}\ \mathbf{c}_{LP}^T\,\mathbf{x}\ \ \textbf{s.t.}\ \ \mathbf{A}_{LP}\,\mathbf{x} = \mathbf{b}_{LP},\ \ \mathbf{x} \geq \mathbf{0}, \tag{111}$$

$$\mathbf{x} = \begin{bmatrix} u \\ \mathbf{p} \\ \mathbf{s} \end{bmatrix},\ \mathbf{A}_{LP} = \left[\begin{array}{c|c|c} & -\mathbf{a_s^T}(d_1) & \\ \mathbf{1_N} & \vdots & \mathbf{I_N} \\ & -\mathbf{a_s^T}(d_N) & \\ \hline & & \\ 0 & \mathbf{1}_\mathbf{K}^T & \mathbf{0}_\mathbf{N}^T \end{array}\right]$$

which is LP type and where $\mathbf{s} = [\,s_1\, s_2 \ldots s_N\,]^T$ is the column vector of slack variables, $\mathbf{c}_{LP} = \left[-1\,\mathbf{0}_\mathbf{K}^T\,\mathbf{0}_\mathbf{N}^T\right]$, $\mathbf{b}_{LP} = \left[\mathbf{0}_\mathbf{N}^T\,P_{max}\right]$ and $\mathbf{I_k}$ is unit vector of size k. (111) is solved with LIPSOL (Linear Interior Point Solver) implemented under MATLAB environment [200].

For dark and thermal-NL cases, (110) is transformed to

$$\max_{\mathbf{p}\in\mathbb{R}^{\mathbf{K}},\,\mathbf{u}\in\mathbb{R}} \ u\ \ \textbf{s.t.}\ \ \mathbf{p}^T\,\mathbf{A_{d,t}}(d_i)\,\mathbf{p} \geq u,\ \mathbf{p}^T\,\mathbf{1} = P_{max} \tag{112}$$

where $\mathbf{p} \geq 0$ and $i \in [1,\, N]$. This problem is a multi-objective extension of Standard Quadratic Problem (StQP) where finding the global solution is NP-hard [138]. However,

Algorithm 1: SDP-BB Algorithm

Solve the SDP relaxation in (113) and obtain $\mathbf{p}^* = ([p_1^* \, p_2^* \, ... \, p_K^*])^T$
Set lower and upper bounds for each p_k, $B_{k,l} = \beta_{k,l} \, p_k^*$, $B_{k,u} = \beta_{k,u} \, p_k^*$
Order p_k from highest to lowest and form $K_{ord} = \{k_1, \, k_2, \, ..., \, k_K\}$
for all $j = 1$ to K **do**
  Solve (114) for each $m \in [1, K_{sub}]$ finding the solution $SDP_{k_j,m}$
  Find $m = m_{k_j}^{max}$ where $SDP_{k_j,m}$ is highest and set $B_{k_j,l}, \, B_{k_j,u}$
end for
Solve the SDP relaxation in (113) with constraints $B_{k,l}, \, B_{k,u}$ and obtain final $\mathbf{p}_{opt}^*$

a bound can be found by using SDP relaxation by converting the problem to the following [138],

$$\begin{aligned} &\max_{\mathbf{p} \in \mathbb{R}^{\mathbf{K}}} \; \min_{i=1,2,...,N} \; \mathrm{Tr}\Big(\mathbf{A_{d,t}}(d_i) \, \mathbf{P}\Big) \\ &\textbf{s.t.} \quad \mathrm{Tr}\Big(\mathbf{E} \, \mathbf{P}\Big) = P_{max}^2, \; \mathbf{p} \geq 0, \; \mathbf{P} = \mathbf{p} \, \mathbf{p}^T \end{aligned} \tag{113}$$

where $\mathbf{E}$ is the matrix of all ones. In a SDP problem, the symmetric structure of $\mathbf{P}$ and $\mathbf{p} \geq 0$ are replaced with constraints $\mathbf{P} \geq 0$ and $\mathbf{P}$ being symmetric positive semidefinite matrix, i.e., $\mathbf{P} \succeq 0$. This problem is solved efficiently in polynomial time using freely available toolboxes implemented in MATLAB, i.e., SeDuMi (IP methods) and CVX (for solving convex problems) [169], [62]. After finding the global solution $\mathbf{P}^*$, the feasible solution $\mathbf{p}^*$ is extracted by $\mathbf{p}_k^* = \alpha \sqrt{\mathbf{P}_{kk}^*}$, $k \in [1, \, K]$, with a scaling variable α to satisfy the total power constraint.

Besides that, *max-min* SNR beamforming frameworks in literature use randomization algorithms to better extract the complex valued solutions after finding the initial SDP relaxation solution $\mathbf{p}^*$ [77, 165]. Since the power is real valued in (112), the randomization algorithms cannot be applied and they are replaced with Branch and Bound search [49] by dividing the hyperplane $\mathbf{p}^T \, \mathbf{1} = P_{max}$ into $K_{sub} = (\beta_{k,u} - \beta_{k,l}) \, p_k^* / \Delta p_k$ regions for each k around the initial SDP bound $\mathbf{p}^*$ for constants K_{sub}, $\beta_{k,l} \leq 1$ and $\beta_{k,u} \geq 1$. K_{sub} increases the solution accuracy. The SDP-BB algorithm is given in Algorithm-1. The indices $k \in [1, \, K]$ are ordered with respect to the values of p_k^* from the highest to the lowest, i.e., $K_{ord} = \{k_1, \, k_2, \, ..., \, k_K\}$, so that firstly the one with the maximum initial power is

searched in order to more quickly converge to the optimum solution. Starting with $k = k_1$, SDP relaxations in (113) are solved with the additional constraint of $S^2_{k,m-1} \leq P_{kk} \leq S^2_{k,m}$ for each $m \in [1, K_{sub}]$ where $S_{k,m} \equiv \beta_{k,l}\, p^*_k \, + \, m\, \Delta p_k$. After finding the maximum SDP bound for p_{k_j}, the corresponding optimum subinterval index ($m^{max}_{k_j}$) is saved to be used in the next coming relaxations of $p_{k_{j+1}}$, $p_{k_{j+2}}$, ..., p_{k_K} for specifying the constraint for p_{k_j}. Therefore, SDP problem for the k_j'th component at the m'th subinterval can be expressed as the following,

$$\begin{aligned} &\max_{\mathbf{P} \succeq 0, \mathbf{P} \succeq 0} \; \min_{i=1,2,...,N} \;\; \mathrm{Tr}\Big(\mathbf{A_{d,t}}(d_i)\, \mathbf{P} \Big) \\ &\textbf{s.t. } \mathrm{Trace}\Big(\mathbf{M}\, \mathbf{P} \Big) \, = \, P_M, \; S^2_{k_j,m-1} \, \leq P_{k_j k_j} \, \leq S^2_{k_j,m} \end{aligned} \tag{114}$$

where $B^2_{k_n,l} \leq P_{k_n k_n} \, \leq \, B^2_{k_n,u}$, $B_{k_n,l} = S_{k_n, m^{max}_{k_n}-1}$, $B_{k_n,u} = S_{k_n, m^{max}_{k_n}}$ and $n \in [1,\, j-1]$. $\mathbf{M}$ can be chosen as either $\mathbf{E}$ or $\mathbf{I}$, i.e., $P_M = P_E = P^2_{max}$ or $P_M = P_I = P_{max}$, choosing the hyperplane or quadratic constraint, respectively. Since the solution is scaled, either of the constraints can be used freely. The resulting K_{sub} bounds are compared and $m^{max}_{k_j}$ giving the highest bound is chosen. Finally (113) is solved with the constraint $B^2_{k,l} \, \leq \, P_{kk} \, \leq B^2_{k,u}$, $k \, \in \, [1, K]$.

4.7 Numerical Simulations and Results

In simulations, it is assumed that the diameter range for the CNT network is ($d_c - \Delta d,\, d_c + \Delta d$) for varying Δd where $d_c \, = \, 0.95$ is chosen as the average of the small diameter range $(0.7\text{-}1.2)$. SDP-BB parameters are chosen as $\beta_{k,l} \, = \, 0.2$ and $\beta_{k,u} \, = \, 4$, and the power is allocated for the spectrum between 300-700 THz with frequency interval of $\Delta\nu \, = \, 10$ THz where the transmitted power is assumed to be constant. The wide spectral region covers absorption range of all the tubes with small diameter range $(0.7,\, 1.2)$, i.e., $\nu^{min}_{22} \, \approx \, 350$ THz and $\nu^{max}_{22} \, \approx \, 550$ THz. The performance of the CNT receivers are simulated assuming the receivers are of the same type with equal device structures but having different diameters.

Firstly, photocurrent and dark current models in (99) and (96) are fit to experimental and theoretical works. Then, cut-off data rates and transmitter power levels are examined. Moreover, SNR and BER characteristics are analyzed for broadcast network and single receiver performance with uniform power allocation. Lastly, uniform and optimum power allocations are compared for varying Δd.

4.7.1 Parameter Fitting for the Proposed Current Models

For numerical calculation of SNR and BER, the diameter dependent photocurent modeling in (99) and dark current in (96) are fit with experimental results and theoretical NEGF formalisms. For the experiments of asymmetrically contacted M-SWNT-M photodetectors, i.e., with Ag/Au [30] and Al/Au source-drain metal contacts [111], with SWNT Schottky barrier contact p-n diode [114] and for the theoretical asymmetrical M-SWNT-M photovoltaic device in [26] (corresponding to E_{11}) with Al/Au metal contacts, the obtained values given in Table 4.4 are used to derive approximate values for D_s and Υ_2 to be used in simulation studies in this thesis.

Table 4.4: Reference M-SWNT-M Device Performances

d (nm)	λ (nm)	P_i (W/mm^2)	I_d (pA)	I_p (nA)	Source
1.4	830	≈ 5.65	0.5	1	[30]
0.9	1127	1	-	0.043	[26]
2.6, 3	-	-	$10,500$	-	[111]

d (nm)	I_d (pA)	Source
$1.5, 1.76, 1.9$	$0.82, 2.92, 7.98$	[114]

D_s and Υ_2 are utilized by assuming the receivers have the same properties, e.g., device geometry, metal types and back gate voltages, but different diameters. By inserting the values in Table 4.4 to (99) and (96), Υ_2 of 0.127 and 0.184 (A THz^4 / nm pW) for [30] and [26], respectively, and D_s of 39.4 nA for [30], between 4.33-96.36 nA for [111] and between 23.15-32.35 nA for [114] are obtained. D_s values of different experiments give results in nA range. Taking the experiment of [30], $D_s = 39.4$ nA and $\Upsilon_2 = 0.127$

(A THz^4 / nm pW) are used in simulations. However, since I_d is very low, I_p needs to be very small to satisfy dark noise limited regime and D_s is chosen larger to get larger SNR, $D_s = 96.36$ nA of [111] is used in this regime. Furthermore, *Fano factor* is set to 1 to realize the worst case dark noise contribution.

4.7.2 Cut-off Data Rate Computation

In this thesis, cut-off rate of CNT detectors are computed by using the experimental measurements of the generated carriers of a recent work in [148] showing picoseconds (ps) time delay in CNT photocurrent measurements. The transit time (t_{tr}) limited bandwidth is found by using the delay of the generated carriers in the nanotube to reach the metallic contacts, i.e., $f_c = 3.5 \,/\, 2\,\pi\, t_{tr}$ [188]. Since the length of nanotubes is $L \leq 1\,\mu$m, the group carrier velocity is $\approx 10^6$ m/s as discussed previously for semiconductor CNTs in subsection-4.1.1.3 and carrier life-time is ≈ 0.25 ns [148], it is computed that $t_{tr} \approx 0.5$ ps and $f_c \approx 1.1$ THz. On the other hand, RC limited bandwidth, i.e., $1 \,/\, 2\,\pi\, R_{eq}\, C_p$, is smaller than THz ranges and determines the resulting bandwidth for the equivalent capacitance $C_p = 30$ aF/μm of the devices. Even the ballistic limit $R_{eq} = 10$ KΩ of nanotubes leads to $f_c = 1 \,/\, 2\,\pi\, R_{eq}\, C_p \approx 0.5$ THz. Therefore, in various noise limited regimes, RC limited bandwidth decides the maximum data rate that the receiver can detect.

4.7.3 Transmitter Power Level

In simulation studies, two types of incident power levels are used. For calculation of the performance of single nanotubes, a wide range of power levels are simulated to observe BER characteristics under very small and very large power levels in the next subsection. On the other hand, for comparison of uniform and optimum power allocation schemes in a broadcast network and for observing the practical broadcast data rates, power transmitted along the linewidth $B_l = 24.18$ THz of a single tube is assumed to be in the experimentally available laser incident power range of 5-10 W/mm^2 [30, 150] for shot and thermal noise limited cases. For dark noise limited case, the maximum power satisfying $I_p \ll I_d$ is

found. In comparing I_p with I_d, and σ_t with σ_{Shot}, 10 times or more larger parameter is assumed to be the dominating one. Assuming that experimental laser incident power density of 5 W/mm^2 is applied at a single frequency for shot and thermal noise limited cases, the total transmitted incident power density, i.e., $P_{tot,0}$, becomes $5 \times (700-300) \,/\, B_l \approx 82.7$ (W / mm^2) where $(700-300) \,/\, B_l$ is used to find the maximum number of absorption windows since each nanotube is assumed to absorb most of the light in B_l linewidth. For dark noise limited case, maximum $P_{tot,0} \approx 171$ (nW / mm^2) incident power satisfies $I_p \ll I_d$ for the nanotubes. It is assumed that broadcast incident power level is $P_{tot,0}$. Therefore, for $P_{tot,0}$ incident power level, the power density per area and per Hz for thermal and shot noise limited cases is given by $P_{dens,0} = 82.7 \,/\, 400 \approx 0.2068$ (pW / mm^2 Hz) and for dark noise limited case $P_{dens,0} \approx 0.2125$ (nW / mm^2 THz).

4.7.4 Uniform Power Allocation BER & SNR Performance

For the power level of $P_{tot,0}$ with uniform power allocation, $R_{eq} \geq 285\,\text{M}\Omega$, $\leq 333\,\text{K}\Omega$ and ≥ 161 TΩ with fixed values along the network result in shot, thermal and dark noise limited cases, respectively, for all the tubes in the diameter range (0.7-1.2) nm. The threshold resistance values are chosen to simulate noise limited types. RC bandwidths of $f_c^{dark} = 32$ Hz, $f_c^{shot} = 18.6$ MHz and $f_c^{therm} = 15.93$ GHz are calculated for these specific resistances. Although $1/f$ noise is high and SNR is very low in dark noise limited case, SNR is calculated to observe the diameter dependence. Next, BER and SNR are computed for both broadcast network and single receivers with uniform power allocation.

4.7.4.1 Broadcast Network

BER of IM/DD non-return-to-zero on-off keying modulation schemes are found by using (38). In Fig. 4.22, the BER of the worst performance tube in the network (all the tubes in the diameter range (0.7-1.2) nm) is shown for varying broadcast data rates R_b and the power level $P_{tot,0}$.

Assuming a BER threshold of 10^{-8} for Mb/s communication, $R_{b,s} < 44.9$ Mb/s and

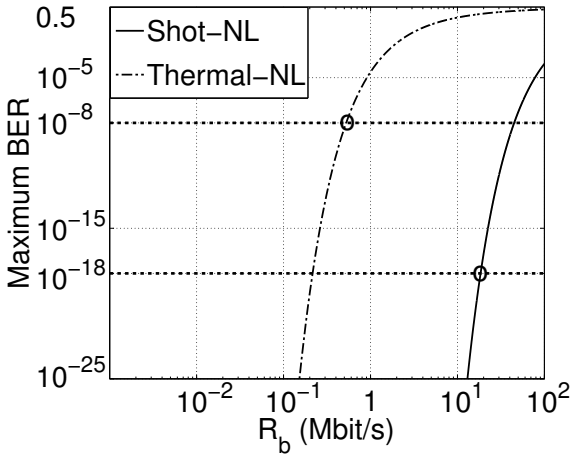

Figure 4.22: BER of the worst performance tube vs. broadcast R_b for uniform power allocation.

$R_{b,t} < 521$ Kb/s are found for shot and thermal noise limited cases, respectively. Since the cut-off frequency is smaller than the computed rate, i.e., $f_{c,1} < 44.9$ Mb/s, the maximum data rate satisfying BER is chosen as $R_{b,1} = f_{c,1} = 18.6$ MHz leading to a maximum BER of $\approx 10^{-18}$. The diameter and chiral angle dependence of SNR for the receivers in the broadcast network are shown in Fig. 4.23(a) and (b).

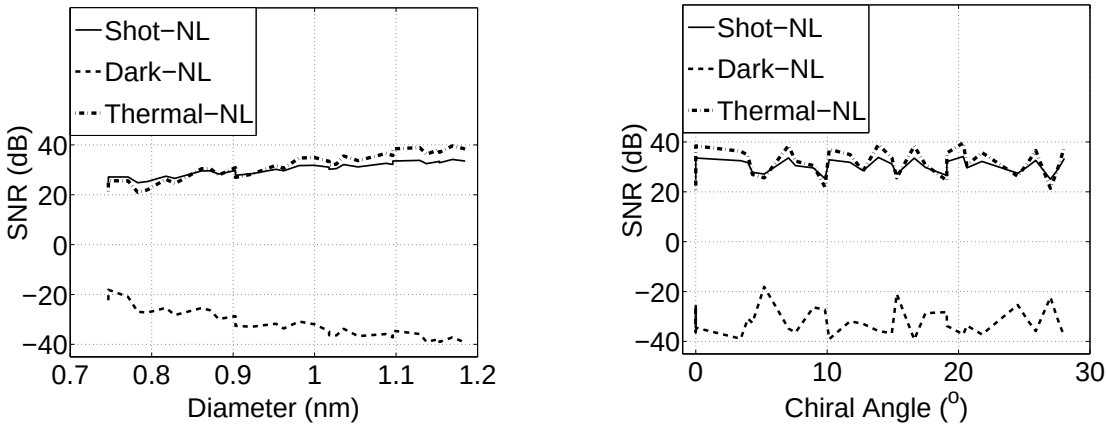

Figure 4.23: SNR vs. (a) the diameter d_t, (b) the chiral angle of single CNT receiver for uniform power allocation.

There is an $\approx 9,\ 18$ and 21 dB difference, i.e., $SNR_r \equiv SNR_{max} \,/\, SNR_{min}$, between the maximum and minimum SNR among the tubes for shot, thermal and dark noise limited

cases, respectively, as the diameter changes. SNR increases with respect to diameter for shot and thermal noise limited cases, and decreases for dark noise limited case. There is not an observable linear dependence on chiral angle. These observations, especially the oscillations prove the distinct nature of nanotubes which are due to the nonuniform optical transition energies, i.e., E_{ii}, with respect to the diameter and its effect in absorption and photocurrent in (97) and (99), and should be tested with experimental works.

4.7.4.2 Single Receiver

The BER of the best performance tube, i.e., minimum BER along the network, is computed without considering noise limited cases but the total receiver noise, i.e., $\sigma_{tot} = \sigma_{Shot} + \sigma_t$, for varying R_b is shown in Fig. 4.24(a) and (b) where tubes are assumed to have adaptive and distinct R_{eq} such that the maximum rates and the BER performances of each tube are computed for a wide range of equivalent resistance values.

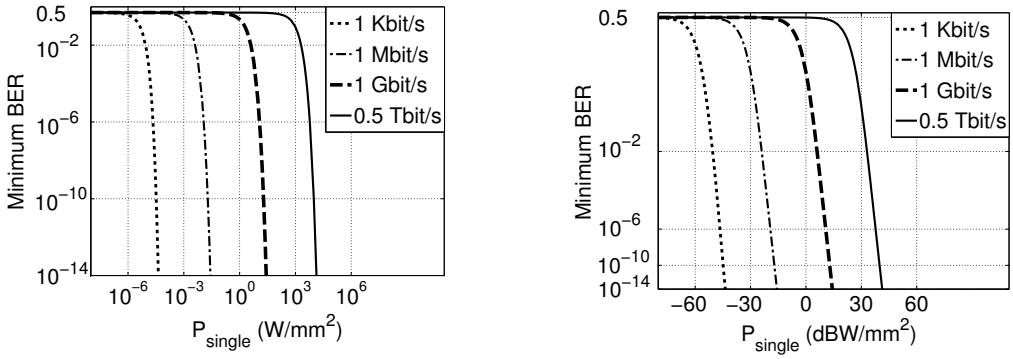

Figure 4.24: Minimum BER among all the tubes vs. P_{single} for varying R_b in (a) logarithmic, (b) double logarithmic (y-axis) plot.

The BER performance is plotted against the absorbed power per nanotube approximating the total absorbed power by finding the total power inside the absorption linewidth B_l, i.e., P_{single}. As the resistance value is lowered the thermal noise component increases lowering the SNR. However, RC limited bandwidth increases allowing higher cut-off data rates. Therefore, the wide range of resistance values are simulated to find the maximum

allowable data rate for a specific power level, BER threshold and for all diameter nanotubes. For various combinations of R_b and power levels, the tube with the minimum BER is chosen.

BER of 10^{-6} is possible even with very low total incident power levels of $P_{single} \approx 20\,\mu$W/mm^2 at the minimum simulated communication rate $R_b = 1$ Kb/s. The maximum R_b is set to ≈ 0.5 THz, since the ballistic limit $R_{eq} = 10$ KΩ leads to $f_c = 1 \,/\, 2\,\pi\, R_{eq}\, C_p \approx 0.5$ THz. It is observed that for 500 Gb/s communication link with BER better than 10^{-14}, the nanotube should be feed with the incident optical power larger than ≈ 15 kW/mm^2 which is out of practical ranges. However, it is possible to achieve hundreds of Mb/s data for tens of W/mm^2 incident power density, e.g., BER of $\approx 10^{-11}$ at $R_b = 1$ Gb/s with power density of ≈ 20 W/mm^2. Next, optimum and uniform power allocations are compared for varying Δd in a broadcast optical nanonetwork.

4.7.5 Optimum vs. Uniform Broadcast Power Allocation

In a broadcast ad hoc network, information is transmitted to a set of nanotubes by distributing the limited total power among the frequency spectrum. Observing the significant SNR difference among tubes, optimization is substantially important for nanoscale optical communication networks. The broadcast power allocation problem could be significantly important in future nanotechnology applications with limited transmitter power and distributed nanodevices where it is difficult to interact with single devices [2].

A fair comparison between optimum and uniform power allocations is achieved by assigning power to the frequency range $(\nu_{22}^{min} - B_l,\, \nu_{22}^{max} + B_l)$ where ν_{22}^{min} and ν_{22}^{max} are the minimum and the maximum optical transition frequencies of the CNT network, respectively, in order to prevent consumption of power in non-absorbing frequency bands in uniform allocation. The incident power density is set to practical level $P_{dens,0}$ for uniform power allocation whereas for optimum power allocation the total power, i.e., $P_{dens,0}\,(\nu_{22}^{min} - B_l,\, \nu_{22}^{max} + B_l)$, is distributed based on the optimization. Furthermore,

R_{eq} is chosen freely (same along the network) by adapting to satisfy the noise limited conditions. BER threshold is set to 10^{-8} assuming Mb/s communication ranges and maximum achievable broadcast R_b along the network is compared for optimum and uniform power allocations, i.e, $G_{opt} = R_b^{opt} / R_b^{uni}$. The rate of the worst performance tube determines the global rate of the network, i.e., R_b. As diameter variation of the network, i.e., Δd increases, the gain increases in an oscillating manner as shown in Fig. 4.25(a) showing that as the difference among the tubes increases, the optimization brings better improvements and between $\approx$ 2-11 dB for various noise limited cases.

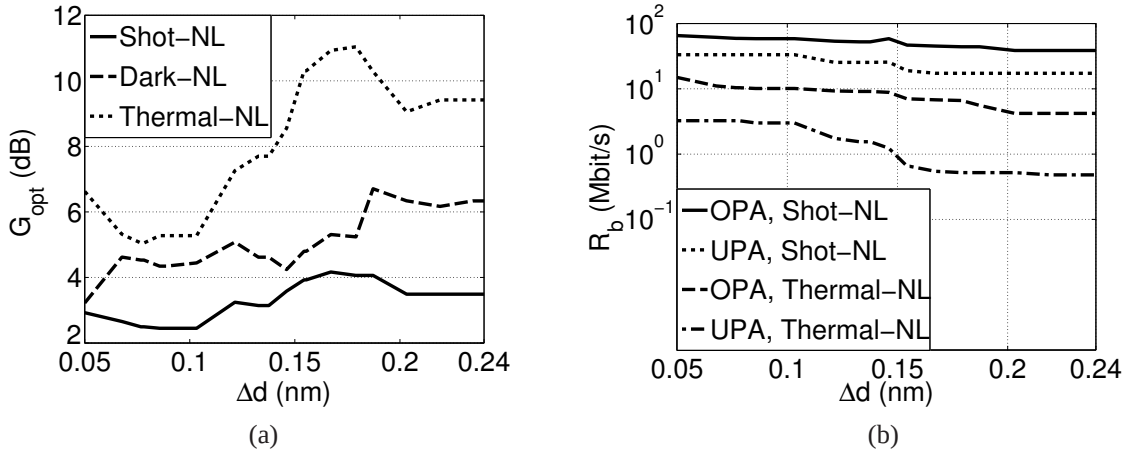

Figure 4.25: (a) G_{opt} vs. Δd for various noise limited cases, (b) R_b vs. Δd for shot and thermal-NL cases for optimum and uniform power allocations.

Furthermore, maximum broadcast R_b at a BER of 10^{-8} is shown in Fig. 4.25(b). All the rates are decreased as Δd increases due to the significant decrease in SNR_{min} as the smaller diameter tubes (for shot and thermal noise limited case) are encountered. However, optimization gives significant improvements where shot noise limited case performs better than thermal noise limited case giving the highest broadcast R_b but the worst gain. It is possible to increase the data rate of the worst receiver in the network by tens of Mb/s by using optimization as shown in 4.25(b) for shot noise limited case. These are the theoretical results which could be developed and modified theoretically with future experimental results.

4.7.5.1 Analysis of Noise Limited Gain Behaviors

The gain behavior of noise limited cases for various diameter sets can be explained as the following. Since SNR $\propto I_p$ for shot noise limited case, SNR $\propto I_p^2 R_{eq}$ and $R_{eq} = 0.1 \times \max\left(4\kappa T / (2q\mathbf{I}_p^{opt})\right)$ for thermal noise limited case, SNR $\propto I_p^2 e^{15.78/d}$ for dark noise limited case where $\mathbf{I}_p$ is the photocurrent vector of the tubes, if R_b is set to the same value for both optimum and uniform power allocations, the gain becomes the ratio of SNR values of the worst performance tubes for optimum and uniform power allocations and can be expressed as the following,

$$G_{opt}^{shot} \propto \frac{\min\left(\mathbf{I}_p^{opt}\right)}{\min\left(\mathbf{I}_p^{uni}\right)} \tag{115}$$

$$G_{opt}^{therm} \propto \frac{\min\left(\mathbf{I}_p^{opt}\right)}{\min\left(\mathbf{I}_p^{uni}\right)} \frac{\max\left(\mathbf{I}_p^{uni}\right) / \min\left(\mathbf{I}_p^{uni}\right)}{\max\left(\mathbf{I}_p^{opt}\right) / \min\left(\mathbf{I}_p^{opt}\right)} \tag{116}$$

$$G_{opt}^{dark} \propto \frac{\min\left((\mathbf{I}_p^{opt})^2 \otimes \mathbf{e}\right)}{\min\left((\mathbf{I}_p^{uni})^2 \otimes \mathbf{e}\right)} \tag{117}$$

where $\mathbf{e} = [e^{15.78/d_1} \ldots e^{15.78/d_N}]$, $\otimes$ and $()^2$ denote the element-wise product and square power, respectively.

In comparison of thermal and shot noise limited cases, it is observed that their optimized power allocations are the same due to the proportionality $\gamma_t(d_t) \propto \gamma_s^2(d_t)$ which can be derived from (100-102) and (104). This leads to the same ratio of min $(\mathbf{I}_p^{opt})$ / min $(\mathbf{I}_p^{uni})$. Furthermore, since optimum power allocation lowers max $(\mathbf{I}_p^{opt})$ / min $(\mathbf{I}_p^{opt})$ and max $(\mathbf{I}_p^{uni})$ / min $(\mathbf{I}_p^{uni}) \propto SNR_r$ gets larger as Δd increases in uniform power allocation as seen in Fig. 4.26, thermal noise limited gain is bigger than shot noise limited gain and gets larger as Δd increases based on (116) and as observed in Fig. 4.25(a). On the other hand, the behavior of the optimization gain for dark noise limited case obeys the proportionality defined in (117) where the diameter of the worst performance tubes changes the gain in an exponential manner. Moreover, as the diameter variation is increased, the SNR ratio between the worst and best performance tubes increases drastically as shown in Fig. 4.26. Since, the effect of diameter on SNR is much more in dark and thermal noise limited cases as shown

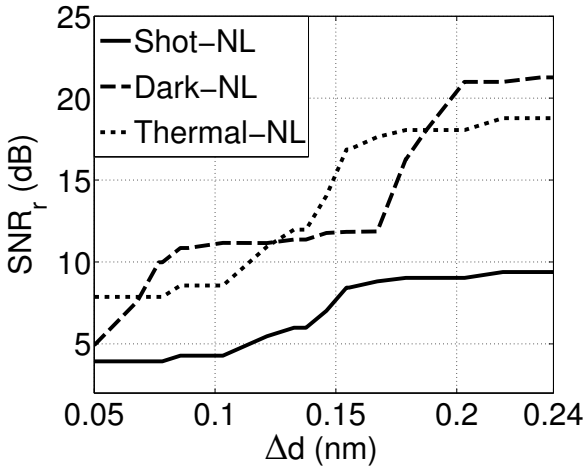

Figure 4.26: SNR_r vs. Δd for uniform power allocation.

in Fig. 4.23(a), SNR_r ratio obeys the same rule such that shot noise limited case has a smaller SNR_r ratio than dark and thermal noise limited cases.

As a summary, CNT nanoscale optical network architecture based on M-SWNT-M photodiodes is presented and analyzed in terms of SNR, BER and R_b. Transmitter power allocation optimization problem is defined and solved for the broadcast network with small diameter nanotubes. The receivers are theoretically modeled emphasizing the diameter dependence in terms of photocurrent and noise for shot, dark and thermal noise limited cases. Information broadcast to multi-user optical CNT receiver network is presented and maximizing the minimum SNR is modeled as a NP-hard max-min quadratic problem in a network of specific diameter range for thermal and dark noise limited cases and as a LP problem for shot noise limited case. SDP relaxation solution is presented within a BB framework. The performance metrics are analyzed for uniform power allocation and IM/DD non-return-to-zero on-off keying modulation for practical transmission powers. Optimum power allocation results in significant performance improvement compared with uniform power allocation in terms of SNR gain and maximum R_b showing an increasing trend with increasing diameter range. The theoretical receiver model is compared with existing experimental results using parameter fitting. Data rates reaching hundreds of Mbit/s are

achievable with very low BERs. Thermal noise limited case gives the highest gain and shot noise limited case gives the highest data rate.

The novel communication theoretical analysis presented for carbon nanotubes combined with the same analysis for graphene photodetectors gives a valuable framework for the next generation nanoscale optical communication architectures by using two rising stars of nanotechnology.

CHAPTER 5

CONCLUSION

Graphene and carbon nanotube with their significant electronic, optical, mechanical and thermal properties are candidates as basic building blocks of the next generation nanoscale optical wireless communication architectures. The communication theoretical analysis of the nanoscale optical receivers built with graphene and carbon nanotube is currently missing in the literature. In this thesis, communication theoretical fundamentals of nanoscale optical wireless communication architectures based on single layer graphene and single walled nanotubes are established.

Not only the great variety of graphene and carbon nanotube photodetectors are introduced by presenting their detailed operation basics but also the different types of photodetectors are classified with respect to their basic layouts. The photo-thermoelectric, symmetric metal and asymmetric metal p-n junctions, multi-layer p-i-n schemes and phototransistors are the observed major types of graphene photodetectors. On the other hand, CNTFET photoconductive devices, CNT p-n junctions with tunable gate voltages, Schottky barrier CNTFET photodiodes are the major types of single walled carbon nanotube photodetectors. The fundamental performance limitations of graphene and carbon nanotubes due to resistance, carrier velocity and capacitive elements are modeled in a detailed manner. Furthermore, optical absorption and tuning properties are examined in coordination with their unique electronic transport properties.

The basic communication theoretical performance metrics, i.e., SNR, BER and data rate, for single layer graphene and single walled carbon nanotube photodetectors are analyzed in a communication theoretical manner. The achievable data rates of the photodetectors are explored from very low transmit power levels to practical and very high laser

power levels. Tens of Gb/s and hundreds of Mb/s data rates for single layer graphene and single walled carbon nanotube, respectively, can be achieved with practical power levels where they are capable of THz range communication intrinsically. The fascinating performance of the photodetectors are promising to open new optoelectonics applications in future nanoscale communication architectures.

Not only the communication theoretical models of the detectors are extracted but also the networking concepts such as diversity combining for multi-receiver graphene photodetectors and broadcast network in a multi-user CNT optical network are introduced by bridging the gap between foundations established upon physical sciences based on quantum mechanical basics with the wireless communication perspective of engineering community. Based upon the presented models in this thesis, more networking analyses and methods can be explored for graphene and carbon nanotube wireless optical communication networks.

To summarize the achievements obtained in this thesis for graphene and carbon nanotube detectors, the following contributions can be listed. For graphene, single-layer symmetric metal-graphene-metal photodetectors are modeled and their SNR, BER and data rate performance metrics for IM/DD non-return-to-zero on-off keying optical modulation are numerically simulated. The shot and thermal noise sources encountered in graphene photodetectors are modeled by defining noise limited operating regimes with respect to the available transmit power levels. It is observed that thermal noise is major source of noise for practical power levels. The achievable data range is found to reach tens of Gb/s with very low BERs which is a significant rate in a nanoscale world with a single layer atomic sheet which can be patterned with respect to the desired size. Besides that, multi-receiver graphene photodetector structures are introduced where classical methods of maximal ratio and equal gain diversity combining schemes are utilized in order to increase the efficiency of the graphene photodetectors. Furthermore, parallel line-scan transmit topology is defined which can be useful in an ad hoc nanoscale network where it is difficult to interact

with particular receivers. The nonuniform SNR observed in a single photodetector in a parallel line-scan transmit topology is improved by homogenizing the output SNR within an optimization approach. The obtained multi-receiver device combines diversity techniques and the optimum placement in order to have spatial channels with more uniform and stronger SNR performance.

On the other hand, the specific results and achievements for CNTs are as the following. The fundamental SNR, BER and data rate metrics of M-SWNT-M asymmetric metal photodiodes is obtained based on the communication theoretical modeling of the basic properties of the detector emphasizing the diameter dependence. Similar to graphene photodetectors, the noise types are modeled for various transmit power levels. It is observed that the communication data rate of hundreds of Mb/s is achievable with very low BERs with practical transmit power levels. The networking concepts are introduced to CNT photodetectors by defining broadcast information for the respective nanoscale network. The transmit power is optimized as a NP-hard max-min quadratic problem to maximize the performance of the worst tube in the network. It is observed that optimum power allocation is significantly superior compared with uniform power allocation due to the high performance differences between nanotubes as much as reaching approximately 20 dB under uniform power allocation.

The future work, especially our ongoing work regarding the graphene photodetectors, is about tuning the absorption optical spectrum by using AB Bernal-stacked bi-layer graphene layers since the band-gap opening is observed for gate modulated bi-layer graphene transistors. The tuning property can be modeled communication theoretically similar to the work achieved in this thesis. Novel multi-color multi-receiver tunable structures can be implemented which can have special place in creating an ultra-wide band tunable photodetector with fast carrier velocity and high quantum efficiency. In a similar manner, graphene nanoribbons are observed to have band-gap and their communication theoretical performances can be analyzed within a tunable detectors concept.

Similar research areas can be explored for multi-color CNT detectors by combining a couple of them. In addition to this, array nanotube structures can be explored since the performance of the detector improves significantly by using carbon nanotube arrays. On the other hand, double walled carbon nanotubes and multi-walled carbon nanotubes can be explored and modeled in terms of photodetection performances.

The fascinating properties of graphene and nanotubes will open new horizons in the future of mankind which is getting more involved in nanoscale science both in terms of technology and the conceptual understanding.

BIBLIOGRAPHY

[1] D. Abdula and M. Shim, "Performance and photovoltaic response of polymer-doped carbon nanotube p-n diodes," *ACS Nano*, vol. 2, no. 10, pp. 2154–2159, 2008.

[2] I. Akyildiz, F. Brunetti, and C. Blázquez, "Nanonetworks: A new communication paradigm," *Computer Networks*, vol. 52, no. 12, pp. 2260–2279, 2008.

[3] I. Akyildiz and J. Jornet, "Electromagnetic wireless nanosensor networks," *Nano Communication Networks*, vol. 1, no. 1, pp. 3–19, 2010.

[4] K. Anstreicher, "Semidefinite programming versus the reformulation-linearization technique for nonconvex quadratically constrained quadratic programming," *J. Global Optim.*, vol. 43, no. 2, pp. 471–484, 2009.

[5] B. Atakan and O. Akan, "Carbon nanotube-based nanoscale ad hoc networks," *IEEE Commun. Mag.*, vol. 48, no. 6, pp. 129–135, 2010.

[6] P. Avouris, "Graphene: Electronic and photonic properties and devices vol. 10, no. 11, pp. 4285–4294, 2010.," *Nano Lett.*, vol. 10, no. 11, pp. 4285–4294, 2010.

[7] P. Avouris, J. Chen, M. Freitag, V. Perebeinos, and J. Tsang, "Carbon nanotube optoelectronics," *Phys. Status Solidi B*, vol. 243, no. 13, pp. 3197–3203, 2006.

[8] P. Avouris, M. Freitag, and V. Perebeinos, "Carbon-nanotube photonics and optoelectronics," *Nat. Photonics*, vol. 2, no. 6, pp. 341–350, 2008.

[9] P. Avouris and R. Martel, "Progress in carbon nanotube electronics and photonics," *MRS Bulletin*, vol. 35, no. 04, pp. 306–313, 2010.

[10] P. Avouris, M. Radosavljević, and S. Wind, *Carbon nanotube electronics and optoelectronics*, ch. 9, pp. 227–251. Springer, 2005.

[11] H. Bach, R. Kunkel, G. Mekonnen, R. Zhang, and D. Schmidt, "100 gb/s photoreceivers for coherent and direct detection," in *Proc. IEEE Optical Fiber Comm. Conf. and Expo. (OFC/NFOEC) and the National Fiber Optic Engineers Conf.*, Los Angeles, USA, March 2011, pp. 1–3.

[12] A. Balandin, S. Ghosh, W. Bao, I. Calizo, D. Teweldebrhan, F. Miao, and C. Lau, "Superior thermal conductivity of single-layer graphene," *Nano Lett.*, vol. 8, no. 3, pp. 902–907, 2008.

[13] P. Bandaru, "Electrical properties and applications of carbon nanotube structures," *J. Nanosci. Nanotechnol*, vol. 7, no. 4-5, pp. 1239–1267, 2007.

[14] Q. Bao, H. Zhang, Y. Wang, Z. Ni, Y. Yan, Z. Shen, K. Loh, and D. Tang, "Atomic-layer graphene as a saturable absorber for ultrafast pulsed lasers," *Advanced Functional Materials*, vol. 19, no. 19, pp. 3077–3083, 2009.

[15] A. Bell, "Selenium and the photophone," *Nature*, vol. 22, pp. 500–503, 1880.

[16] C. Bena, "Effects of decoherence on the shot noise in carbon nanotubes," *Phys. Rev. B*, vol. 81, no. 3, pp. 033404–1–033404–3, 2010.

[17] J. Berashevich and T. Chakraborty, "Tunable band gap and magnetic ordering by adsorption of molecules on graphene," *Phys. Rev. B*, vol. 80, no. 3, pp. 033404–1–033404–4, 2009.

[18] G. F. D. Betta, *Advances in Photodiodes*. Rijeka, Croatia: InTech, 2011.

[19] D. Bitauld, F. Marsili, A. Gaggero, F. Mattioli, R. Leoni, S. Nejad, F. Levy, and A. Fiore, "Nanoscale optical detector with single-photon and multiphoton sensitivity," *Nano Lett.*, vol. 10, no. 8, pp. 2977–2981, 2010.

[20] F. Bonaccorso, Z. Sun, T. Hasan, and A. Ferrari, "Graphene photonics and optoelectronics," *Nat. Photonics*, vol. 4, no. 9, pp. 611–622, 2010.

[21] K. Bosnick, N. Gabor, and P. McEuen, "Transport in carbon nanotube pin diodes," *Appl. Phys. Lett.*, vol. 89, no. 16, pp. 163121–163121, 2006.

[22] P. Burke, "AC performance of nanoelectronics: Towards a ballistic THz nanotube transistor," *Solid-State Electron.*, vol. 48, no. 10-11, pp. 1981–1986, 2004.

[23] P. Burke, S. Li, and Z. Yu, "Quantitative theory of nanowire and nanotube antenna performance," *IEEE Trans. Nanotechnol.*, vol. 5, no. 4, pp. 314–334, 2006.

[24] L. Carloni, P. Pande, and Y. Xie, "Networks-on-chip in emerging interconnect paradigms: Advantages and challenges," in *Proc. ACM/IEEE Int. Symp. on Networks-on-Chip (NOCS)*, San Diego, USA, May 2009, pp. 93–102.

[25] C. Chen, L. Yang, Y. Lu, G. Xiao, and Y. Zhang, "Assessment of optical absorption in carbon nanotube photovoltaic device by electromagnetic theory," *IEEE Trans. Nanotechnol.*, vol. 8, no. 3, pp. 303–314, 2009.

[26] C. Chen, W. Zhang, E. Kong, and Y. Zhang, "Carbon nanotube photovoltaic device with asymmetrical contacts," *Appl. Phys. Lett.*, vol. 94, no. 26, pp. 263501–1–263501–3, 2009.

[27] C. Chen and Y. Zhang, *Nanowelded Carbon Nanotubes: From Field-Effect Transistors to Solar Microcells*. Berlin: Springer Verlag, 2009.

[28] C. Chen, M. Aykol, C. Chang, A. Levi, and S. Cronin, "Graphene-silicon schottky diodes," *Nano Letters*, vol. 11, pp. 1863–1867, 2011.

[29] H. Chen, N. Xi, K. Lai, C. Fung, and R. Yang, "CNT infrared detectors using Schottky barriers and p-n junctions based FETs," in *Proc. IEEE Nanotechnol. Mater. Devices Conf.*, Michigan, USA, 2009, pp. 91–95.

[30] H. Chen, N. Xi, K. Lai, C. Fung, and R. Yang, "Development of infrared detectors using single carbon-nanotube-based field-effect transistors," *IEEE Trans. Nanotechnol.*, vol. 9, no. 5, pp. 582–589, 2010.

[31] P. Chen, S. Chang, S. Ji, S. Lin, H. Lin, H. Tsay, P. Huang, W. Chiang, W. Lin, S. Lee, *et al.*, "Demonstration of 16 channels 10 Gb/s WDM free space transmission over 2.16 km," in *Proc. Digest of the IEEE/LEOS Summer Topical Meetings*, Acapulco, Mexico, July 2008, pp. 235–236.

[32] Y. Chen and M. Fuhrer, "Electric field dependent charge carrier velocity in semiconducting carbon nanotubes," *Phys. Rev. Lett.*, vol. 95, no. 23, p. 236803, 2005.

[33] Z. Chen, J. Appenzeller, J. Knoch, Y. Lin, and P. Avouris, "The role of metal-nanotube contact in the performance of carbon nanotube field-effect transistors," *Nano Lett.*, vol. 5, no. 7, pp. 1497–1502, 2005.

[34] S. Choi and K. Sarabandi, "Performance assessment of bundled carbon nanotube for antenna applications at terahertz frequencies and higher," *IEEE Trans. Antennas Propag.*, vol. 59, no. 99, pp. 802–809, 2011.

[35] E. Ciaramella, Y. Arimoto, G. Contestabile, M. Presi, A. D'Errico, V. Guarino, and M. Matsumoto, "1.28-Tb/s (32×40 Gb/s) free-space optical WDM transmission system," *IEEE Photon. Technol. Lett.*, vol. 21, no. 16, pp. 1121–1123, 2009.

[36] R. Danneau, F. Wu, M. Craciun, S. Russo, M. Tomi, J. Salmilehto, A. Morpurgo, and P. Hakonen, "Shot noise measurements in graphene," *Solid State Commun.*, vol. 149, no. 27-28, pp. 1050–1055, 2009.

[37] S. Datta, *Electronic Transport in Mesoscopic Systems*. Cambridge: Cambridge Univ. Pr., 1997.

[38] S. Datta, *Quantum Transport: Atom to Transistor*. New York: Cambridge Univ. Pr., 2005.

[39] C. Davis and T. Murphy, "Fiber-optic communications [In the Spotlight]," *IEEE Signal Process. Mag.*, vol. 28, no. 4, pp. 152 –150, 2011.

[40] J. Dawlaty, S. Shivaraman, J. Strait, P. George, M. Chandrashekhar, F. Rana, M. Spencer, D. Veksler, and Y. Chen, "Measurement of the optical absorption spectra of epitaxial graphene from terahertz to visible," *Appl. Phys. Lett.*, vol. 93, no. 13, p. 131905, 2008.

[41] D. Decoster and J. Harari, *Optoelectronic Sensors*. London, UK: Wiley-ISTE, 2009.

[42] M. Dresselhaus, G. Dresselhaus, R. Saito, and A. Jorio, "Exciton photophysics of carbon nanotubes," *Annu. Rev. Phys. Chem.*, vol. 58, pp. 719–747, 2007.

[43] S. Dubois, Z. Zanolli, X. Declerck, and J. Charlier, "Electronic properties and quantum transport in graphene-based nanostructures," *The European Physical Journal B-Condensed Matter and Complex Systems*, vol. 72, no. 1, pp. 1–24, 2009.

[44] T. Echtermeyer, L. Britnell, P. Jasnos, A. Lombardo, R. Gorbachev, A. Grigorenko, A. Geim, A. Ferrari, and K. Novoselov, "Strong plasmonic enhancement of photovoltage in graphene," *Nat. Commun*, vol. 2, p. 458, 2011.

[45] K. El Shabrawy, K. Maharatna, and B. Al-Hashimi, "Exploiting SWCNT structural variability towards the development of a photovoltaic device," in *Proc. IEEE 12th Int. Symp. on Integrated Circuits (ISIC)*, Singapore, December 2009, pp. 248–251.

[46] D. Elias, R. Nair, T. Mohiuddin, S. Morozov, P. Blake, M. Halsall, A. Ferrari, D. Boukhvalov, M. Katsnelson, A. Geim, *et al.*, "Control of graphene's properties by reversible hydrogenation: Evidence for graphane," *Science*, vol. 323, no. 5914, p. 610, 2009.

[47] B. Ellis, M. Mayer, G. Shambat, T. Sarmiento, J. Harris, E. Haller, and J. Vučković, "Ultralow-threshold electrically pumped quantum-dot photonic-crystal nanocavity laser," *Nat. Photonics*, vol. 5, no. 5, pp. 297–300, 2011.

[48] T. Fang, A. Konar, H. Xing, and D. Jena, "Carrier statistics and quantum capacitance of graphene sheets and ribbons," *Appl. Phys. Lett.*, vol. 91, no. 9, pp. 092109–1–092109–3, 2007.

[49] C. Floudas, *Nonlinear and Mixed-Integer Optimization*. USA: Oxford University Press, 1995.

[50] A. Franklin and Z. Chen, "Length scaling of carbon nanotube transistors," *Nat. Nanotechnol.*, vol. 5, no. 12, pp. 858–862, 2010.

[51] M. Freitag, "Optical and thermal properties of graphene field-effect transistors," *Phys. Status Solidi B*, vol. 247, no. 11-12, pp. 2895–2903, 2010.

[52] M. Freitag, Y. Martin, J. Misewich, R. Martel, and P. Avouris, "Photoconductivity of single carbon nanotubes," *Nano Lett.*, vol. 3, no. 8, pp. 1067–1071, 2003.

[53] M. Freitag, J. Tsang, A. Bol, D. Yuan, J. Liu, and P. Avouris, "Imaging of the Schottky barriers and charge depletion in carbon nanotube transistors," *Nano Lett.*, vol. 7, no. 7, pp. 2037–2042, 2007.

[54] M. Fuhrer, C. Lau, and A. MacDonald, "Graphene: Materially better carbon," *MRS Bulletin*, vol. 35, no. 04, pp. 289–295, 2010.

[55] H. Fukuyama, K. Sano, K. Murata, H. Kitabayashi, Y. Yamane, T. Enoki, and H. Sugahara, "Photoreceiver module using an InP HEMT transimpedance amplifier for over 40 Gb/s," *IEEE J. Solid-State Circuits*, vol. 39, no. 10, pp. 1690–1696, 2004.

[56] A. Ganguly, K. Chang, S. Deb, P. Pande, B. Belzer, and C. Teuscher, "Scalable hybrid wireless network-on-chip architectures for multi-core systems," *IEEE Trans. Comput.*, vol. 60, pp. 1485–1502, October 2011.

[57] A. Geim and K. Novoselov, "The rise of graphene," *Nat. Mater.*, vol. 6, no. 3, pp. 183–191, 2007.

[58] G. Ghione, *Semiconductor Devices for High-speed Optoelectronics*. Cambridge, UK: Cambridge Univ. Pr., 2009.

[59] G. Giovannetti, P. Khomyakov, G. Brocks, P. Kelly, and J. Van Den Brink, "Substrate-induced band gap in graphene on hexagonal boron nitride: Ab initio density functional calculations," *Phys. Rev. B*, vol. 76, no. 7, p. 073103, 2007.

[60] A. Goldsmith, *Wireless Communications*. New York, USA: Cambridge Univ. Pr., 2005.

[61] J. González, H. Santos, M. Pacheco, L. Chico, and L. Brey, "Electronic transport through bilayer graphene flakes," *Phys. Rev. B*, vol. 81, no. 19, p. 195406, 2010.

[62] M. Grant and S. Boyd, "Cvx: Matlab software for disciplined convex programming, version 1.21." http://cvxr.com/cvx, Apr. 2011.

[63] H. Gu, J. Xu, and Z. Wang, "A novel optical mesh network-on-chip for gigascale systems-on-chip," in *Proc. IEEE Asia Pacific Conf. on Circuits and Systems (APCCAS)*, Macao, November 2008, pp. 1728–1731.

[64] B. Gulbahar and O. Akan, "A communication theoretical modeling of single-walled carbon nanotube optical nanoreceivers and broadcast power allocation," *to appear in IEEE Transactions on Nanotechnology*, 2011.

[65] J. Guo, M. Alam, and Y. Yoon, "Theoretical investigation on photoconductivity of single intrinsic carbon nanotubes," *Appl. Phys. Lett.*, vol. 88, no. 13, pp. 133111–1–133111–3, 2006.

[66] R. Hadfield, "Single-photon detectors for optical quantum information applications," *Nat. Photonics*, vol. 3, no. 12, pp. 696–705, 2009.

[67] M. Han, B. Ozyilmaz, Y. Zhang, and P. Kim, "Energy band-gap engineering of graphene nanoribbons," *Phys. Rev. Lett.*, vol. 98, no. 20, p. 206805, 2007.

[68] E. Haroz, S. Bachilo, R. Weisman, and S. Doorn, "Curvature effects on the E33 and E44 exciton transitions in semiconducting single-walled carbon nanotubes," *Phys. Rev. B*, vol. 77, no. 12, p. 125405, 2008.

[69] Y. Homma, S. Chiashi, and Y. Kobayashi, "Suspended single-wall carbon nanotubes: Synthesis and optical properties," *Reports on Progress in Physics*, vol. 72, no. 6, p. 066502, 2009.

[70] S. Hranilovič, *Wireless Optical Communication Systems*. USA: Springer Verlag, 2005.

[71] S. I. T. Ichihashi, "Single-shell carbon nanotubes of 1-nm diameter," *Nature(London)*, vol. 363, no. 6430, pp. 603–605, 1993.

[72] Y. Ichino, T. Saito, and I. Saito, "Optical trap detector with large acceptance angle," *Journal of Light & Visual Environment*, vol. 32, no. 3, pp. 295–301, 2008.

[73] S. Iijima *et al.*, "Helical microtubules of graphitic carbon," *Nature*, vol. 354, no. 6348, pp. 56–58, 1991.

[74] M. Islam and V. Logeeswaran, "Nanoscale materials and devices for future communication networks," *IEEE Commun. Mag.*, vol. 48, no. 6, pp. 112–120, 2010.

[75] A. Javey and J. Kong, *Carbon Nanotube Electronics*. New York, USA: Springer Verlag, 2009.

[76] S. Jhang, S. Lee, D. Lee, E. Campbell, S. Roth, and Y. Park, "Random telegraph noise in individual single-walled carbon nanotubes," in *Proc. Mater. Res. Soc. Symp.*, vol. 858, Warrendale, US, 2004, pp. 185–190.

[77] M. Jordan, M. Senst, G. Ascheid, and H. Meyr, "Long-term beamforming in single frequency networks using semidefinite relaxation," in *Proc. IEEE VTC 2008-Spring*, Marina Bay, Singapore, May 2008, pp. 275–279.

[78] A. Jorio, G. Dresselhaus, and M. Dresselhaus, *Carbon Nanotubes: Advanced Topics in the Synthesis, Structure, Properties and Applications*. Berlin: Springer Verlag, 2008.

[79] J. Kahn and J. Barry, "Wireless infrared communications," *Proc. IEEE*, vol. 85, no. 2, pp. 265–298, 1997.

[80] J. Kahn, R. You, P. Djahani, A. Weisbin, B. Teik, and A. Tang, "Imaging diversity receivers for high-speed infrared wireless communication," *IEEE Commun. Mag.*, vol. 36, no. 12, pp. 88–94, 1998.

[81] S. Kartalopoulos, *Optical Bit Error Rate: An Estimation Methodology*, vol. 1. NJ, USA: Wiley-IEEE Press, 2004.

[82] H. Kataura, Y. Kumazawa, Y. Maniwa, I. Umezu, S. Suzuki, Y. Ohtsuka, and Y. Achiba, "Optical properties of single-wall carbon nanotubes," *Synthetic Metals*, vol. 103, no. 1-3, pp. 2555–2558, 1999.

[83] K. Kato, S. Hata, K. Kawano, and A. Kozen, "Design of ultrawide-band, high-sensitivity pin photodetectors," *IEICE Tran. on Electronics*, vol. 76, no. 2, pp. 214–214, 1993.

[84] P. Khomyakov, A. Starikov, G. Brocks, and P. Kelly, "Nonlinear screening of charges induced in graphene by metal contacts," *Phys. Rev. B*, vol. 82, no. 11, p. 115437, 2010.

[85] J. Kim, J. Yun, C. Kim, Y. Park, J. Woo, J. Park, J. Lee, J. Yi, and C. Han, "ZnO nanowire-embedded Schottky diode for effective UV detection by the barrier reduction effect," *Nanotechnology*, vol. 21, no. 11, p. 115205, 2010.

[86] S. Konabe, T. Yamamoto, and K. Watanabe, "Auger-recombination Induced photocurrents in single-walled carbon nanotubes," *Appl. Phys. Expr.*, vol. 2, no. 9, p. 092202, 2009.

[87] S. Konabe, T. Yamamoto, and K. Watanabe, "Photocurrents in carbon nanotubes with various diameters under high-intensity laser irradiation," *Jpn. J. Appl. Phys.*, vol. 49, no. 2, pp. 02BD06–1–02BD06–4, 2010.

[88] M. Kotzin and A. van den Heuvel, "A duplex infra-red system for in-building communications," in *Proc. IEEE 36th Vehicular Technology Conf.*, vol. 36, Texas, USA, May 1986, pp. 179–185.

[89] K. Lai, C. Fung, H. Chen, R. Yang, B. Song, and N. Xi, "Fabrication of graphene devices for infrared detection," in *Proc. IEEE Nanotechnology Materials and Devices Conf. (NMDC)*, Monterey, CA, October 2010, pp. 14–17.

[90] E. Lee, K. Balasubramanian, R. Weitz, M. Burghard, and K. Kern, "Contact and edge effects in graphene devices," *Nat. Nanotechnol.*, vol. 3, no. 8, pp. 486–490, 2008.

[91] J. Lee, "Photovoltaic effect in ideal carbon nanotube diodes," *Appl. Phys. Lett.*, vol. 87, no. 7, pp. 073101–1–073101–3, 2005.

[92] J. Lee, "Band-gap renormalization in carbon nanotubes: Origin of the ideal diode behavior in carbon nanotube p-n structures," *Phys. Rev. B*, vol. 75, no. 7, pp. 075409–1–075409–5, 2007.

[93] J. Lee, P. Codella, and M. Pietrzykowski, "Direct probe of excitonic and continuum transitions in the photocurrent spectroscopy of individual carbon nanotube p-n diodes," *Appl. Phys. Lett.*, vol. 90, no. 5, pp. 053103–1–053103–3, 2007.

[94] W. Lee, J. Park, S. Sim, S. Jo, K. Kim, B. Hong, and K. Cho, "Transparent flexible organic transistors based on monolayer graphene electrodes on plastic," *Advanced Materials*, vol. 23, no. 15, pp. 1752–1752, 2011.

[95] M. Lemme, F. Koppens, A. Falk, M. Rudner, H. Park, L. Levitov, and C. Marcus, "Local on-off control of a graphene p-n photodetector," *Arxiv preprint arXiv:1012.4745*, 2010.

[96] F. Léonard, *The Physics of Carbon Nanotube Devices*. New York, USA: William Andrew Pub., 2008.

[97] H. Li, W. Loke, Q. Zhang, and S. Yoon, "Physical device modeling of carbon nanotube/GaAs photovoltaic cells," *Appl. Phys. Lett.*, vol. 96, no. 4, pp. 043501–1–043501–3, 2010.

[98] H. Li, Q. Zhang, and N. Marzari, "Unique carbon-nanotube field-effect transistors with asymmetric source and drain contacts," *Nano Lett.*, vol. 8, no. 1, pp. 64–68, 2008.

[99] Z. Li, V. Kunets, V. Saini, Y. Xu, E. Dervishi, G. Salamo, A. Biris, and A. Biris, "Light-harvesting using high density p-type single wall carbon nanotube/n-type silicon heterojunctions," *ACS Nano*, vol. 3, no. 6, pp. 1407–1414, 2009.

[100] Z. Li, E. Henriksen, Z. Jiang, Z. Hao, M. Martin, P. Kim, H. Stormer, and D. Basov, "Dirac charge dynamics in graphene by infrared spectroscopy," *Nature Physics*, vol. 4, no. 7, pp. 532–535, 2008.

[101] J. Liang, D. Akinwande, and H. Wong, "Carrier density and quantum capacitance for semiconducting carbon nanotubes," *Journal of Applied Physics*, vol. 104, no. 6, pp. 064515–064515, 2008.

[102] L. Liao, Y. Lin, M. Bao, R. Cheng, J. Bai, Y. Liu, Y. Qu, K. Wang, Y. Huang, and X. Duan, "High-speed graphene transistors with a self-aligned nanowire gate," *Nature*, vol. 467, no. 7313, pp. 305–308, 2010.

[103] S. Lim, J. Jang, D. Bae, G. Han, S. Lee, I. Yeo, and Y. Lee, "Contact resistance between metal and carbon nanotube interconnects: Effect of work function and wettability," *Appl. Phys. Lett.*, vol. 95, pp. 264103–1–264103–3, 2009.

[104] L. Lin, C. Wang, M. Hegg, and L. Huang, "Quantum dot nanophotonics-from waveguiding to integration," *Journal of Nanophotonics*, vol. 3, no. 1, p. 031603, 2009.

[105] Y. Lin, C. Dimitrakopoulos, K. Jenkins, D. Farmer, H. Chiu, A. Grill, and P. Avouris, "100-GHz transistors from wafer-scale epitaxial graphene," *Science*, vol. 327, no. 5966, p. 662, 2010.

[106] G. Liu, W. Stillman, S. Rumyantsev, Q. Shao, M. Shur, and A. Balandin, "Low-frequency electronic noise in the double-gate single-layer graphene transistors," *Appl. Phys. Lett.*, vol. 95, no. 3, pp. 033103–1–033103–3, 2009.

[107] J. Liu, *Photonic Devices*. Cambridge, UK: Cambridge Univ. Pr., 2005.

[108] L. Liu and Z. Shen, "Bandgap engineering of graphene: A density functional theory study," *Appl. Phys. Lett.*, vol. 95, no. 25, pp. 252104–1–252104–3, 2009.

[109] P. Liu, Q. Sun, F. Zhu, K. Liu, K. Jiang, L. Liu, Q. Li, and S. Fan, "Measuring the work function of carbon nanotubes with thermionic method," *Nano Lett.*, vol. 8, no. 2, pp. 647–651, 2008.

[110] A. Loiseau, *Understanding Carbon Nanotubes: From Basics to Applications*, vol. 677. Berlin: Springer Verlag, 2006.

[111] C. Lu, L. An, Q. Fu, J. Liu, H. Zhang, and J. Murduck, "Schottky diodes from asymmetric metal-nanotube contacts," *Appl. Phys. Lett.*, vol. 88, no. 13, pp. 133501–1–133501–3, 2006.

[112] Z. Luo, L. Pfefferle, G. Haller, and F. Papadimitrakopoulos, "(n, m) abundance evaluation of single-walled carbon nanotubes by fluorescence and absorption spectroscopy," *J. Am. Chem. Soc.*, vol. 128, no. 48, pp. 15511–15516, 2006.

[113] S. Magazine, "Modeling SWCNT bandgap and effective mass variation using a Monte Carlo approach," *IEEE Trans. on Nanotechnol.*, vol. 9, no. 2, pp. 184–193, 2010.

[114] A. Malapanis, D. Jones, E. Comfort, and J. Lee, "Measuring carbon nanotube band gaps through leakage current and excitonic transitions of nanotube diode," *Nano Lett.*, vol. 11, no. 5, pp. 1946–1951, 2011.

[115] L. Mandalapu, F. Xiu, Z. Yang, and J. Liu, "Al/Ti contacts to Sb-doped p-type ZnO," *Journal of Applied Physics*, vol. 102, no. 2, pp. 023716–1–023716–5, 2007.

[116] H. Manohara, E. Wong, E. Schlecht, B. Hunt, and P. Siegel, "Carbon nanotube Schottky diodes using Ti-Schottky and Pt-Ohmic contacts for high frequency applications," *Nano Lett.*, vol. 5, no. 7, pp. 1469–1474, 2005.

[117] J. Martinez-Duart, R. Martín-Palma, and F. Agulló-Rueda, *Nanotechnology for Microelectronics and Optoelectronics*. Great Britain: Elsevier Science, 2006.

[118] I. Meric, M. Han, A. Young, B. Ozyilmaz, P. Kim, and K. Shepard, "Current saturation in zero-bandgap, top-gated graphene field-effect transistors," *Nat. Nanotechnol.*, vol. 3, no. 11, pp. 654–659, 2008.

[119] H. Michaelson, "The work function of the elements and its periodicity," *Journal of Applied Physics*, vol. 48, no. 11, pp. 4729–4733, 1977.

[120] J. Misewich, R. Martel, P. Avouris, J. Tsang, S. Heinze, and J. Tersoff, "Electrically induced optical emission from a carbon nanotube FET," *Science*, vol. 300, no. 5620, p. 783, 2003.

[121] A. Mohite, J. Lin, G. Sumanasekera, and B. Alphenaar, "Field-enhanced photocurrent spectroscopy of excitonic states in single-wall carbon nanotubes," *Nano Lett.*, vol. 6, no. 7, pp. 1369–1373, 2006.

[122] A. Mohite, P. Gopinath, H. Shah, and B. Alphenaar, "Exciton dissociation and Stark effect in the carbon nanotube photocurrent spectrum," *Nano Lett.*, vol. 8, no. 1, pp. 142–146, 2008.

[123] T. Mueller, M. Kinoshita, M. Steiner, V. Perebeinos, A. Bol, D. Farmer, and P. Avouris, "Efficient narrow-band light emission from a single carbon nanotube p–n diode," *Nat. Nanotechnol.*, vol. 5, no. 1, pp. 27–31, 2009.

[124] T. Mueller, F. Xia, and P. Avouris, "Graphene photodetectors for high-speed optical communications," *Nat. Photonics*, vol. 4, no. 5, pp. 297–301, 2010.

[125] T. Mueller, F. Xia, M. Freitag, J. Tsang, and P. Avouris, "Role of contacts in graphene transistors: A scanning photocurrent study," *Phys. Rev. B*, vol. 79, no. 24, p. 245430, 2009.

[126] Y. Murakami, E. Einarsson, T. Edamura, and S. Maruyama, "Polarization dependent optical absorption properties of single-walled carbon nanotubes and methodology for the evaluation of their morphology," *Carbon*, vol. 43, no. 13, pp. 2664–2676, 2005.

[127] N. Nair, M. Usrey, W. Kim, R. Braatz, and M. Strano, "Estimation of the (n, m) concentration distribution of single-walled carbon nanotubes from photoabsorption spectra," *Analytical chemistry*, vol. 78, no. 22, pp. 7689–7696, 2006.

[128] R. Nair, P. Blake, A. Grigorenko, K. Novoselov, T. Booth, T. Stauber, N. Peres, and A. Geim, "Fine structure constant defines visual transparency of graphene," *Science*, vol. 320, no. 5881, p. 1308, 2008.

[129] A. Nasibulin and S. Shandakov, "Aerosol synthesis of single-walled carbon nanotubes," *Aerosols: Science and Technology*, vol. 3, p. 1, 2011.

[130] A. Naumov, S. Ghosh, D. Tsyboulski, S. Bachilo, and R. Weisman, "Analyzing absorption backgrounds in single-walled carbon nanotube spectra," *ACS Nano*, vol. 5, no. 3, pp. 1639–1648, 2011.

[131] A. Neto, F. Guinea, N. Peres, K. Novoselov, and A. Geim, "The electronic properties of graphene," *Reviews of Modern Physics*, vol. 81, no. 1, p. 109, 2009.

[132] Z. Ni, T. Yu, Y. Lu, Y. Wang, Y. Feng, and Z. Shen, "Uniaxial strain on graphene: Raman spectroscopy study and band-gap opening," *ACS Nano*, vol. 2, no. 11, pp. 2301–2305, 2008.

[133] A. Nojeh and A. Ivanov, "Wireless interconnect and the potential for carbon nanotubes," *IEEE Des. Test Comput.*, vol. 27, no. 4, pp. 44–53, 2010.

[134] A. Nojeh, P. Pande, A. Ganguly, S. Sheikhaei, B. Belzer, and A. Ivanov, "Reliability of wireless on-chip interconnects based on carbon nanotube antennas," in *Proc. IEEE 14th International Mixed-Signals, Sensors, and Systems Test Workshop*, Canada, June 2008, pp. 1–6.

[135] Y. Nosho, Y. Ohno, S. Kishimoto, and T. Mizutani, "n-type carbon nanotube field-effect transistors fabricated by using Ca contact electrodes," *Appl. Phys. Lett.*, vol. 86, no. 7, p. 073105, 2005.

[136] K. Novoselov, "Nobel lecture: Graphene: Materials in the flatland," *Bulletin of the American Physical Society*, vol. 56, 2011.

[137] K. Novoselov, A. Geim, S. Morozov, D. Jiang, M. Grigorieva, S. Dubonos, and A. Firsov, "Two-dimensional gas of massless dirac fermions in graphene," *Nature*, vol. 438, no. 7065, pp. 197–200, 2005.

[138] I. Nowak, "A new semidefinite programming bound for indefinite quadratic forms over a simplex," *J. Global Optim.*, vol. 14, no. 4, pp. 357–364, 1999.

[139] M. O'Connell, *Carbon Nanotubes: Properties and Applications*. FL, USA: CRC Pr., 2006.

[140] R. Olac-vaw, H. Kang, T. Komori, T. Watanabe, H. Karasawa, Y. Miyamoto, H. Handa, H. Fukidome, T. Suemitsu, M. Suemitsu, *et al.*, "Optoelectronic application of multi-layer epitaxial graphene on a Si substrate," in *Proc. IEEE 3rd Int. Nanoelectronics Conf. (INEC)*, Hong Kong, China, January 2010, pp. 224–225.

[141] J. Park, Y. Ahn, and C. Ruiz-Vargas, "Imaging of photocurrent generation and collection in single-layer graphene," *Nano Lett.*, vol. 9, no. 5, pp. 1742–1746, 2009.

[142] X. Peng and R. Ahuja, "Symmetry breaking induced bandgap in epitaxial graphene layers on sic," *Nano Lett.*, vol. 8, no. 12, pp. 4464–4468, 2008.

[143] V. Perebeinos and P. Avouris, "Inelastic scattering and current saturation in graphene," *Phys. Rev. B*, vol. 81, no. 19, p. 195442, 2010.

[144] D. Perello, S. ChuLim, S. Chae, I. Lee, M. Kim, Y. Lee, and M. Yun, "Anomalous Schottky barriers and contact band-to-band tunneling in carbon nanotube transistors," *ACS Nano*, vol. 4, no. 6, pp. 3103–3108, 2010.

[145] E. Peters, E. Lee, M. Burghard, and K. Kern, "Gate dependent photocurrents at a graphene p-n junction," *Appl. Phys. Lett.*, vol. 97, no. 19, pp. 193102–1–193102–3, 2010.

[146] V. Popov, L. Henrard, and P. Lambin, "Electron-phonon and electron-photon interactions and resonant Raman scattering from the radial-breathing mode of single-walled carbon nanotubes," *Phys. Rev. B*, vol. 72, no. 3, pp. 035436–1–035436–10, 2005.

[147] M. Pourfath, H. Kosina, and S. Selberherr, "Reduction of the dark-current in carbon nanotube photo-detectors," in *Proc. 38th European Solid-State Device Research Conf.*, Edinburgh, UK, September 2008, pp. 214–217.

[148] L. Prechtel, L. Song, S. Manus, D. Schuh, W. Wegscheider, and A. Holleitner, "Time-resolved picosecond photocurrents in contacted carbon nanotubes," *Nano Lett.*, vol. 11, no. 1, pp. 269–272, 2011.

[149] J. Proakis and M. Salehi, *Digital Communications*. Boston: McGraw-Hill, 1995.

[150] X. Qiu, M. Freitag, V. Perebeinos, and P. Avouris, "Photoconductivity spectra of single-carbon nanotubes: Implications on the nature of their excited states," *Nano Lett.*, vol. 5, no. 4, pp. 749–752, 2005.

[151] R. Ramesh, M. Madheswaran, and K. Kannan, "Physical noise model of a uniformly doped nanoscale FinFET photodetector," *Optik-International Journal for Light and Electron Optics*, 2011.

[152] R. Ramirez-Iniguez, S. Idrus, Z. Sun, and I. Books24x7, *Optical Wireless Communications: IR for Wireless Connectivity*. FL, USA: CRC Press, 2008.

[153] H. Raza, "Zigzag graphene nanoribbons: Bandgap and midgap state modulation," *Journal of Physics: Condensed Matter*, vol. 23, no. 38, p. 382203, 2011.

[154] D. Reddy, L. Register, G. Carpenter, and S. Banerjee, "Graphene field-effect transistors," *Journal of Physics D: Applied Physics*, vol. 44, no. 31, p. 313001, 2011.

[155] S. Reich, C. Thomsen, and J. Maultzsch, *Carbon Nanotubes: Basic Concepts and Physical Properties*. Germany: Wiley-Vch, 2004.

[156] S. Rice, "Mathematical analysis of random noise-conclusion," *Bell Systems Tech. J.*, vol. 24, pp. 46–156, 1945.

[157] J. Robinson, M. Hollander, M. LaBella, K. Trumbull, R. Cavalero, and D. Snyder, "Epitaxial graphene transistors: Enhancing performance via hydrogen intercalation," *Nano Lett.*, vol. 11, no. 9, pp. 3875–3880, 2011.

[158] P. Russer and N. Fichtner, "Nanoelectronics in radio-frequency technology," *IEEE Microwave Mag.*, vol. 11, no. 3, pp. 119 –135, 2010.

[159] V. Ryzhii, V. Mitin, M. Ryzhii, N. Ryabova, and T. Otsuji, "Device model for graphene nanoribbon phototransistor," *Appl. Phys. Expr.*, vol. 1, no. 6, p. 3002, 2008.

[160] V. Ryzhii and M. Ryzhii, "Graphene bilayer field-effect phototransistor for terahertz and infrared detection," *Phys. Rev. B*, vol. 79, no. 24, p. 245311, 2009.

[161] V. Ryzhii, M. Ryzhii, N. Ryabova, V. Mitin, and T. Otsuji, "Terahertz and infrared detectors based on graphene structures," *Infrared Phys. Technol.*, vol. 54, no. 3, pp. 302–305, 2011.

[162] K. Sattler, *Handbook of Nanophysics: Functional Nanomaterials*, vol. 5. FL, USA: CRC Pr., 2010.

[163] H. Schneider and H. Liu, *Quantum Well Infrared Photodetectors: Physics and Applications*. Berlin: Springer, 2007.

[164] F. Schwierz, "Graphene transistors," *Nat. Nanotechnol.*, vol. 5, no. 7, pp. 487–496, 2010.

[165] N. Sidiropoulos, T. Davidson, and Z. Luo, "Transmit beamforming for physical-layer multicasting," *IEEE Trans. Sig. Proc.*, vol. 54, no. 6, pp. 2239–2251, 2006.

[166] C. Soci, A. Zhang, X. Bao, H. Kim, Y. Lo, and D. Wang, "Nanowire photodetectors," *Journal of Nanoscience and Nanotechnology*, vol. 10, no. 3, pp. 1430–1449, 2010.

[167] D. Stewart and F. Léonard, "Photocurrents in nanotube junctions," *Phys. Rev. Lett.*, vol. 93, no. 10, p. 107401, 2004.

[168] D. Stewart and F. Leonard, "Energy conversion efficiency in nanotube optoelectronics," *Nano Lett.*, vol. 5, no. 2, pp. 219–222, 2005.

[169] J. Sturm, "Using sedumi 1.02, a matlab toolbox for optimization over symmetric cones," *Optim. Method Softw.*, vol. 11, no. 1, pp. 625–653, 1999.

[170] Z. Sun, T. Hasan, F. Torrisi, D. Popa, G. Privitera, F. Wang, F. Bonaccorso, D. Basko, and A. Ferrari, "Graphene mode-locked ultrafast laser," *ACS Nano*, vol. 4, no. 2, pp. 803–810, 2010.

[171] J. Svensson, A. Sourab, Y. Tarakanov, D. Lee, S. Park, S. Baek, Y. Park, and E. Campbell, "The dependence of the Schottky barrier height on carbon nanotube diameter for Pd-carbon nanotube contacts," *Nanotechnology*, vol. 20, no. 17, p. 175204, 2009.

[172] S. M. Sze and K. K. Ng., *Physics of Semiconductor Devices*. NJ, USA: Wiley, 2007.

[173] S. Sze, D. Coleman Jr, and A. Loya, "Current transport in metal-semiconductor-metal (MSM) structures," *Solid-State Electron.*, vol. 14, no. 12, pp. 1209–1218, 1971.

[174] C. Tao, L. Jiao, O. Yazyev, Y. Chen, J. Feng, X. Zhang, R. Capaz, J. Tour, A. Zettl, S. Louie, *et al.*, "Spatially resolving edge states of chiral graphene nanoribbons," *Nature Physics*, vol. 7, no. 8, pp. 616–620, 2011.

[175] S. Thornhill, N. Wu, Z. Wang, Q. Shi, and J. Chen, "Graphene nanoribbon field-effect transistors," in *Proc. IEEE Int. Symp. on Circuits and Systems (ISCAS)*, Washington, USA, May 2008, pp. 169–172.

[176] F. Tittel, D. Richter, A. Fried, *et al.*, "Mid-infrared laser applications in spectroscopy," *Quantum*, vol. 516, no. 7, pp. 445–516, 2003.

[177] F. Träger, *Springer handbook of lasers and optics*. New York, USA: Springer Verlag, 2007.

[178] J. Tworzydło, B. Trauzettel, M. Titov, A. Rycerz, and C. Beenakker, "Sub-poissonian shot noise in graphene," *Phys. Rev. Lett.*, vol. 96, no. 24, p. 246802, 2006.

[179] M. Ummy, N. Madamopoulos, A. Joyo, M. Kouar, and R. Dorsinville, "Tunable multi-wavelength SOA based linear cavity dual-output port fiber laser using Lyot-Sagnac loop mirror," *Optics Express*, vol. 19, no. 4, pp. 3202–3211, 2011.

[180] F. Vasko, "Saturation of interband absorption in graphene," *Phys. Rev. B*, vol. 82, no. 24, p. 245422, 2010.

[181] A. Venugopal, L. Colombo, and E. Vogel, "Contact resistance in few and multilayer graphene devices," *Appl. Phys. Lett.*, vol. 96, no. 1, pp. 013512–1–013512–3, 2010.

[182] S. Wang, L. Zhang, Z. Zhang, L. Ding, Q. Zeng, Z. Wang, X. Liang, M. Gao, J. Shen, H. Xu, *et al.*, "Photovoltaic effects in asymmetrically contacted CNT barrier-free bipolar diode," *J. Phys. Chem. C*, vol. 113, no. 17, pp. 6891–6893, 2009.

[183] J. Webster, *Wiley Encyclopedia of Electrical and Electronics Engineering*. New York, USA: Wiley, 1999.

[184] H. Wong and D. Akinwande, *Carbon Nanotube and Graphene Device Physics*. Cambridge, UK: Cambridge Univ. Pr., 2011.

[185] A. Wright, J. Cao, and C. Zhang, "Enhanced optical conductivity of bilayer graphene nanoribbons in the terahertz regime," *Phys. Rev. Lett.*, vol. 103, no. 20, p. 207401, 2009.

[186] F. Xia, T. Mueller, and P. Avouris, "Photocurrent imaging of the potential profiles in a graphene transistor," in *Proc. IEEE 21st Annu. Meeting of Lasers and Electro-Optic Society*, USA, November 2008, pp. 763–764.

[187] F. Xia, T. Mueller, R. Golizadeh-Mojarad, M. Freitag, Y. Lin, J. Tsang, V. Perebeinos, and P. Avouris, "Photocurrent imaging and efficient photon detection in a graphene transistor," *Nano Lett.*, vol. 9, no. 3, pp. 1039–1044, 2009.

[188] F. Xia, T. Mueller, Y. Lin, A. Valdes-Garcia, and P. Avouris, "Ultrafast graphene photodetector," *Nat. Nanotechnol.*, vol. 4, no. 12, pp. 839–843, 2009.

[189] F. Xia, V. Perebeinos, Y. Lin, Y. Wu, and P. Avouris, "The origins and limits of metal-graphene junction resistance," *Nat. Nanotechnol.*, vol. 6, no. 3, pp. 179–184, 2011.

[190] F. Xia, J. Thomson, M. Gokhale, P. Studenkov, J. Wei, W. Lin, and S. Forrest, "An asymmetric twin-waveguide high-bandwidth photodiode using a lateral taper coupler," *IEEE Photon. Technol. Lett.*, vol. 13, no. 8, pp. 845–847, 2001.

[191] J. Xia, F. Chen, J. Li, and N. Tao, "Measurement of the quantum capacitance of graphene," *Nat. Nanotechnol.*, vol. 4, no. 8, pp. 505–509, 2009.

[192] G. Xu, C. Torres Jr, J. Tang, J. Bai, E. Song, Y. Huang, X. Duan, Y. Zhang, and K. Wang, "Edge effect on resistance scaling rules in graphene nanostructures," *Nano Lett.*, vol. 11, no. 3, pp. 1082–1086, 2011.

[193] H. Xu, Z. Zhang, Z. Wang, S. Wang, X. Liang, and L. Peng, "Quantum capacitance limited vertical scaling of graphene field-effect transistor," *ACS Nano*, vol. 5, no. 3, pp. 2340–2347, 2011.

[194] X. Xu, N. Gabor, J. Alden, A. van der Zande, and P. McEuen, "Photo-thermoelectric effect at a graphene interface junction," *Nano Lett.*, vol. 10, no. 2, pp. 562–566, 2009.

[195] M. Yang, K. Teo, W. Milne, and D. Hasko, "Carbon nanotube Schottky diode and directionally dependent field-effect transistor using asymmetrical contacts," *Appl. Phys. Lett.*, vol. 87, no. 25, pp. 253116–1–253116–3, 2005.

[196] O. Yutaka, S. Kishimoto, and T. Mizutani, "Photoresponse of carbon nanotube field-effect transistors," *Jpn. J. Appl. Phys.*, vol. 44, no. 4A, pp. 1592–1595, 2005.

[197] H. Zhang, D. Tang, R. Knize, L. Zhao, Q. Bao, and K. Loh, "Graphene mode locked, wavelength-tunable, dissipative soliton fiber laser," *Appl. Phys. Lett.*, vol. 96, no. 11, pp. 111112–1–111112–3, 2010.

[198] J. Zhang, N. Xi, H. Chen, K. Lai, G. Li, and U. Wejinya, "Design, manufacturing, and testing of single-carbon-nanotube-based infrared sensors," *IEEE Trans. Nanotechnol.*, vol. 8, no. 2, pp. 245–251, 2009.

[199] J. Zhang, N. Xi, K. Lai, H. Chen, Y. Luo, and G. Li, "Single carbon nanotube based photodiodes for infrared detection," in *Proc. IEEE 7th Conf. on Nanotechnology (IEEE-NANO)*, Hong Kong, China, August 2007, pp. 1156–1160.

[200] Y. Zhang, "User's guide to LIPSOL: Linear programming interior point solver v0. 4," *Optim. Method Softw.*, vol. 11, no. 1/4, pp. 385–396, 1999.

[201] Y. Zhang, T. Tang, C. Girit, Z. Hao, M. Martin, A. Zettl, M. Crommie, Y. Shen, and F. Wang, "Direct observation of a widely tunable bandgap in bilayer graphene," *Nature*, vol. 459, no. 7248, pp. 820–823, 2009.